Oscillations in Stochastic Multi-species Interactions

Yang, Qian

Award date:
2018

Awarding institution:
University of Bath

Oscillations in Stochastic Multi-species Interactions

submitted by

Qian Yang

for the degree of Doctor of Philosophy

of the

University of Bath

Department of Mathematical Sciences

March 2018

致谢

原谅我先用中文写下这一章，毕竟这是整个毕业论文中最情绪化的一部分，也许母语更能表达我现在的心情。我保证，等我翻译把这一段翻译成英文时，尽量确保原汁原味。

我在巴斯度过了三年的博士生涯，这是我人生中第一次到这么遥远的地方长久地居住。得到许多师长友人的热情帮助，没有他们，我不可能完成这三年多的学业和生活。最最重要的最最要感谢的当然是我的导师们，乔纳森和蒂姆。我有两个非常有趣的导师，虽然性格脾性完全不同，但他们都带着英国人典型的幽默。何其有幸，得你们为导师，与君合作。感谢 CNCB 组，欢乐常在。

谢谢我的父母，从 18 岁以后我就很少陪伴他们。

感谢李建平教授，硕士期间对我的指导，博士期间对我的关怀；感谢白峰衫教授，使我有机会来到巴斯。

感谢我的爱人张港，我们一起遥望了 6 年，也会一起走过以后的 60 年。

感谢我的室友们，徐梦荣，刘子琛，童璐，刘阳，黄贺，一起做饭来避免英国的黑暗料理。

感谢师兄们，大师兄董恩铭在硕士期间给我巨大帮助，初到巴斯时一起当饭友；而后结识刘铱师兄，他们给了我对数学研究和巴斯的最初的印象。

感谢和女王同名的同事，每周帮我提升口语。

感谢插图彩色老虎和蜥蜴的两位作者，徐梦荣和米兰达。

感谢狼人杀，让我的生活里不仅仅有数学；感谢电影明星，李易峰和林更新，让我每天开开心心。

Acknowledgements

I wrote this part in Chinese at first because it is the most emotional part in the thesis. I guess that my mother language helps me express the feeling more precisely. I will try my best to offer an authentic translation as follows.

I spent more than three years living in Bath for my PhD studies. It's the first time I have lived in a place which is about 10,000 kilometers away from my hometown. I am deeply grateful to my supervisors, Jonathan Dawes and Tim Rogers, who encourage me to work hard, comfort me in culture differences, teach me mathematical knowledge and British jokes. They have different characters with the same typical British humor. It is my pleasure and my fortune to receive their supervision and collaborate with them. Thank CNCB group, fantastic academic atmosphere and good coffee and biscuits.

I also would like to thank my parents, I rarely accompany them after 18 years old; thank Prof. Jianping Li and Prof. Fengshan Bai, without them I can't obtain the chance of study in Bath; thank my husband, Gang Zhang, we have been together for 6 years and will be together more than 60 years in the future; thank my roommates, Mengrong Xu, Zichen Liu, Lu tong, Yang Liu and He Huang, and our cooking competitions; thank Elizabeth Arter, our weekly discussions help me practice my oral English; thank Enming Dong, Yi Liu, they give me much help in the first year of my PhD.

Many thanks to the two artists: Mengrong Xu and Miranda, they offered the colourful tiger and vivid lizard in Chapter 1.

Besides, I thank 'Werewolf Kill' and the board game weekly party; thank movie stars, Yifeng Li and Kenny Lin, make me happy every day.

List of publications 已发表工作

Demographic noise slows down cycles of dominance
Qian Yang, Tim Rogers, Jonathan H.P.Dawes,
Journal of Theoretical Biology, 432, pp. 157-168. (2017)

Faster and stronger stochastic oscillations induced by interference in autocatalytic networks
Qian Yang, Tim Rogers,
In preparation.

Summary 摘要

This thesis mainly presents new research on mathematical descriptions for stochastic interactions in multi-species systems. Oscillations have been observed in many biological competition models, e.g. the Lotka-Volterra model and the Rock-Paper-Scissors (RPS) model. In this thesis, by analysing properties of these oscillations, the effects of demographic noise are demonstrated and comprehensively explained in some specific stochastic multi-species competition models. Three paradigmatic models are introduced and analysed using novel, and, generally applicable techniques.

Chapter 2 considers the well-known cyclic dominance dynamics of three mutually-competing populations, as in the toy model for the RPS game. In this chapter, the non-zero-sum RPS model is studied in detail, especially for the case with small mutation rate. The mean period of oscillations is computed in detail for stochastic competition models. Phenomena that are observed numerically are explained theoretically in details using techniques from Markov Processes, asymptotics, local-global maps and stochastic differential equations.

In chapter 3 the focus is on the extension to models of four species interacting. Even in the simplest case of symmetric interactions there are new possibilities for the deterministic (and stochastic) dynamics.

Chapter 4 considers the effect of a random environment of competitive interactions on the dynamics of the simplest RPS model. By coupling the zero-sum RPS model to a larger well-mixed random system, the RPS subsystem still has a sustained oscillation, but the oscillation has larger amplitude and higher frequency which is induced by the random interaction network. Via the cavity method, the changes in amplitude and frequency can be estimated quantitatively.

Contents 目录

致谢 **1**

Acknowledgements **1**

List of Publications 已发表工作 **2**

1 Introduction 概述 **7**

1.1 Research Context 7

1.1.1 Competition Between Species and Cyclic Phenomena 9

1.1.2 Research Objectives 11

1.2 Thesis Layout 12

1.3 Methodology 13

1.3.1 Replicator Equation, Chemical Reactions, and the Gillespie Algorithm 13

1.3.2 Fokker-Planck Equation and Stochastic Differential Equation . . 17

1.3.3 Jump Matrix following Kurtz's theorem 22

1.3.4 Power Spectral Density 24

1.3.5 Random Matrix and Cavity method 25

1.3.6 Method Summary 31

2 Three Species Competition 三种群竞争 **32**

2.1 Two Updated Models based on the RPS Model 32

2.1.1 Symmetric RPS Model with Mutation 33

2.1.2 Asymmetric RPS Model with Mutation 39

2.2 Behaviour of the Limit Cycle in Regions I–III 46

2.2.1 Analysis of the Periodic Orbit in Region I 47

2.2.2 Analysis of the Periodic Orbit in Region III 51

2.2.3 Analysis of the Periodic Orbit in Region II 60

2.2.4 Short Summary 69

3 Four Species Competition 四种群竞争 **70**
3.1 Model 71
3.1.1 Replicator Equations 71
3.1.2 Technique of Finding Reactions 72
3.1.3 Existence and Stability of Equilibria 74
3.2 Heteroclinic Cycles 78
3.2.1 Stability of Cycles 78
3.2.2 Maps of Cycles 81

4 Interactions between Species and Complex Environment 种群竞争与环境互动 **86**
4.1 An Isolated 'Island' 86
4.1.1 Model 87
4.1.2 Analysis of Oscillations 89
4.2 Adding Specific Species to the 'Island' 95
4.2.1 Coupling Model – Overlap of Two Evolving Systems 95
4.2.2 Spectrum Calculation 98
4.2.3 Effects from the Complicated Environment 101

5 Discussion and Conclusion 总结与探讨 **104**
5.1 3-species Competition 104
5.2 Four-species Competition 106
5.3 Many species Competition 106

Appendices **108**

A Itô's formula **109**

B Power Spectral Density **113**

Bibliography 参考文献 **119**

Chapter 1

Introduction 概述

1.1 Research Context

I have two stories to start my thesis. First is a piece of news from China [1]: during the Spring Festival of 2017 (which is the biggest holiday in China), a visitor had been mauled to death by a tiger in Ningbo Zoo, after he climbed over the zoo's wall to avoid paying for a ticket and landed in the tiger enclosure. The tiger was then shot dead by a policeman. This news is very unfortunate, however, it raises a question: which species is stronger? Human beings or tigers? The death of the visitor and the tiger shows the struggle between the two populations, filled with contingency and inevitability.

The other story is also about a human and a tiger but it is a fictional story with the title 'Life of Pi' [44]. The protagonist is a boy called 'Pi', who lives with a tiger 'Richard Parker' on a life boat in the Pacific Ocean for 227 days. In this extreme environment, they learn to coexist harmoniously and finally survive. Their survival is a miracle and against the reader's expectations.

Interactions between species including competition and cooperation determine structures of biological system. Each interaction is not only the individuals' behaviour, but also, in a sense, a game played between them. Nowak and Sigmund's article [63] in 2004 has reviewed many biological game models to show the historical developments of Evolutionary Game Theory (EGT). Following Nowak's terminology, we also use a 'game' to show an interaction between a set of individuals, and these 'players' are 'types' of interest (be they species, chemicals, bacterial disease strains). They act according to their behaviour phenotypes, which are called 'strategies' in Game Theory.

The players' payoffs are translated into 'fitness' which depends on their own strategies and on that of their co-players. For more detailed notions please refer to section 1.3.

Nash equilibrium is an important definition in classic Game Theory. In a non-cooperation game, a Nash equilibrium is a combination of strategies such that no player has anything to gain by changing only their own strategy [57]. John Maynard Smith in 1973 introduced a concept of Evolutionarily Stable Strategies (ESS) by refining the form of a Nash equilibrium [76]. An ESS is a Nash equilibrium that is "evolutionarily" stable: once most of the members of a population adopt it, there is no alternative strategy that would give higher fitness (payoff). Here, the idea is that most of the members adopt it because of 'Darwinian selection': individuals best adapted to their environments are more likely to survive and reproduce. Roughly speaking, ESS is an application of Nash equilibrium in biology, like Evolutionary game theory (EGT) is the application of game theory to evolving populations in biology.

The first use of game-theoretic arguments can be found in the field of sex-ratio theory [15, 81]. ESS were introduced to discuss the prevalence of ritual fighting in interspecific animal conflicts. Examples include mate choice [29], siblings rivalry [52] and the arms races between predators and prey [2]. Increasingly, EGT is also used in economic and social sciences and applied to experimental games with human subjects [62, 85, 25, 18]. Even genes, bacteria, organelles, and viruses can be engaged in games of cooperation and conflict [83, 67, 34].

Darwinian selection is a plain but very general concept in Biological Evolution Theory (BET). In EGT, the 'old-fashioned' concept is borrowed and developed. The classical understanding of 'selection' was based on the assumption that the fitness of a phenotype is independent of the abundance of that phenotype in the population. However, frequency-dependent selection arises and appears to play an important role in many applications. Frequency-dependent selection is an evolutionary process by which the fitness of a phenotype depends on its frequency relative to other phenotypes in a given population. For example, in the evolution of the virulence of infectious agents, parasites evolve to maximize their basic reproductive ratio [4]. This is based on a hypothesis of constant selection. At the same time, if several parasite strains super-infect the same host or rapid evolution generates many different parasite mutants in any one infected individual, then frequency-dependent selection is probably important [61].

Not only from BET, but also from Game Theory (GT), EGT inherits many basic concepts and opinions and develops them in its own applications. Many phenomena are difficult to explain just through the static classical GT because the equilibrium notion of Nash and the quest for a unique solution to rational play does not exist in many

biological systems. For example, a simple toy game, named 'rock-paper-scissors', has a long-term outcome which is not a Nash equilibrium but endless regular or irregular oscillations. This model will be introduced in detail in section 1.3. The above discussion shows that the static GT approach (e.g. Nash rational play and Nash equilibrium) is unable to provide a full analysis and explanations for the biological/ecological interaction models. Hence, we are led to consider the development of a dynamical theory, EGT. In contrast with GT, EGT considers the population dynamics of a biological system by extending the concepts 'unbeatable strategy' and 'evolutionary stability'. Then the potential success of invading mutants and the interplay between mutation in frequency-dependent selection (as remarked in the Darwinian selection paragraph above) is described well by EGT [61]. Generally speaking, the population dynamics depends on the structure of the population (in this thesis we will assume the population is well-mixed), on the mechanisms for the transmission of the relevant traits (by competing or genetic inheritance), and on the time scales underlying the evolutionary and ecological processes [63].

1.1.1 Competition Between Species and Cyclic Phenomena

Competition between species is a key driver of complex dynamics in ecology. It is also an important research project in theoretical EGT. Even very simple competitive interactions can yield complex dynamical behaviour, for example the well-known Lotka-Volterra model for predator-prey interactions [42, 43, 84, 45]. The Lotka-Volterra model for the evolutionary dynamics of two species – A (predator) and B (prey), has four distinct outcomes(Figure 1-1(a)) [63]. (i) Dominance: A vanishes (or, equivalently B). (ii) Bi-stability: Either A or B vanishes, depending on the initial condition. (iii) Coexistence: A and B coexist in a stable proportions. (iv) Neutrality: Any proportions of A and B are in equilibrium. Here the cases (i), (ii), (iii) all correspond to the ecological examples of two-species competition [63, 47].

With three species, the outcome of competitions looks considerably more complicated. The most obvious difference is the existence of 'Rock-Paper-Scissors' cycle in a 3-species model(Fig 1-1(c)). Depending on the parameters of the game, the evolutionary trajectories can spiral inwards, leading to a stable coexistence state of all three species, or spiral outwards, leading to (in the most obvious stochastic dynamical case) a random extinction of two species. These cyclic phenomena have been observed in different ecological systems. For example, in the mating strategy of some species lizards [75], there exist three morphs of male lizards who differ in their throat colour (Fig 1-1(b)). The strongest type A always succeeds in preventing other males from approaching their mate. Type C is less efficient but still can beat type B and obtain the mating right.

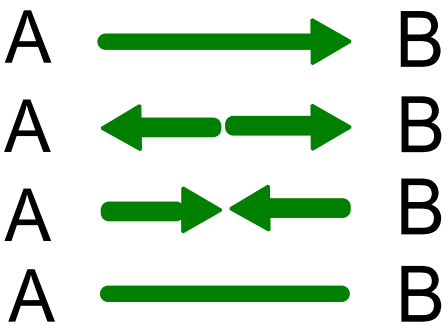

(a) L–V model

(b) Side-blotched lizard

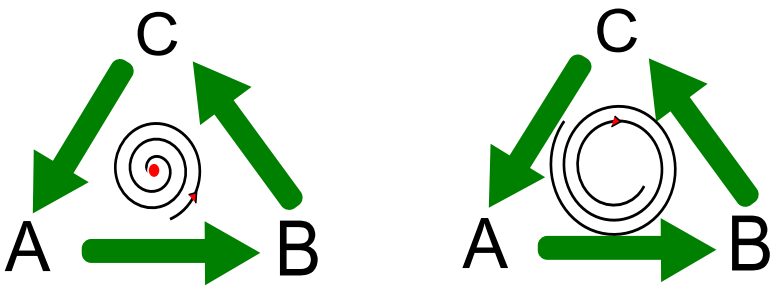

(c) Three species

Figure(图) 1-1: Different possibilities for population interactions. (a) Four outcomes of Lotka-Volterra Model: B always wins; A or B wins depending on the initial status; stable coexistence, or neutral interactions and coexistence with different proportions is possible; (b) Different species of side-blotched lizards are distinguished by different throat colours; (c) Two outcomes of dynamical three-species competitions: trajectories spiral inwards to an equilibrium or spiral outwards towards the single-species equilibria.

Only type B who is the weakest and does not engage in female-guarding behaviour at all, roams around in search of sneaky matings. The other example is *Escherichia coli* bacteria. There exist three strains who exhibit a similar RPS competitive relationship [31]. For a more detailed model description and methods, please refer to section 1.3.1.

In the case of four or more species, cyclical interactions have much more complicated evolutionary behaviours [78]. For example, the emergence of defensive alliances [77] is stimulated by four-strategy food web with different invasion rates between predator-prey pairs. Similar defensive alliances, as well as noise-guided evolution, have been found in a six-species food web with heterogeneous invasion rates [66]. As paper [78] M. Mobilia remarks, although the outcome of evolutionary game with cyclic dominance may depend on the properties of the interaction networks, on the topology of the network structure, and on the number of species (or strategy) engaged in competitions, there exists fascinatingly robust universal behaviour that is independent of model particularities. In four words, we are interested in such 'kinds of robust cycles'.

1.1.2 Research Objectives

Cyclic competitions play a prominent role in explaining biodiversity in nature [9, 31, 70, 78]. The RPS model mentioned in last section is a good example for explaining the coexistence of three species. Although at infinite population, the RPS model shows cyclic coexistence of 3-species, at finite population size with noise, this model cannot sustain this biodiversity indefinitely. In the latter case, only one species survives finally. If each species has same reproduction-predation rate, we can not predict which one wins. Otherwise, the most likely species to win is the one with the lowest reproduction-predation rate [69, 6]. This reminds us that differences that result from by randomness may arise between the observation in nature and the theoretical prediction in the lab, because the real world is discrete and limited while the analytical researchers prefer assuming a continuous and infinite population model. All discussion above shows that only studying the population dynamics in a deterministic setting is not enough.

Recently research has focussed on building bridges between deterministic models for the case of an infinite population and stochastic models for a finite population. Normally, the deterministic model would provide us with the first impression of the evolution in a system. In many instances of ecological/chemical systems, macro-behaviour could be explained well by a deterministic model. After that, considering the same system without the large population limit assumption, researchers build relevant mathematical models, often based on stochastic processes and other probabilistic tools. For example, they establish differential equations with a stochastic diffusion according interactions at individual level [5, 37], and analyse them using the theory of Stochastic

Differential Equations (SDEs). In this thesis we follow this study pattern, combining deterministic and stochastic approaches in order to present a comprehensive description of demographic fluctuations (which means the noise comes from the discrete and finite population) in the evolution of 'biological species'(or other 'types').

We are also interested in the periodicity and amplitude of different oscillations which often emerge in the species competitions, e.g the regular dominance in RPS model. These oscillations may be broken up, damped, or enhanced in different cases. For example, demographic noise often change these properties (slowing down or speeding up the period) of the oscillations [87]. Specifically, in this thesis we combine a set of methods to determine the existence of periodic or quasi-periodic cycles as well as to predict the period according to intrinsic parameters given in different models.

In summary, the motivations of this thesis could be summarised as following: (1) keeping the biodiversity; (2) bridging deterministic models and stochastic models; (3) finding the oscillations in the competitions between species; (4) predicting the period and amplitude (analytically or numerically) of the oscillations.

1.2 Thesis Layout

The thesis consists of five chapters. **Chapter 1** is the introduction, divided into two parts. The first part has stated the general biological background to the project and my specific research objectives. The second part summarises the mathematical methodology that I used in the research. **Chapter 2** concerns 3-species competition. A classic 3-species model, Rock-Paper-Scissors(RPS) model is reviewed here, with the inclusion of mutation effects. We find a sustained oscillation around the inner equilibrium in the stochastic model, while in the infinite and continuous model the oscillation is damped. An extended model with an asymmetric payoff matrix is also discussed. It is different from symmetric model, having a limit cycle when mutation rate is smaller than a critical value. **Chapter 3** concerns 4-species interactions, in the permutational symmetrical case. **Chapter 4** discusses the coupling a subsystem (i.e. the RPS model) to a complicated, bulk environment. Mainly we study the effects of the environment on the stochastic oscillation of the subsystem (which is also discussed in chapter 2). **Chapter 5** discusses possible future work and summarises the results of the thesis.

The main results in Chapter 2 have been published in paper [87]. Further papers based on the results in Chapter 3 and 4 are currently in preparation.

1.3 Methodology

The existence of 'autocatalytic networks' is a very useful hypothesis that helps scientists to understand the origin and the organization of life [27]. By definition, this network is a collection of species, each of which can be reproduced catalytically by other species within the set (e.g. RPS model [51], RNA world [39, 27], and some biochemical networks [10]). In this thesis, we study the research objectives in the paradigmatic case of an autocatalytic network.

Mathematically, there are two kinds of autocatalytic network being discussed later. The first type is the deterministic toy model – RPS [51]. It is a small autocatalytic reaction network. We will explain it mainly in section 1.3.1. In 1.3.2 and 1.3.3 we will discuss some mathematical tools based on the network. The second type discussed in the thesis is a kind of random graph. It is equivalent to a random matrix in principle since the random graph can be expressed by the adjacency matrix. In section 1.3.5, we define such random autocatalytic reaction networks and we present an algorithm for generating them.

1.3.1 Replicator Equation, Chemical Reactions, and the Gillespie Algorithm

A classical formalism for studying biological competitions is that of **Replicator Equations** (REs). The core idea of REs is to introduce Game Theory to Evolutionary Dynamics, and to use a Payoff Matrix (which is often used to present relations between strategies) to show interactions between species [26]. The gain or loss of Species i when it fights against Species j is notated by p_{ij}, forming a 'payoff matrix' $P := (p_{ij})_{n\times n}$. The relative abundance (or frequency) of species i is denoted by x_i; its expected overall gain in the system is $f_i := \sum_{j=1}^{n} p_{ij}x_j$, where the number n is total of species. The average gain of the whole system is defined as $\phi := \sum_{i=1}^{n} x_i f_i$. Briefly, if single species' gain is greater than the average, then the relative abundance (or frequency) will increase. This mechanism is captured by replicator equations as follows:

$$\dot{x}_i = x_i \left(f_i - \phi\right), \quad i = 1, ..., n. \tag{1.1}$$

Rock-Paper-Scissors model is a good toy example to present the technique. RPS game is a simple two-player, three-state game which illustrates the idea of cyclic dominance: a collection of strategies, or unchanging system states, in which each state in turn is unstable to the next in the cycle. In mathematical neuroscience dynamical switches between such a collection of system states has been referred to as 'winnerless competition' since there is no best-performing state overall [68, 82]. In detail: playing

the strategy 'rock' beats the strategy 'scissors' but loses to the strategy 'paper'; similarly, 'scissors' beats 'paper' but loses to 'rock'. When the two players play the same strategy the contest is a draw.

In game theory, the usual way to summarise this information is via a payoff matrix that specifies the payoff to one player from all possible combinations of actions by both players. It is a mean-field presentation for the competition. In the two-player RPS game, we define the payoff matrix P by setting the entry (p_{ij}) to be the payoff to player 1 when player 1 plays strategy i and player 2 plays strategy j. For the RPS game we summarise the payoffs in the following table and payoff matrix P:

	A	B	C
A	0	1	−1
B	−1	0	1
C	1	−1	0

$$P = \begin{pmatrix} 0 & -1 & 1 \\ 1 & 0 & -1 \\ -1 & 1 & 0 \end{pmatrix} \tag{1.2}$$

Its corresponding REs are:

$$\begin{aligned} \dot{x}_1 &= x_1(x_3 - x_2), \\ \dot{x}_2 &= x_2(x_1 - x_3), \\ \dot{x}_3 &= x_3(x_2 - x_1). \end{aligned} \tag{1.3}$$

Note that $\phi = 0$ (since P is anti-symmetric). This is a deterministic and mean-field model. In the figure 1-3(b), a closed orbit can be clearly observed. This phenomenon can be explained by considering the function $V(t) = x_1(t)x_2(t)x_3(t)$ in the toy RPS model; for which

$$\begin{aligned} \dot{V} =& \dot{x}_1 x_2 x_3 + x_1 \dot{x}_2 x_3 + x_1 x_2 \dot{x}_3 \\ =& x_2 x_3 (x_3 x_1 - x_1 x_2) + x_1 x_3 (x_1 x_2 - x_2 x_3) + x_1 x_2 (x_2 x_3 - x_3 x_1) \\ =& 0\,, \end{aligned} \tag{1.4}$$

and hence trajectories for the ODEs lie in level sets $V = constant$.

Chemical reaction schemes are a visual and stochastic version of interactions between species. For example, the reactions below have the same mean-field ODEs as (1.3) [69].

$$\begin{aligned} A + B &\xrightarrow{1} B + B, \\ B + C &\xrightarrow{1} C + C, \\ C + A &\xrightarrow{1} A + A. \end{aligned} \tag{1.5}$$

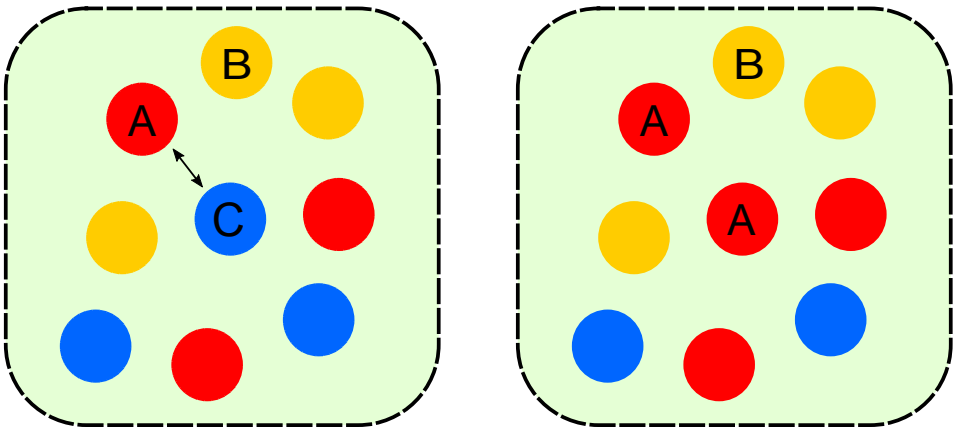

(a) Before a reaction (b) After the reaction

Figure(图) 1-2: This figure describes stochastic evolution of a well-mixed finite biological system, in which there are three species A, B and C. At each time step, two random individuals are chosen to react, and the weaker one will be replaced by its opponent. It is an example of Moran process: in each time step a random individual (which is of either type A or C) is chosen for reproduction and a random individual is chosen for death; thus ensuring that the population size remains constant.

These reactions imply that when an individual from species A meets an individual from species B, the result is to form two individuals from species B; and similarly for the second and third chemical reaction.

These reactions form an autocatalytic network, represented by the reaction matrix:

$$\boldsymbol{R} = \begin{pmatrix} 0 & 1 & 0 \\ 0 & 0 & 1 \\ 1 & 0 & 0 \end{pmatrix} . \tag{1.6}$$

Here each component R_{ij} is the rate of a reaction $X_i + X_j \xrightarrow{R_{ij}} 2X_j$, specifically in RPS model $(X_1, X_2, X_3) = (A, B, C)$.

Consider a population of size N which is well-mixed, with its stochastic dynamics described by the chemical reactions (1.5). This is closely related to the Moran process [69, 53, 40], which has been illustrated in figure 1-2. The **Gillespie Algorithm** [21] is the classical stochastic simulation algorithm (SSA) for the stochastic modelling of chemical reactions. In contrast to ODEs, the Gillespie algorithm allows a discrete and stochastic simulation of a system with few reactants because every reaction is explicitly simulated.

To simulate the system of chemical reactions (1.5), we perform the following steps at time t, which starts with $A(0) = A_0, B(0) = B_0, C(0) = C_0$, and $A_0 + B_0 + C_0 = N$.

Algorithm 1.1 (Gillespie Reaction Simulation for RPS)**.**

1. *Generate two random numbers r_1 and r_2 uniformly distributed in $(0,1)$.*

2. *Compute the propensity functions of each reaction $\alpha_1 := A(t)B(t)/N$, $\alpha_2 := B(t)C(t)/N$, $\alpha_3 := C(t)A(t)/N$. Compute the total propensity $\alpha_0 = \alpha_1+\alpha_2+\alpha_3$.*

3. *Compute the time when the next chemical reaction takes place as $t+\tau$ where*

$$\tau = \frac{1}{\alpha_0}\log\left[\frac{1}{r_1}\right]. \tag{1.7}$$

4. *Compute the number of individuals at time $t+\tau$ by*

$$A(t+\tau) = \begin{cases} A(t)-1 & \text{if} \quad 0 \le r_2 < \alpha_1/\alpha_0; \\ A(t) & \text{if} \quad \alpha_1/\alpha_0 \le r_2 < (\alpha_1+\alpha_2)/\alpha_0; \\ A(t)+1 & \text{if} \quad (\alpha_1+\alpha_2)/\alpha_0 \le r_2 < 1; \end{cases} \tag{1.8}$$

$$B(t+\tau) = \begin{cases} B(t)+1 & \text{if} \quad 0 \le r_2 < \alpha_1/\alpha_0; \\ B(t)-1 & \text{if} \quad \alpha_1/\alpha_0 \le r_2 < (\alpha_1+\alpha_2)/\alpha_0; \\ B(t) & \text{if} \quad (\alpha_1+\alpha_2)/\alpha_0 \le r_2 < 1; \end{cases} \tag{1.9}$$

$$C(t+\tau) = \begin{cases} C(t) & \text{if} \quad 0 \le r_2 < \alpha_1/\alpha_0; \\ C(t)+1 & \text{if} \quad \alpha_1/\alpha_0 \le r_2 < (\alpha_1+\alpha_2)/\alpha_0; \\ C(t)-1 & \text{if} \quad (\alpha_1+\alpha_2)/\alpha_0 \le r_2 < 1; \end{cases} \tag{1.10}$$

5. *Return to step 1.*

The Gillespie simulation algorithm is shown in algorithm 1.1 in the paradigmatic case. In fact, it could be applied to any reaction scheme.

Fig 1-3(a) shows the cyclic dominance of the three species for the replicator equations (1.3). We find that although the $x_i(t)$ fluctuate up and down, they never die out completely. The periodic evolution of $x_i(t)$ corresponds to the numerical results of ODEs (1.3) and to the blue solid line in the right subfigure 1-3(b). Plotting in barycentric coordinates (because $x_1+x_2+x_3=1$), which is shown in 1-3(b), it is clear to observe that the periodic evolution of $x_i(t)$ forms approximately closed orbits, and the radius and the location of these orbits only depends on the initial value of ODEs [51]. In this and subsequent figures we represent the 2-dimensional phase space using the coordinates (y_1, y_2) defined to be $y_1 := x_1 + \frac{1}{2}x_2$, $y_2 := \frac{\sqrt{3}}{2}x_2$.

However, changes happen when we introduce some demographic noise. The red line in figure 1-3(b) is produced by the stochastic simulation (Gillespie Algorithm 1.1)

with $N = 256$ individuals. It clearly looks to be randomly evolving in time. And there are also qualitative differences, for example the way in which the stochastic evolution hits the boundary (an absorbing set for the dynamics) and then the corner of the simplex (also absorbing) as the species go extinct one by one, until only one survives. The disagreement between the result of the ODEs and the result of the simulations in the toy model illustrates the gap between the deterministic and the stochastic modelling approaches to the same problem.

In summary, the three methods introduced here often give us useful initial information for many models. They will make useful contributions and form the basis for the whole thesis.

1.3.2 Fokker-Planck Equation and Stochastic Differential Equation

In order to reveal the effects of demographic noise, we return to the toy model and chemical reactions (1.5), and consider in detail the derivation of the differential equations from the individual–level stochastic processes.

At the individual level, each step of evolution is randomly chosen following the reaction rules and rates. The state of the system is represented by a vector $\boldsymbol{n} = (n_1, n_2, n_3)^T$ where $n_1 + n_2 + n_3 = N$. The probability of the system being in state $\boldsymbol{n}$ at time t is defined as $\mathbb{P}(\boldsymbol{n}, t)$. The transition rates $T(\boldsymbol{n}'|\boldsymbol{n})$ from state $\boldsymbol{n}$ to the state $\boldsymbol{n}'$ are given by expressions similar to equation (1) of [48] extended because we have three reactions (1.5):

$$T(n_1 - 1, n_2 + 1, n_3) = \frac{n_1 n_2}{N}\,, \tag{1.11}$$

$$T(n_1, n_2 - 1, n_3 + 1) = \frac{n_2 n_3}{N}\,, \tag{1.12}$$

$$T(n_1 + 1, n_2, n_3 - 1) = \frac{n_3 n_1}{N}\,. \tag{1.13}$$

These transition rates are proportional to the product of the number of individuals in the reaction species on the left-hand-sides of the chemical reactions (1.5). The term '$|\boldsymbol{n}$' can be omitted because the information is contained in the arguments n_1, n_2, n_3.

Let $\mathbb{P}(\boldsymbol{n}, t|\boldsymbol{n}_0, t_0)$ denote the probability that the system is in state $\boldsymbol{n}$ at time t given that it was in state $\boldsymbol{n}_0$ at time t_0, where $t_0 < t$. As discussed in section 3 of [11], we have

$$\mathbb{P}(\boldsymbol{n}, t + \Delta t) = \sum_{\boldsymbol{n}'} \mathbb{P}(\boldsymbol{n}, \Delta t|\boldsymbol{n}', 0)\mathbb{P}(\boldsymbol{n}', t), \tag{1.14}$$

with

$$\mathbb{P}(\boldsymbol{n}, \Delta t|\boldsymbol{n}', 0) = T(\boldsymbol{n}'|\boldsymbol{n})\Delta t + O(\Delta t^2), \tag{1.15}$$

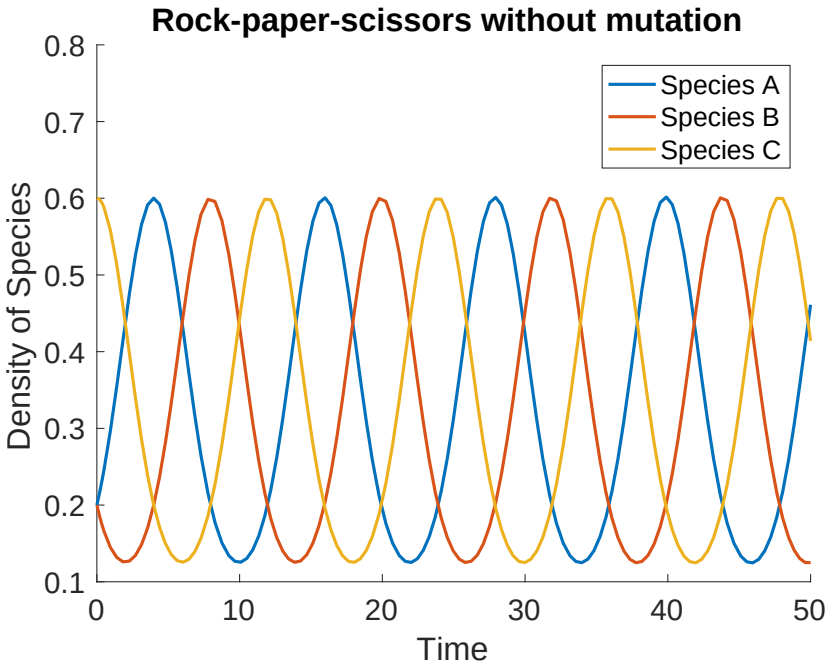

(a) Result of ODE (1.3) in coordinates: time vs $x_i(t)$.

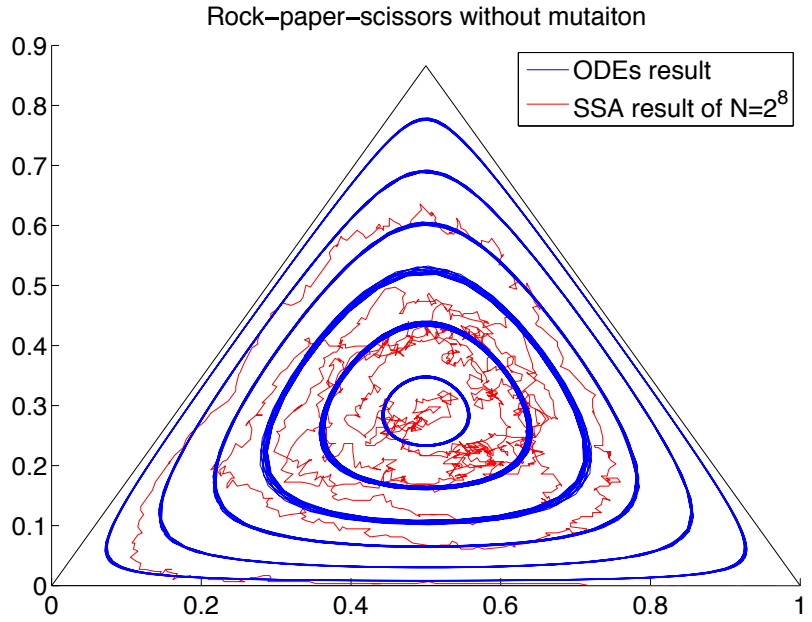

(b) $x_i(t)$ in barycentric coordinates.

Figure(图) 1-3: The figure shows comparison between the solution to REs and the stochastic simulation (algorithm 1.1) result with population size $N = 256$. (a) The solution to ODEs; (b) The solution to ODEs and the simulation of stochastic simulation algorithm (SSA): in a three-species simplex. Horizontal direction $y_1 = x_1 + x_2/2$ and vertical direction $y_2 = \sqrt{3}x_2/2$.

which is the evolution operator generating $\mathbb{P}(\boldsymbol{n}, t+\Delta t)$ from $\mathbb{P}(\boldsymbol{n}, t)$ where Δt is a very small time interval (small enough that with high probability at most one reaction can occur). Here, equation (1.15) is the conditional probability of being in state $\boldsymbol{n}$ at time Δt, given that the system is in state $\boldsymbol{n}'$ at time 0, expressed to leading order in Δt, in terms of transition rate. In order to write these transitions in a more compact notation, we follow [11] and introduce three step operators $\mathbb{E}_1$, $\mathbb{E}_2$, $\mathbb{E}_3$ that act to increment the variables indicated by the respective subscripts:

$$\mathbb{E}_1[f(\boldsymbol{n})] := f(n_1+1, n_2, n_3)\,, \tag{1.16}$$

$$\mathbb{E}_2[f(\boldsymbol{n})] := f(n_1, n_2+1, n_3)\,, \tag{1.17}$$

$$\mathbb{E}_3[f(\boldsymbol{n})] := f(n_1, n_2, n_3+1)\,. \tag{1.18}$$

Naturally these step operators have inverses which represent decrements by 1 in each case. Using these operators it is straightforward to compute $\mathbb{P}(\boldsymbol{n}, t+\Delta t)$ in terms of $\mathbb{P}(\boldsymbol{n}, t)$:

$$\begin{aligned}\mathbb{P}(\mathbf{n}, t+\Delta t) = \mathbb{P}(\mathbf{n}, t) &+ (\mathbb{E}_A\mathbb{E}_B^{-1} - 1)[T(n_1-1, n_2+1, n_3)\Delta t\mathbb{P}(\mathbf{n}, t)] \\ &+ (\mathbb{E}_B\mathbb{E}_C^{-1} - 1)[T(n_1, n_2-1, n_3+1)\Delta t\mathbb{P}(\mathbf{n}, t)] \\ &+ (\mathbb{E}_C\mathbb{E}_A^{-1} - 1)[T(n_1+1, n_2, n_3-1)\Delta t\mathbb{P}(\mathbf{n}, t)] \\ &+ O(\Delta t^2).\end{aligned} \tag{1.19}$$

We use the scaled variables $\boldsymbol{x} = \boldsymbol{n}/N$, which is exactly the species frequencies x_i from the last section, to define a probability density in terms of these variables:

$$P(\boldsymbol{x}, t, N) := \frac{\mathbb{P}(\boldsymbol{n}, t)}{1/N}, \tag{1.20}$$

then the step operators (1.16)-(1.18) similarly can be redefined as

$$\mathbb{E}_1[g(\boldsymbol{x})] := g\left(x_1 + 1/N, x_2, x_3\right), \tag{1.21}$$

$$\mathbb{E}_2[g(\boldsymbol{x})] := g\left(x_1, x_2 + 1/N, x_3\right), \tag{1.22}$$

$$\mathbb{E}_3[g(\boldsymbol{x})] := g\left(x_1, x_2, x_3 + 1/N\right), \tag{1.23}$$

By introducing (1.20) and (1.11)-(1.13) into (1.19) and tidying it up, we now can write

the evolution of the discrete probability density (1.19) in the form:

$$\begin{aligned}\frac{1}{N\Delta t}(P(\mathbf{x},t+\Delta t,N)-P(\mathbf{x},t,N)) =&(\mathbb{E}_1\mathbb{E}_2^{-1}-1)\big[x_1x_2P(\mathbf{x},t,N)\big]\\ &+(\mathbb{E}_2\mathbb{E}_3^{-1}-1)\big[x_2x_3P(\mathbf{x},t,N)\big]\\ &+(\mathbb{E}_3\mathbb{E}_1^{-1}-1)\big[x_3x_1P(\mathbf{x},t,N)\big]\\ &+O(\Delta t).\end{aligned} \tag{1.24}$$

Expanding the terms with step operators for a Taylor series up to a sufficient by high order ($O(1/N^2)$), for example

$$\begin{aligned}(\mathbb{E}_1\mathbb{E}_2^{-1}-1)\big[x_1x_2P\big] =& \frac{1}{N}\left(\frac{\partial}{\partial x_1}-\frac{\partial}{\partial x_2}\right)[x_1x_2P]\\ &+\frac{1}{2N^2}\left(\frac{\partial}{\partial x_1}-\frac{\partial}{\partial x_2}\right)^2[x_1x_2P]+O\left(\Delta t,\frac{1}{N^3}\right).\end{aligned} \tag{1.25}$$

In the limit $\Delta t\to 0$ and at leading order in $1/N$, (1.24) can be simplified into the form of:

$$\frac{\partial P}{\partial t}+\nabla\cdot(\boldsymbol{u}P)=\frac{1}{2}\frac{\partial}{\partial \boldsymbol{x}}\left(\frac{\partial}{\partial \boldsymbol{x}}\right)^T(\boldsymbol{B}P) \tag{1.26}$$

where $\boldsymbol{u}(\boldsymbol{x})$ is the vector field $\begin{pmatrix}x_1x_3-x_1x_2\\ x_2x_1-x_2x_3\\ x_3x_2-x_3x_1\end{pmatrix}$ corresponding to the nonlinear ODEs (1.3), and the matrix $\boldsymbol{B}$ is:

$$\boldsymbol{B}(\boldsymbol{x}):=\frac{1}{N}\begin{pmatrix}x_1(x_2+x_3) & -x_1x_2 & -x_1x_3\\ -x_1x_2 & x_2(x_1+x_3) & -x_2x_3\\ -x_1x_3 & -x_2x_3 & x_3(x_1+x_2)\end{pmatrix}. \tag{1.27}$$

Passing to the limit $N\to\infty$, we obtain an advection equation because $\boldsymbol{B}$ vanishes, so the right-hand-side of equation (1.26) is zero. This shows that the ODEs (1.3) comprise the usual mean-field description of the dynamics when population size is infinite and probability density is just advected around trajectories of the ODEs. At the same time, the above derivation makes clear the relation between these ODEs (1.3) and the microscopic stochastic description when population size is finite. This is because equation (1.26) is an equation for the time evolution of the probability of being a state. It is also an example of a Fokker-Planck Equation, the vector $\boldsymbol{u}(\boldsymbol{x})$ is the drift term and $\boldsymbol{B}$ describes the diffusion.

Equation (1.26) is a Fokker-Planck (F-P) Equation, where $\boldsymbol{u}(\boldsymbol{x})$ represents its drift coefficient and $\boldsymbol{B}(\boldsymbol{x})$ is the diffusion coefficient. Following [30, 19], we know that there

is a connection between F-P equation and stochastic differential equation (SDE).

Definition 1.1 (SDE)**.** *In general, many variable systems of stochastic differential equations can be defined for n variables vector* $\boldsymbol{x}(t)$ *by*

$$\mathrm{d}\boldsymbol{x} = \boldsymbol{u}(\boldsymbol{x}, t)\mathrm{d}t + \boldsymbol{M}(\boldsymbol{x}, t)\mathrm{d}\boldsymbol{W}(t), \tag{1.28}$$

where $\boldsymbol{u} : \mathbb{R}^n \otimes \mathbb{R}^+ \to \mathbb{R}^n$, $\boldsymbol{M} : \mathbb{R}^n \otimes \mathbb{R}^+ \to \mathbb{R}^{n\times n}$, *the* $\boldsymbol{W}(t)$ *is a n-variable Wiener process.*

Definition 1.2 (Wiener process)**.** *We say* $\{W(t) : t \in \mathbb{R}^+\}$ *is a 1-variable Wiener process if it is a real-valued Gaussian process with continous sample paths, mean function* $\mu(t) = 0$*, and covariance function cov(s,t)=min{s,t}. Here Gaussian process means that* $\{W(t_1), W(t_2), ..., W(t_N)\}$ *follows a multivariate Gaussian distribution for any* $t_1, ..., t_N \in \mathbb{R}^+$ *and* $N \in \mathbb{N}$*. A n-variable Wiener process is defined by* $\boldsymbol{W}(t) = [W_1(t), ..., W_n(t)]^T$*.*

The name 'Wiener' refers to Norbert Wiener, who made a significant contribution to the mathematical theory. Wiener process is also frequently called 'Brownian motion' after Robert Brown, who identified Brownian motion in the movement of pollen particles [41]. Based on these concepts, the equivalence between F-P equations and SDEs is illustrated in the following theorem.

Theorem 1.3 (Connection between F-P equations and SDEs)**.** *The F-P equation for the conditional probability density* $p(\boldsymbol{x}, t|\boldsymbol{x}_0, t_0) \equiv p$ *is*

$$\partial_t p = -\sum_i \partial_i[\boldsymbol{u}_i(\boldsymbol{x})p] + \frac{1}{2}\sum_{i,j}\partial_i\partial_j\{[\boldsymbol{M}(\boldsymbol{x})\boldsymbol{M}^T(\boldsymbol{x})]_{ij}p\}. \tag{1.29}$$

It is equivalent to a multi-variable SDE:

$$\mathrm{d}\boldsymbol{x} = \boldsymbol{u}(\boldsymbol{x})\mathrm{d}t + \boldsymbol{M}(\boldsymbol{x})\mathrm{d}\boldsymbol{W}_t. \tag{1.30}$$

Proof(证明) . Please refer to Appendix A. □

According to theorem 1.3, the SDE which is equivalent to equation (1.26) is as follows:

$$\mathrm{d}\boldsymbol{x} = \boldsymbol{u}(\boldsymbol{x})\mathrm{d}t + \boldsymbol{M}(\boldsymbol{x})\mathrm{d}\boldsymbol{W}_t, \tag{1.31}$$

where $\boldsymbol{u}(\boldsymbol{x})$ is same as the term in equation (1.26) and $\boldsymbol{M}(\boldsymbol{x})$ satisfies $\boldsymbol{M}(\boldsymbol{x})\boldsymbol{M}(\boldsymbol{x})^T = \boldsymbol{B}(\boldsymbol{x})$ in equation (1.27).

In summary, the method introduced in this section shows how to obtain ODEs which correspond to the macroscopic dynamics and how to deduce SDEs which correspond to the macroscopic but still stochastic dynamics of the classic RPS model. In deriving the Fokker–Planck Equation, we truncated the expansion at second order, this is equivalent to making a Gaussian moment closure assumption. The correctness of the assumption in the limit of large N is established rigorously by a theorem of Kurtz that we will discuss in the next section. Meanwhile it also reveals the relation between coefficients of differential equation and the payoff matrix and rate coefficients in the chemical reactions described in section 1.3.1. Later, in chapter 2 and chapter 4, the method is widely used and extended in order to consider more complicated models.

1.3.3 Jump Matrix following Kurtz's theorem

There is another roughly equivalent path which takes us from the chemical reactions in (1.5) to a diffusion process (stochastic differential equation) of the form (1.31). This path follows Kurtz [37] in 1978 who focuses on the Markov process itself. In [5] Baxendale and Greenwood summarize the method through which the SDEs are derived from the Markov process of the chemical reactions. Let us introduce the method in this section briefly with the example RPS model. All notation follows section 1.3.2.

Each type of interaction (chemical reaction) causes the vector $\boldsymbol{n} \in \mathbb{N}^3$ to jump by a jump vector $\boldsymbol{s} \in \mathbb{Z}^3$. The stochastic rate $r(\boldsymbol{n}, \boldsymbol{s})$ (or $r(\boldsymbol{x}, \boldsymbol{s})$ with $\boldsymbol{x} := \boldsymbol{n}/N$) at which these jumps $\boldsymbol{n} \to \boldsymbol{n} + \boldsymbol{s}$ take place are the jump rates in the Markov model (the chemical reaction system). As before, let N be the sum of the components of $\boldsymbol{n}$; N is also a parameter representing the overall size of the system. The finite collection of possible jumps $\boldsymbol{s}$ is denoted by the stoichiometric matrix $\boldsymbol{S}$ and the corresponding jump rates are summarized into a vector $\boldsymbol{r}(\boldsymbol{x})$. For example, in the RPS model, the kth column of $\boldsymbol{S}$, $\boldsymbol{s}_k$, corresponds to the kth element of the vector $\boldsymbol{r}$:

$$\boldsymbol{S} = \begin{pmatrix} -1 & 0 & 1 \\ 1 & -1 & 0 \\ 0 & 1 & -1 \end{pmatrix}, \qquad \boldsymbol{r}(\boldsymbol{x}) = \begin{pmatrix} x_1 x_2 \\ x_2 x_3 \\ x_3 x_1 \end{pmatrix}. \tag{1.32}$$

Method of Kurtz

The Markov jump process determined by the chemical reaction is represented by Kurtz [37] as:

$$\boldsymbol{n}(t) = \boldsymbol{n}(0) + \sum_{\boldsymbol{s}_k \in \boldsymbol{S}} \boldsymbol{s}_k \mathbf{P}^{(\boldsymbol{s}_k)} \left(\int_0^t N r_k \mathrm{d}\tau \right). \tag{1.33}$$

Here $\{\mathbf{P}^{(\boldsymbol{s})}(\xi) : \xi \geq 0\}$ is a collection of independent rate 1 Poisson processes [5] and r_k which is the k-th element of $\boldsymbol{r}(x)$ describes the density dependent rate in the Markov system. Dividing by N gives:

$$\boldsymbol{x}(t) = \boldsymbol{x}(0) + \sum_{\boldsymbol{s}_k \in \boldsymbol{S}} \frac{1}{N} \boldsymbol{s}_k \mathbf{P}^{(\boldsymbol{s}_k)} \left(\int_0^t N r_k \mathrm{d}\tau \right). \tag{1.34}$$

The Poisson process here can be approximately written in the form:

$$\mathbf{P}^{(\boldsymbol{s})}(t) \approx t + W(t), \tag{1.35}$$

where $W(t)$ is a Wiener process. Replacing each Poisson process $\mathbf{P}^{(\boldsymbol{s}_k)}(t)$ with $t + W^{(\boldsymbol{s}_k)}(t)$ in (1.34) gives the equation:

$$\boldsymbol{x}(t) = \boldsymbol{x}(0) + \int_0^t \left(\sum_{\boldsymbol{s}_k \in \boldsymbol{S}} \boldsymbol{s}_k r_k \right) \mathrm{d}\tau + \sum_{\boldsymbol{s}_k \in \boldsymbol{S}} \boldsymbol{s}_k \frac{1}{N} W^{(\boldsymbol{s}_k)} \left(\int_0^t N r_k \mathrm{d}\tau \right), \tag{1.36}$$

and so the $\boldsymbol{x}(t)$ satisfies a stochastic differential equation of the form:

$$\mathrm{d}\boldsymbol{x}(t) = \left(\sum_{\boldsymbol{s}_k \in \boldsymbol{S}} \boldsymbol{s}_k r_k \right) \mathrm{d}t + \frac{1}{\sqrt{N}} \sum_{\boldsymbol{s}_k \in \boldsymbol{S}} \boldsymbol{s}_k \sqrt{r_k} \mathrm{d}W^{(\boldsymbol{s}_k)}(t). \tag{1.37}$$

A cleaner and more compact way of writing (1.37) is given by defining:

$$\boldsymbol{u}(\boldsymbol{x}) := \boldsymbol{S}\boldsymbol{r}(\boldsymbol{x}), \qquad \boldsymbol{B}_{i,j}(\boldsymbol{x}) := \sum_{\boldsymbol{s}_k \in \boldsymbol{S}} r_k s_{ki} s_{kj}\,, \tag{1.38}$$

where s_{ki} means the ith element of vector $\boldsymbol{s}_k$. Here $\boldsymbol{u}(\boldsymbol{x})$ is the vector field of means of the first term of the right side of equation (1.37) and $\boldsymbol{B}(\boldsymbol{x}) = \{\boldsymbol{B}_{i,j}(\boldsymbol{x})\}$ is the covariance function arising in the second term. In terms of $\boldsymbol{u}(\boldsymbol{x})$ and $\boldsymbol{B}(\boldsymbol{x})$, the SDE can be written as:

$$\mathrm{d}\boldsymbol{x}(t) = \boldsymbol{u}(\boldsymbol{x})\mathrm{d}t + \frac{1}{\sqrt{N}} \boldsymbol{M}(\boldsymbol{x}) \mathrm{d}\boldsymbol{W}(t), \tag{1.39}$$

where $\boldsymbol{W}(t)$ is a d-dimensional ($d = 3$ in the RPS model) Wiener process and the $d \times d$ matrix function $\boldsymbol{M}(\boldsymbol{x})$ is chosen so that $\boldsymbol{M}(\boldsymbol{x})\boldsymbol{M}^T(\boldsymbol{x}) = \boldsymbol{B}(\boldsymbol{x})$.

As $N \to \infty$ equation (1.39) only has the deterministic term ($\dot{\boldsymbol{x}} = \boldsymbol{S}\boldsymbol{r}(\boldsymbol{x})$), which is the REs (1.3) exactly. With a finite N, the stochastic term can also be interpreted with reference to the rate function $\boldsymbol{r}$ and the jump matrix $\boldsymbol{S}$.

This idea offers us a bridge between the interpretation of REs which are just derived from the payoff matrix and a set of chemical reactions for individual-level simulation

in some more complicated models. We will explore some detailed cases in section 2.1.2.

1.3.4 Power Spectral Density

The state variable $\boldsymbol{x}(t)$ above represents the dynamical evolution of the three species in the RPS-model. Now let us forget all the physical/biological background, and consider $\boldsymbol{x}(t)$ to be just a time series of a stationary stochastic process (see definition in equation (B.14)) with n variables. Assuming that a periodic/quasi-periodic fluctuation is observed in $\boldsymbol{x}(t)$, we try to work out its period or spectrum.

We would like to compute 'Power Spectral Density' (PSD) which describes how the power in a signal is distributed over frequencies. The PSD will help identify if there exists a most important frequency component to the signal $\boldsymbol{x}(t)$, i.e. whether $\boldsymbol{x}(t)$ has obvious periodic or quasi-periodic components. Mathematically, the definition of the PSD in the case of a scalar variable is:

Definition 1.4 (Power Spectral Density)**.** *The Power Spectral Density of the stochastic scalar process $x(t)$ is defined in two stages. First, define*

$$y(\omega) = \int_0^T \mathrm{e}^{-\mathrm{i}\omega t} x(t)\mathrm{d}t, \tag{1.40}$$

then the spectrum is defined by

$$\mathcal{P}(\omega) = \lim_{T\to\infty} \frac{1}{2\pi T} \left|y(\omega)\right|^2. \tag{1.41}$$

It is difficult to calculate the PSD directly from its definition in many cases. Gardiner's book [19] mentions that "the mean and the variance of $x(t)$ do not tell a great deal about the underlying dynamics of what is happening. What would be of interest is some quantity which is a measure of the influence of a value of x at time t on the value at time $t+\tau$. Such a quantity is the **autocorrelation function**." In fact, the autocorrelation function and the **spectrum** are closely connected, which is shown by Wiener-Khinchin theorem [86, 32] and offers another way of calculating the PSD.

Definition 1.5 (Autocorrelation function)**.** *Given a measurable quantity, a stochastic process $x(t)$ which fluctuates with time, its autocorrelation function is defined to be:*

$$G(\tau) = \lim_{T\to\infty} \frac{1}{T} \int_0^T x(t)x(t+\tau)\mathrm{d}t. \tag{1.42}$$

Theorem 1.6 (Wiener-Khinchin theorem)**.** *The Power Spectral Density of the stochas-*

tic process $x(t)$ is the Fourier Transform of its autocorrelation function

$$\mathcal{P}(\omega) = \frac{1}{2\pi}\int_{-\infty}^{\infty} \mathrm{e}^{-\mathrm{i}\omega\tau} G(\tau)\mathrm{d}\tau \tag{1.43}$$

where the autocorrelation function $G(\tau)$ of $x(t)$ is defined above.

Proof(证明) . Please refer to Appendix B. □

Theorem 1.7. *In general, the definitions and theorem is also valid in many-variable systems. If $\boldsymbol{x}(t)$ is given by a linear stochastic differential equation in the form of:*

$$\mathrm{d}\boldsymbol{x} = \boldsymbol{A}\boldsymbol{x}\mathrm{d}t + \boldsymbol{M}\mathrm{d}\boldsymbol{W}(t), \tag{1.44}$$

where $\boldsymbol{A}$ and $\boldsymbol{M}$ are constant matrices with $\boldsymbol{M}\boldsymbol{M}^T = \boldsymbol{B}$ and $\boldsymbol{B}$ is also a constant matrix and $\boldsymbol{W}(t)$ is a multivariate Wiener process. Then the Power Spectral Density of the stochastic process $\boldsymbol{x}(t)$ is

$$\boldsymbol{\mathcal{P}}(\omega) = \frac{1}{2\pi}(\boldsymbol{A} - \mathrm{i}\omega\boldsymbol{I})^{-1}\boldsymbol{B}(\boldsymbol{A} - \mathrm{i}\omega\boldsymbol{I})^{-\dagger}. \tag{1.45}$$

The stochastic process which is define by the SDE (1.44) *is called multivariate Ornstein–Uhlenbeck process.*

Proof(证明) . Please refer to Appendix B. □

In summary, the Power Spectral Density can be theoretically computed in order to investigate the frequency response observed in many models, assuming that these oscillations can be described by SDEs in the form of Ornstein-Ulenbeck Process (1.44). In chapter 2 and chapter 4 the conclusion (1.45) is applied directly.

1.3.5 Random Matrix and Cavity method

In this subsection we consider a more general form of autocatalytic network is defined on a set of N species $\{X_1, X_2, ..., X_N\}$. As before, we assume that all the interactions occur only in pairs (X_i, X_j). We can use chemical reactions to show these relations: $X_i + X_j \xrightarrow{r_{ij}} 2X_j$. The rate of reactions r_{ij} is a component of the reaction rate matrix $\boldsymbol{R} = \{r_{ij}\}$.

Random Matrix

Because we lack specific knowledge of the interaction network, we consider an ensemble of interaction matrices. This idea is inspired by a modelling paradigm in

ecology, going back to the seminal paper of May on the stability of complex systems [46]. We assume that the number of chemical species, N, is large and the total number of reactions is $M = cN/2$, so that the mean number of reactions, c, per chemical species obeys $1 \ll c \ll N$. Therefore the average degree of the autocatalytic network is c as well. Then the reaction rates are chosen to be independently identically distributed (IID) with mean $\mathbb{E}[r] = \mu_1$ and raw second moment $\mathbb{E}[r^2] = \mu_2$ where r is the rate of a reaction. In numerical experiments we generate IID rates and project $\boldsymbol{R}$ into the space of row/column balanced matrices where 'balance' means that the number of nonzero entries allocated to row is same as that allocated to column. Note that we assume bidirectional reactions are vanishingly rare (such as is food webs, for example), so that generally $\boldsymbol{R}_{ij}\boldsymbol{R}_{ji} = 0$. The algorithm for generating the reaction rate matrix $\boldsymbol{R}$ is as follows.

Algorithm 1.2 (Generating a random matrix for reactions)**.**

1. *Given the number of species N, the mean number of reactions per species c ($c \mod 4 = 0$ for convenience of balanced projection), and μ_1, μ_2 as defined in last paragraph (i.e. the first and second moments of the probability distributions for rates).*

2. *Define two numbers a and b by*

$$a = 2\ln\mu_1 - \frac{1}{2}\ln\mu_2, \qquad b = \sqrt{\ln\mu_2 - 2\ln\mu_1} \tag{1.46}$$

3. *Generate an $N \times N$ matrix $\boldsymbol{R}$ with initial value $\mathbf{0}$, i.e. generate N independent vertices $\{v_1, ..v_N\}$.*

4. *For the i–th row, choose $c/4$ numbers in the range $\{1, ..., N\}\backslash\{i\}$ randomly, and put these numbers in a set J_r, i.e. choose $c/4$ vertices which are disconnected from v_i.*

5. *For each $j \in J_r$, choose the reaction rate $\boldsymbol{R}_{ij}$ at random from a distribution on $\mathbb{R}^+$. We will consider two examples: 'log–normal' and 'exponential' generated via*

$$\boldsymbol{R}_{ij} = \begin{cases} \exp(a + b\xi_1) & \text{for lognormal IID} \quad \xi_1 \sim \mathcal{N}(0,1); \\ -\mu_1 \ln\xi_2 & \text{for exponential IID} \quad \xi_2 \sim \mathcal{U}(0,1); \end{cases} \tag{1.47}$$

6. *For the i–th column, repeat step 4 and 5 to get $\boldsymbol{R}_{ji}$ (here we obtain a set J_c, make sure $J_r \cap J_c = \varnothing$), i.e. draw a directed edge from v_j to v_i with weight $\boldsymbol{R}_{ji}$.*

7. *Iterate steps 4, 5 and 6 for $i = 1...N$, then we get a graph with N vertices, and $cN/2$ directed edges.*

After generating the random matrix $\boldsymbol{R}$ which satisfies all the rules above, we obtain the simplest possible model for a random autocatalytic reaction network.

Cavity Method

In the last section we described a convenient way to calculate the power spectral density of a stochastic process $\boldsymbol{x}(t)$ given by a SDE. However, when the coefficient matrices $\boldsymbol{A}$ and $\boldsymbol{B}$ are high-dimensional, random and sparse, the calculation of $\boldsymbol{\mathcal{P}}(\omega)$ in (1.45) could be very tough. When the reaction matrix is a high-dimensional random matrix $\boldsymbol{R}$ (e.g. an autocatalytic network, generated by algorithm 1.2), the payoff matrix would be $\boldsymbol{P} = \boldsymbol{R}^T - \boldsymbol{R}$ and then the coefficient matrices $\boldsymbol{A}$ and $\boldsymbol{B}$ can both be derived from $\boldsymbol{P}$ through the techniques described in section 1.3.2 and 1.3.3. In this section we briefly introduce a useful different method, the cavity method, which has been widely used in many applications, to solve the calculation problem of $\boldsymbol{\mathcal{P}}(\omega)$, when the system is high-dimensional and sparse.

The cavity method was initially invented by M. Mézard, Giorgio Parisi and Miguel Angel Virasoro in 1985 to deal with the Sherrington Kirkpatrick model of spin glasses [55]. Since then, the cavity method has been applied much more widely [54], for instance, in optimization problems, the K-satisfiability problem [56] and their variants. In this thesis I will use the cavity method just for a matrix calculation related to Random Matrix Theory (RMT). In [73] and [72], the cavity method is applied to analyse the spectral density of sparse symmetric matrices and non-Hermitian sparse matrices. The Wigner semicircle law for Gaussian matrices [73], the Marĉenko-Pastur law for covariance matrices [73] and the generalized Girko's law for non-Hermitian sparse random matrices [72] are all recovered within this method easily. A more recent example, in the study of the modularity and stability of ecological communities [23], the cavity method was shown to be a simple and effective way to calculate the distribution of the eigenvalues of a random community network. Similarly, for large random ecosystems, the method has helped in the analysis of the effects of population abundance on the stability of random interacting networks [20]. The general technique used in [23, 20] is to study the spectrum of the community matrix analytically through the cavity method. Motivated by these papers, we introduce the cavity method here in order to help analyse the power spectral density $\boldsymbol{\mathcal{P}}(\omega)$.

Consider a system of N dynamical variables (which are spins in the original Sherrington-Kirkpatrick model) $\boldsymbol{z} = (z_1, ..., z_N)$. They are arranged in a graph , with interactions between two neighbors z_i and z_j given by a bond strength A_{ij}. Actually

a tree-like graph $G = (V, E)$, which means there are long loops in the graph, can illustrate this model by assuming the dynamical variables reside on the vertices of the graph G and interact in pairs according to the edges of the graph. The key idea of the cavity method is to exploit the topological structure of the underlying network. The assumption that G is a tree is key.

Following [73] and [88], we consider the joint probability density function (JPDF) $P(\boldsymbol{z})$ of the variables $\boldsymbol{z}$. We assume $P(\boldsymbol{z})$ can be factorised into terms $\{p_{ij}\}$ associated to the edges of G and $\{p_i\}$ associated to the vertices:

$$P(\boldsymbol{z}) = \frac{1}{\mathcal{Z}} \prod_{i,j \in E} p_{ij}(z_i, z_j) \prod_{i \in V} p_i(z_i). \tag{1.48}$$

and these two sets of terms $\{p_{ij}\}$ and $\{p_i\}$ are determined by the bond strength A_{ij} specifically. Then consider the same system with the modified graph $G^{(i)} = (V^{(i)}, E^{(i)})$, where $G^{(i)}$ is the subgraph of G in which vertex i is removed. This subgraph is called the cavity graph. If we use the notation $\boldsymbol{z}^{(i)}$ to represent the vector of variables of $\boldsymbol{z}$ with the i-th component removed, the JPDF of $\boldsymbol{z}^{(i)}$ is given by:

$$P^{(i)}(\boldsymbol{z}^{(i)}) = \frac{1}{\mathcal{Z}^{(i)}} \prod_{j,k \in E^{(i)}} p_{jk}(z_j, z_k) \prod_{j \in V^{(i)}} p_j(z_j). \tag{1.49}$$

Here $\mathcal{Z}$ and $\mathcal{Z}^{(i)}$ are both normalization coefficients.

At the same time, by the definition of marginal probability, the probability distribution for the single variable z_i is given by:

$$\begin{aligned} P_i(z_i) &= \int P(\boldsymbol{z}) \prod_{j \neq i} \mathrm{d}z_j \\ &\propto p_i(z_i) \int \prod_{j \sim i} (p_{ij}(z_i, z_j) \mathrm{d}z_j) \int \prod_{l \neq i} p_l(z_l) \prod_{l,k \neq i} p_{lk}(z_l, z_k) \prod_{l \in V^{(i \cup \mathcal{N}_i)}} \mathrm{d}z_l, \\ &\propto p_i(z_i) \int \prod_{j \sim i} (p_{ij}(z_i, z_j) \mathrm{d}z_j)\, P^{(i)}_{\mathcal{N}_i}(\boldsymbol{z}_{\mathcal{N}_i}), \end{aligned} \tag{1.50}$$

where $\int \prod_i \mathrm{d}z_i$ represents $\int \cdots \int \mathrm{d}z_1 \cdots \mathrm{d}z_n$. Here we write $\mathcal{N}_i$ for the set of neighbours of the vertex i and $j \sim i$ means that there exists an edge $e_{ij} \in E$ or equivalently, that $j \in \mathcal{N}_i$. With writing $\mathcal{Z}_i = \mathcal{Z}/\mathcal{Z}^{(i)}$, we get the $P_i(z_i)$ from (1.50):

$$P_i(z_i) = \frac{1}{\mathcal{Z}_i} p_i(z_i) \int P^{(i)}_{\mathcal{N}_i}(\boldsymbol{z}_{\mathcal{N}_i}) \prod_{j \in \mathcal{N}_i} p_{ij}(z_i, z_j) \mathrm{d}z_j \,. \tag{1.51}$$

Now we are at the key step of the cavity method. If the distribution $P^{(i)}_{\mathcal{N}_i}$ could be

calculated, of course we could get the individual distribution $P_i(z_i)$ from (1.51).

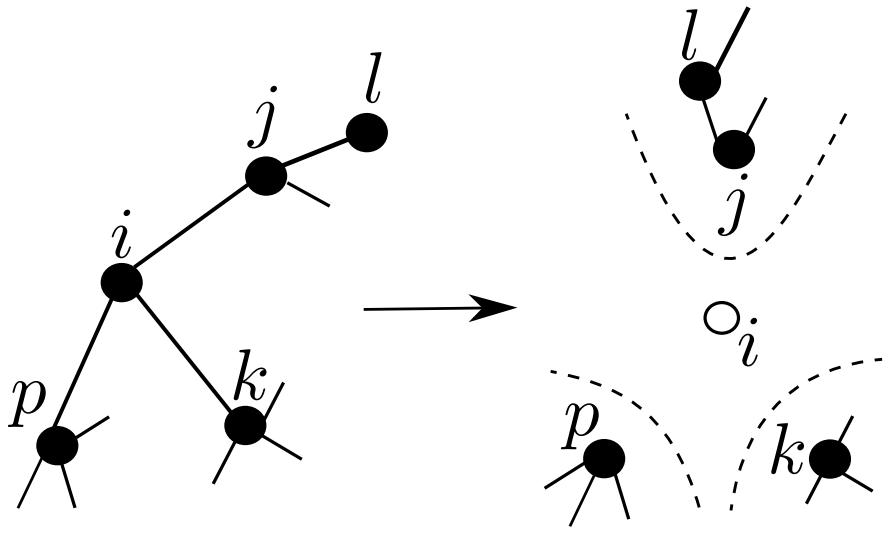

Figure(图) 1-4: The left is a tree-like graph G. If vertex i is removed from G, obviously each vertex in its neighbourhood is in different connected components. Particularly, if j is removed, for the vertex l in the right, it is as if i is also removed at the same time. This is important for the validation of the second equivalence in (1.54).

At the beginning, we assumed that the graph G is tree-like, which is illustrated in figure 1-4. After removing vertex i, we can find that every vertex in the neighbourhood $\mathcal{N}_i$ becomes a root of a separated tree. Intuitively the distribution $P^{(i)}_{\mathcal{N}_i}$ could be expressed as the product of the probability of each neighbour because they belong to independent components respectively:

$$P^{(i)}_{\mathcal{N}_i}(\boldsymbol{z}_{\mathcal{N}_i}) = \prod_{j\sim i} P^{(i)}_j(z_j), \tag{1.52}$$

so the question is interpreted to calculate $P^{(i)}_j(z_j)$. Similar to the form of (1.51), $P^{(i)}_j(z_j)$ is also decided by its neighbours:

$$P^{(i)}_j(z_j) = \frac{1}{\mathcal{Z}^{(i)}_j} p_j(z_j) \int P^{(j)(i)}_{\mathcal{N}_j\setminus i}(\boldsymbol{z}_{\mathcal{N}_j\setminus i}) \prod_{l\in\mathcal{N}_j\setminus i} p_{jl}(z_j, z_l)\mathrm{d}z_l\,. \tag{1.53}$$

Naturally, the term $P^{(j)(i)}_{\mathcal{N}_j\setminus i}(\boldsymbol{z}_{\mathcal{N}_j\setminus i})$ could be written in the form of product which is similar to equation (1.52) because it happens in the graph $G^{(j)(i)}$, after removing vertex j the rest components are still disconnected:

$$P^{(j)(i)}_{\mathcal{N}_j\setminus i}(\boldsymbol{z}_{\mathcal{N}_j\setminus i}) = \prod_{l\in\mathcal{N}_j\setminus i} P^{(j)(i)}_l(z_l) = \prod_{l\in\mathcal{N}_j\setminus i} P^{(j)}_l(z_l)\,. \tag{1.54}$$

Here the second equivalence $P_l^{(j)(i)}(z_l) = P_l^{(j)}(z_l)$ is valid since when vertex j is removed, the vertices i and l reside in different connected components (as shown in figure 1-4). Finally, we conclude that $P_j^{(i)}(z_j)$ and $P_i(z_i)$ can be written in the form:

$$P_j^{(i)}(z_j) = \frac{1}{\mathcal{Z}_j^{(i)}} p_j(z_j) \int \prod_{l \in \mathcal{N}_j \backslash i} p_{jl}(z_j, z_l) P_l^{(j)}(z_l) \mathrm{d}z_l \,, \tag{1.55}$$

$$P_i(z_i) = \frac{1}{\mathcal{Z}_i} p_i(z_i) \int \prod_{j \in \mathcal{N}_i} p_{ij}(z_i, z_j) P_j^{(i)}(z_j) \mathrm{d}z_j \tag{1.56}$$

For all possible pairs (i, j) the equations in the form of (1.55) define a self-consistent scheme for the cavity distribution $P_j^{(i)}(z_j)$. If they are solved, then using equation (1.56) we may calculate $P_i(z_i)$.

It is very difficult to solve cavity equations directly in many cases: it is a system of $2|E|$ equations. For some tractable events, the cavity distributions can be parameterised (sometimes approximately) by finitely many parameters. By reducing the cavity equations to a set of self-consistent equations for the parameters, the cavity distribution could be solved analytically or numerically.

The derivations above are all based on the assumption that G is a tree-like graph. But actually the cavity equation (1.55) could be applied to any graph, tree-like or not. How good the approximation of the correct distribution this is depends on the degree of the correlations among the vertices. The less they are correlated, the better the approximation is. For example, the cavity method works well in large random graphs drawn from a tree-like matrix [73] and in [12] the asymptotic correctness of the cavity method for the Ising model on locally tree-like graphs has been proved.

For a fully connected graph, the TAP approach (invented by Thouless, Anderson and Palmer) offers the idea of still considering the cavity method as a natural analogue [79]. For the case of Wigner random matrices, with the result of TAP approach, the cavity method can be used to derive the semicircle law; this is shown in [73]. The key point of the approach is to consider that the bond strengths $\{A_{ij}\}$ to form an $N \times N$ Hermitian matrix with independent entries. The mean of these entries is zero and the variance is $1/N$. Although the graph presented by the matrix is not tree-like (it is almost fully connected), the cavity method is still valid in the large N limit. The contribution from the neighbourhood to the local field of a vertex is approximately negligible because the correlation between the connected vertices is very small and tends to zero when $N \to \infty$. This method is applied in chapter 4.

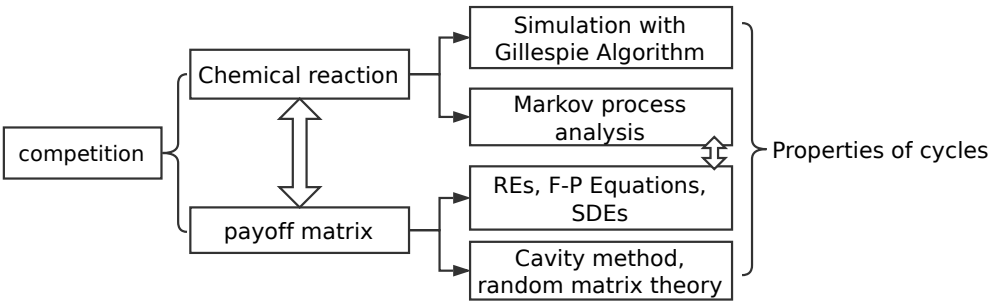

Figure(图) 1-5: The flow diagram shows the logical order of these methods.

1.3.6 Method Summary

Figure 1-5 briefly illustrates the links between the various methods used throughout the thesis. First of all, there are competitions in species interactions. Then on the population level, the payoff matrix could be used to describe the competitions among several species; on the individual level, we use chemical reactions to show the competitive relationships. These two expressions are intrinsically equivalent. Sections 1.3.2 and 1.3.3 introduce how to convert chemical reactions to differential equations, which are same as the equations derived from the payoff matrix. Section 2.1.2 also shows how to deduce corresponding chemical reactions from existing differential equations which are derived from a payoff matrix.

The right half of fig 1-5 explains how these methods are organised. We use the Gillespie Algorithm to simulate clearly the competition and evolution with chemical reaction scheme. At the same time, this scheme also offers us ideas for stochastic process analysis. Replicator equations can be derived from the expression of payoff matrix, while Fokker–Planck equations and SDE can be obtained by stochastic process analysis. Then we can easily compare the stochastic dynamics to the deterministic dynamics, and analyse the effects from the demographic noise. Last, but not least, the cavity method offers a very helpful approach to dealing with cases that are sparse, random and high-dimensional.

In summary, in this thesis we use combinations of the above methods to study oscillations in multi-species competitions.

Chapter 2

Three Species Competition 三种群竞争

In this chapter we consider in detail the Rock-Paper-Scissors (RPS) model discussed in Chapter 1. Recall the classic RPS model which was introduced in section 1.3.1. Analysis which is based on the mean-field rate equations shows that when the population of the species involved is infinite and well-mixed, the proportion of the three species formed a regular oscillation.

At the same time, in the micro-perspective, although there are some macroscopic rules, the specific individual's behaviour is still random. Through the stochastic simulation algorithm 1.1 in section 1.3.1, we find that when the size of population is finite, the original closed orbit will be broken, the three species will eventually have only one surviving, and we cannot predict which one (especially in the case of all the species having the same reproduction-predation rate).

For the purpose of promoting species diversity, we hope that even in stochastic simulations, it is possible to find some conditions for stable coexistence of the three species. The introduction of another widely occurring factor in nature, mutation, satisfies our requirement to attempt stabilise the dynamics. This is observation, that we wish to avoid the absorbing states in which only one species remains, motivates the addition of mutation and the form of the model considered in this chapter.

2.1 Two Updated Models based on the RPS Model

Another common variant [51, 69] of the RPS model introduces the additional mechanism of mutation between the three strategies, occurring between any pair with equal frequency (shown in figure 2-1).

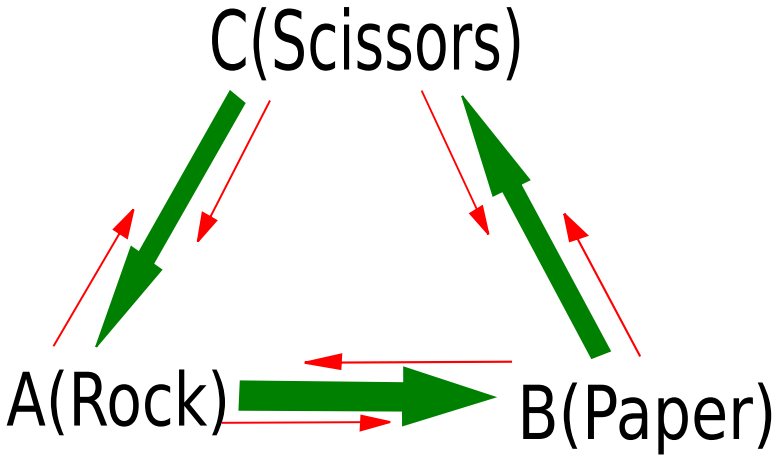

Figure(图) 2-1: Illustration of the Rock–Paper–Scissors interaction in the presence of mutations. Green arrows indicate cases in which the state at the head of the arrow wins over the state at the tail of the arrow. Thin (red) arrows indicate possible mutations between states.

2.1.1 Symmetric RPS Model with Mutation

As we now include mutation, the individual-based simulations must now follow the chemical reactions (1.5) together with the mutation reactions :

$$\begin{aligned} A \xrightarrow{\mu} B, \quad B \xrightarrow{\mu} C, \quad C \xrightarrow{\mu} A, \\ A \xrightarrow{\mu} C, \quad B \xrightarrow{\mu} A, \quad C \xrightarrow{\mu} B. \end{aligned} \tag{2.1}$$

which are taken to all occur at the same rate as each other, denoted by μ. In our assumption, the mutation rates are same in order to keep the cyclic symmetry of the three species. In other specific models, the rates could be different with each other [80].

Rate Equations

Mutation affects the rate of change of strategy i over time since the strategies other than i will contribute new players of i at rates μ while i will lose players at a rate given by $2\mu x_i$ as these players switch to a different strategy. The combined effects of the replicator dynamics together with mutations between strategies gives rise to the model equations (for an infinitely large population)

$$\begin{aligned} \dot{x}_1 &= x_1(x_3 - x_2) + \mu(x_2 + x_3 - 2x_1), \\ \dot{x}_2 &= x_2(x_1 - x_3) + \mu(x_1 + x_3 - 2x_2), \\ \dot{x}_3 &= x_3(x_2 - x_1) + \mu(x_1 + x_2 - 2x_3). \end{aligned} \tag{2.2}$$

Obviously, there is a single interior equilibrium point $\boldsymbol{x}^* = (1/3, 1/3, 1/3)$.

Consider the linear stability of the equilibrium point. Because of the conservation $x_1 + x_2 + x_3 = 1$, the ODEs can be simplified to read:

$$\begin{aligned} \dot{x}_1 &= x_1(1 - x_1 - 2x_2) + \mu(1 - 3x_1), \\ \dot{x}_2 &= x_2(2x_1 + x_2 - 1) + \mu(1 - 3x_2). \end{aligned} \tag{2.3}$$

So the Jacobian matrix about the equilibrium $\boldsymbol{x}^* = (1/3, 1/3, 1/3)$ is:

$$J^* = \begin{pmatrix} -\frac{1}{3} - 3\mu & -\frac{2}{3} \\ \frac{2}{3} & \frac{1}{3} - 3\mu \end{pmatrix} \tag{2.4}$$

and the eigenvalues of this matrix are $\lambda_\pm = \lambda \pm \mathrm{i}\omega$, where $\lambda = -3\mu$ and $\omega = \frac{\sqrt{3}}{3}$. We observe that $\lambda < 0$ because $\mu > 0$, which means that $\boldsymbol{x}^*$ is a stable equilibrium.

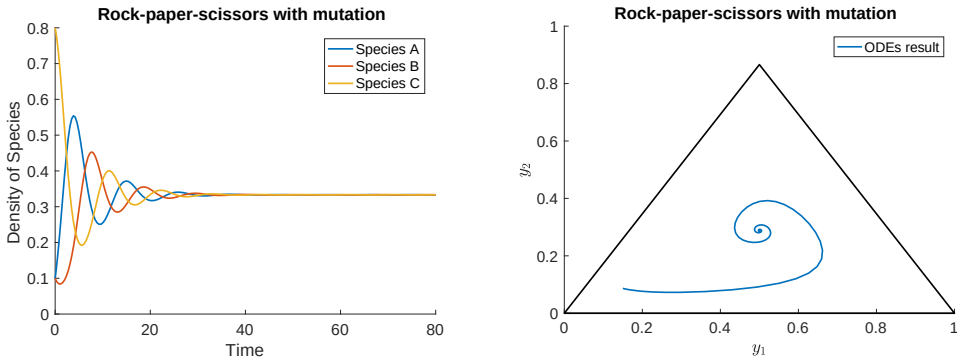

(a) (b)

Figure(图) 2-2: Numerical result of ODEs (2.2). (a) ODEs solution converges to the equilibrium with $\mu = 0.05$. (b) ODEs solution spirals in towards the equilibrium with $\mu = 0.05$. Horizontal direction $y_1 = x_1 + x_2/2$ and vertical direction $y_2 = \sqrt{3}x_2/2$.

Figure 2-2 shows typical numerical solutions of the ODEs (2.2) with the parameter value $\mu = 0.05$ and initial condition $\boldsymbol{x}(0) = (0.1, 0.1, 0.8)$. The trajectory spirals in towards the equilibrium in Figure 2-2(b), which directly illustrates its stability.

Stochastic Simulations: Appearance of a sustained oscillation

We now turn to a large but finite population. Through the Gillespie algorithm introduced in section 1.3.1, we simulate the chemical reactions (1.5) and (2.1) with a total system size $N = 2^{16}$, parameter $\mu = 0.05$ and the same initial value $\boldsymbol{x}(0) = (0.1, 0.1, 0.8)$. The comparison between the simulation result and the numerical solution of the ODEs (2.2) is shown in Figure 2-3. Roughly speaking, the simulation results

and numerical solution has a similar evolution tendency. However, there is a sustained oscillation around the equilibrium in the simulation results, after the evolution has converged to a neighbourhood of the equilibrium point.

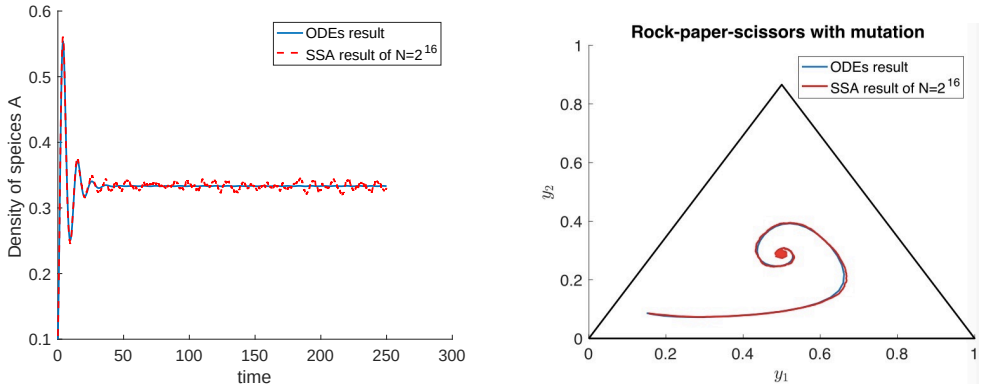

(a) (b)

Figure(图) 2-3: Stochastic simulation results are compared to ODEs numerical solution. (a) Stochastic simulation result always fluctuates around the equilibrium periodically. (b) Comparison between the two methods: they both spiral into the equilibrium with $\mu = 0.05$. Horizontal direction $y_1 = x_1 + x_2/2$ and vertical direction $y_2 = \sqrt{3}x_2/2$.

Analysis of the sustained oscillation

The persistent oscillation of trajectories around the interior equilibrium is caused by the demographic noise. This must be the case since the deterministic dynamics shows exponentially decaying oscillations that do not persist as $t \to \infty$. When the simulation size is finite, according to the derivation in section 1.3.2 (Fokker-Planck Equation) and section 1.3.3 (Kurtz's theory), the diffusion process cannot be ignored. The stoichiometric matrix here is

$$\boldsymbol{S} = \begin{pmatrix} -1 & 0 & 1 & -1 & -1 & 0 & 1 & 1 & 0 \\ 1 & -1 & 0 & 1 & 0 & -1 & -1 & 0 & 1 \\ 0 & 1 & -1 & 0 & 1 & 1 & 0 & -1 & -1 \end{pmatrix}, \tag{2.5}$$

and corresponding rate vector is

$$\boldsymbol{r} = (x_1x_2, x_2x_3, x_3x_1, \mu x_1, \mu x_1, \mu x_2, \mu\mu x_2, \mu x_3, \mu x_3) \ . \tag{2.6}$$

Applying Kurtz's theorem in equation (1.38), enables us to compute the drift coefficient and diffusion term for this case. The dynamics including the microscopic stochastic behaviour now can be described by Stochastic Differential Equation (SDE) in the same

form as (1.31):

$$\mathrm{d}\boldsymbol{x} = \boldsymbol{u}(\boldsymbol{x})\mathrm{d}t + \boldsymbol{M}(\boldsymbol{x})\mathrm{d}\boldsymbol{W}_t,$$

where $\boldsymbol{M}\boldsymbol{M}^T = \boldsymbol{B}$, and the drift term is

$$\boldsymbol{u}(\boldsymbol{x}) = \begin{pmatrix} x_1x_3 - x_1x_2 + \mu(x_2 + x_3 - 2x_1) \\ x_2x_1 - x_2x_3 + \mu(x_1 + x_3 - 2x_2) \\ x_3x_2 - x_3x_1 + \mu(x_1 + x_2 - 2x_3) \end{pmatrix} \quad \boldsymbol{B}(\boldsymbol{x}) := \frac{1}{N}\left(\boldsymbol{B}_1(\boldsymbol{x}) + \mu\boldsymbol{B}_2(\boldsymbol{x})\right) \tag{2.7}$$

where the two contributions to the matrix of diffusion coefficients are

$$\boldsymbol{B}_1(\boldsymbol{x}) = \begin{pmatrix} x_1(x_2 + x_3) & -x_1x_2 & -x_1x_3 \\ -x_1x_2 & x_2(x_1 + x_3) & -x_2x_3 \\ -x_1x_3 & -x_2x_3 & x_3(x_1 + x_2) \end{pmatrix} \tag{2.8}$$

from the deterministic competitive dynamics, and

$$\boldsymbol{B}_2(\boldsymbol{x}) = \begin{pmatrix} 2x_1 + x_2 + x_3 & -x_1 - x_2 & -x_1 - x_3 \\ -x_1 - x_2 & x_1 + 2x_2 + x_3 & -x_2 - x_3 \\ -x_1 - x_3 & -x_2 - x_3 & x_1 + x_2 + 2x_3 \end{pmatrix} \tag{2.9}$$

from the mutation dynamics.

The oscillation occurs around the inner equilibrium $\boldsymbol{x}^* = (1/3, 1/3, 1/3)$. Linearising the drift term $\boldsymbol{u}(\boldsymbol{x})$ in the SDE at the point $\boldsymbol{x}^*$, we get that:

$$\boldsymbol{u}(\boldsymbol{x}) \approx \boldsymbol{A}(\boldsymbol{x} - \boldsymbol{x}^*), \tag{2.10}$$

where

$$\begin{aligned} \boldsymbol{A} := \boldsymbol{J}(\boldsymbol{x})|_{\boldsymbol{x}^*} &= \begin{pmatrix} x_3 - x_2 - 2\mu & -x_1 + \mu & x_1 + \mu \\ x_2 + \mu & x_1 - x_3 - 2\mu & -x_2 + \mu \\ -x_3 + \mu & x_3 + \mu & x_2 - x_1 - 2\mu \end{pmatrix}\Bigg|_{\boldsymbol{x}^*} \\ &= \begin{pmatrix} -2\mu & -1/3 + \mu & 1/3 + \mu \\ 1/3 + \mu & -2\mu & -1/3 + \mu \\ -1/3 + \mu & 1/3 + \mu & -2\mu \end{pmatrix} \end{aligned} \tag{2.11}$$

with $\boldsymbol{J}(\boldsymbol{x})$ is the Jacobian matrix of the drift function $\boldsymbol{u}(\boldsymbol{x})$. Since we are considering dynamics near $\boldsymbol{x}^*$, $|\boldsymbol{x} - \boldsymbol{x}^*|$ is assumed to be small, in which case the linearised dynamics should be a quantitatively good approximation to the full nonlinear flow. Since the equilibrium point $\boldsymbol{x}^*$ is hyperbolic we know from the Hartman–Grobman theorem that the nonlinear and linearised flows are topologically equivalent. For the linearised SDE

we also evaluate the diffusion matrix $\boldsymbol{M}$ at $\boldsymbol{x}^*$ so that it becomes constant in our approximation:

$$\mathrm{d}\boldsymbol{y} = \boldsymbol{A}\boldsymbol{y}\mathrm{d}t + \boldsymbol{M}(\boldsymbol{x}^*)\mathrm{d}\boldsymbol{W}(t),$$

where $\boldsymbol{y} := \boldsymbol{x} - \boldsymbol{x}^*$ and $\boldsymbol{M}\boldsymbol{M}^T = \boldsymbol{B}(\boldsymbol{x}^*)$ which is

$$\boldsymbol{B}(\boldsymbol{x}^*) = \frac{1}{N}\begin{pmatrix} 2/9 & -1/9 & -1/9 \\ -1/9 & 2/9 & -1/9 \\ -1/9 & -1/9 & 2/9 \end{pmatrix} + \frac{\mu}{N}\begin{pmatrix} 4/3 & -2/3 & -2/3 \\ -2/3 & 4/3 & -2/3 \\ -2/3 & -2/3 & 4/3 \end{pmatrix}. \tag{2.12}$$

Following on from the discussion about the power spectral density in section 1.3.4, the spectral density of $\boldsymbol{x}(t)$ of the sustained oscillation can be computed theoretically from equation (1.45):

$$\boldsymbol{\mathcal{P}}(\omega) = \frac{1}{2\pi}(\boldsymbol{A} - \mathrm{i}\omega\boldsymbol{I})^{-1}\boldsymbol{B}(\boldsymbol{A} - \mathrm{i}\omega\boldsymbol{I})^{-\dagger},$$

where $\boldsymbol{A}$ and $\boldsymbol{B}$ are defined in (2.11) and (2.12). We focus first on the element at position $(1,1)$ of $\boldsymbol{\mathcal{P}}(\omega)$, denoted by $\mathcal{P}_{11}$. It describes the frequency spectrum of $x_1(t)$. Using the above formula and (2.8) to (2.12) we obtain directly

$$\begin{aligned} \mathcal{P}_{11} &= \frac{1}{2N\pi}\frac{(4/3\mu + 2/9)(9\mu^2 + 1/3 + \omega^2)}{(9\mu^2 + 1/3 - \omega^2)^2 + 36\omega^2\mu^2}, \\ &= \frac{1}{3N\pi}\frac{3\omega^2(6\mu+1) + 18\mu^2(9\mu+1) + (3\mu+1)^2}{3\omega^2(3\omega^2 + 54\mu^2 - 2) + (27\mu^2+1)^2}. \end{aligned} \tag{2.13}$$

Note that $\mathcal{P}_{22} = \mathcal{P}_{33} = \mathcal{P}_{11}$ because the model is cyclically symmetric.

$\mathcal{P}_{11}$ has a peak at the point ω_0 when the derivative $\mathcal{P}_{11}' = 0$ (see Figure 2-4). This can be computed analytically, giving

$$\omega_0 = \left(-9\mu^2 - \frac{1}{3} + \frac{1}{2}\sqrt{\frac{16}{9} + 48\mu^2}\right)^{1/2}. \tag{2.14}$$

Equation (2.14) shows the main angular speed of the oscillation occurring at the equilibrium $(1/3, 1/3, 1/3)$. When $\mu = 0$, $\omega_0 = \frac{\sqrt{3}}{3}$, equal to the imaginary part of eigenvalues of Jacobian Matrix J^* (2.4) at the equilibrium. This is reasonable because intrinsically they describe the same thing.

The red line in Figure 2-4 is the stochastic simulation result in the frequency-domain obtained by applying the Fast Fourier Transform to the time series $\boldsymbol{x}(t)$. This figure shows that the calculation results based on SDEs and power spectral density agrees with the simulation result well, as we hoped. This result confirms that the

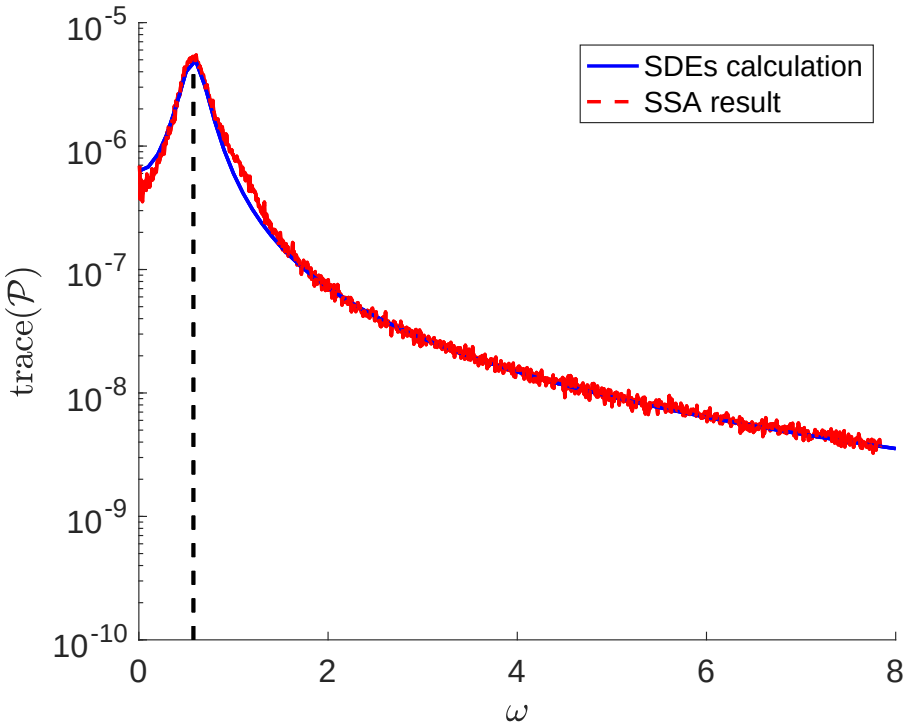

Figure(图) 2-4: The power spectral density $\mathcal{P}(\omega)$ for a time series $\boldsymbol{x}(t)$ resulting from an individual-based simulation of the 3 species RPS system with mutation, using the Gillespie algorithm, for 20 sample simulations. The population size of the simulations is $N = 2^{16}$, the mutation rate here is $\mu = 0.05$, the time step of the data recorded in simulations is 0.05, and the last 10000 time points recorded are used for the FFT. The dominant frequency ω_0, at which the theory predicts $\mathcal{P}$ to have a maximum, is indicated by the vertical dashed line.

linearised SDE is a good approximation to the individual-based stochastic dynamics when N is large and μ is small.

Short Summary

The RPS with mutation model is a cyclic-dominance model with a fixed mutation rate. This avoids the case in which one species dominates the whole system in the stochastic simulation. The dynamics can be described by deterministic ODEs at the population level. At the same time, the SSA describes the microscopic dynamic at the individual level and is a stochastic method.

For the RPS with mutation model the two approaches have some agreement and some disagreements. Numerical solutions of ODEs agree roughly with the stochastic simulation results, especially in the stability of the equilibrium: they both spiral into the equilibrium and near the equilibrium point. However, disagreement also exists: the

SSA result has a quasi-periodic oscillation around the equilibrium, rather than staying at the point exactly in the deterministic result.

Stochastic Differential Equations (SDEs) link the two methods together. They present a more precise description than the ODEs since the SDEs take account of the large but finite population size. The SDEs not only predict the oscillation around the equilibrium, but also predict the frequency of the oscillation. Finally, we show that the theoretical calculation of the frequency of the oscillation fits the simulation results well. We note that this combination of approaches has been used in other applications as well [5]. Our results agree with those of previous authors. In the next subsection we will discuss an asymmetric model, which shows different evolutionary behaviours.

2.1.2 Asymmetric RPS Model with Mutation

The models discussed in previous subsection of this chapter are all win-lose symmetric, which means that the loss and gain due to a particular choice of strategy is always the same, and the payoff matrix of the RPS game is zero-sum. In this subsection, we will introduce an asymmetry into the RPS model, such that losses are always greater than gains. This extension of the model was analysed by Mobilia [51]. The model is summarised by the payoff matrix in the mean-field:

	A	B	C
A	0	1	$-1-\beta$
B	$-1-\beta$	0	1
C	1	$-1-\beta$	0

$$P := \begin{pmatrix} 0 & -1-\beta & 1 \\ 1 & 0 & -1-\beta \\ -1-\beta & 1 & 0 \end{pmatrix} \tag{2.15}$$

where $\beta \geq 0$ is a parameter that indicates that the loss incurred in losing contests is greater than the payoff gained from winning them. When $\beta = 0$, the row and column sums of P are zero: this is the simplest case and corresponds to that discussed in 1.3.1. When $\beta > 0$, the game becomes more complicated, particularly since we would like, as before, to relate the behaviour at the population level to the individual level, in the form of chemical reactions, as we discuss later.

Deterministic rate equations

Following the method in the section 1.3.1, the replicator equations (ordinary differential equations) (1.1)

$$\dot{x}_i = x_i \left(f_i - \phi \right), \quad i = 1, ..., n.$$

describe the dynamics at the mean-field population level:

$$\begin{aligned}
\dot{x}_1 &= x_1[x_3 - (1+\beta)x_2 + \beta(x_1x_2 + x_2x_3 + x_1x_3)] + \mu(x_2 + x_3 - 2x_1),\\
\dot{x}_2 &= x_2[x_1 - (1+\beta)x_3 + \beta(x_1x_2 + x_2x_3 + x_1x_3)] + \mu(x_1 + x_3 - 2x_2),\\
\dot{x}_3 &= x_3[x_2 - (1+\beta)x_1 + \beta(x_1x_2 + x_2x_3 + x_1x_3)] + \mu(x_1 + x_2 - 2x_3),
\end{aligned} \tag{2.16}$$

where again we include mutation. In contrast to equations (2.2)

$$\begin{aligned}
\dot{x}_1 &= x_1(x_3 - x_2) + \mu(x_2 + x_3 - 2x_1),\\
\dot{x}_2 &= x_2(x_1 - x_3) + \mu(x_1 + x_3 - 2x_2),\\
\dot{x}_3 &= x_3(x_2 - x_1) + \mu(x_1 + x_2 - 2x_3).
\end{aligned}$$

the new chaotic terms in (2.16) are introduced by the effect of the win-lose asymmetry parameter, β.

These equations are to be solved in the region of $\mathbb{R}^3$ where all coordinates are non-negative. This region is clearly invariant under the vector field (2.16). Moreover, the constraint $x_1 + x_2 + x_3 = 1$ is required to hold at all times.

As before, we can now proceed to carry out standard investigations of the dynamics of (2.16). We observe that there is only one interior equilibrium point, $x^* = (1/3, 1/3, 1/3)$. To investigate stability of this equilibrium point we write $x_3 = 1 - x_1 - x_2$, substitute this into (2.16) and then look at the resulting 2-dimensional system for (x_1, x_2). The Jacobian matrix at x^* can be easily calculated to be

$$J^* = \begin{pmatrix} -\frac{1}{3} - 3\mu & -\frac{2}{3} - \frac{1}{3}\beta \\ \frac{2}{3} + \frac{1}{3}\beta & \frac{1}{3} + \frac{1}{3}\beta - 3\mu \end{pmatrix}.$$

The eigenvalues of J^* are $\lambda_\pm = \lambda \pm \mathrm{i}\omega$, with $\lambda = \frac{\beta}{6} - 3\mu$ and $\omega = \frac{1}{2\sqrt{3}}\beta + \frac{1}{\sqrt{3}}$. If $\lambda < 0$, then the equilibrium point is linearly stable and there are no periodic orbits. In the case $\lambda > 0$, the equilibrium point x^* is unstable; in terms of the parameters the critical value of μ is $\mu_c = \frac{\beta}{18}$, and x^* is unstable when $\mu < \frac{\beta}{18}$ which is the parameter regime we will focus on.

Previous work by Mobilia [51] has shown that the system undergoes a supercritical Hopf bifurcation as μ decreases and that for $\mu < \mu_c$ trajectories of (2.16) spiral out away from x^* and are attracted to a unique periodic orbit which is stable, i.e a limit cycle. This behaviour is illustrated in fig 2-5.

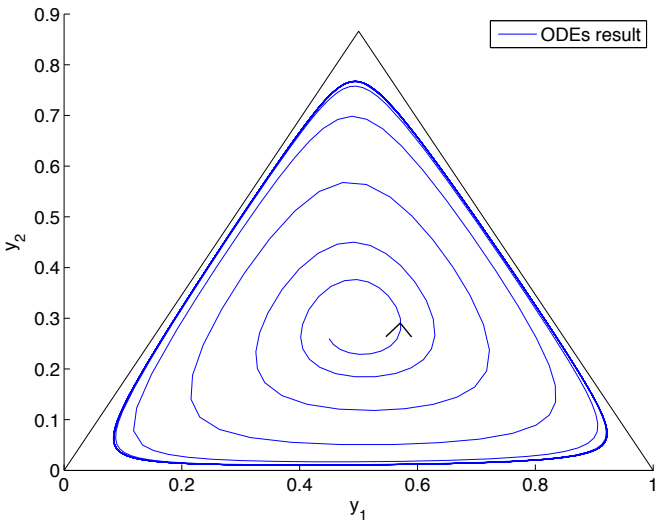

Figure(图) 2-5: A typical trajectory of the ODEs (2.16) in the (y_1, y_2) plane, showing spiralling outwards from the equilibrium point x^* and convergence to the limit cycle. Parameter values: $\beta = 0.5$, $\mu = \frac{1}{216} < \mu_c = \frac{1}{36}$. Horizontal direction $y_1 = x_1 + x_2/2$ and vertical direction $y_2 = \sqrt{3}x_2/2$.

Stochastic chemical reactions

We have discussed a deterministic, population-level model for the RPS game, based on the replicator equations. In a finite population, the behaviour of many competing individuals is more appropriately modelled using a set of stochastic transitions between these states of individuals: essentially a scheme of chemical reactions. In the limit of an infinitely large population, one would expect to recover the dynamics of the deterministic ODEs (2.16) describing the system behaviour. It is common practice to specify such a stochastic model as a chemical reaction scheme, which, chosen appropriately, should recover the ODEs (2.16) in the limit of large systems. It is interesting to note that different stochastic individual-based models may give rise to the same mean-field ODEs, so that the question of constructing a stochastic reaction scheme starting from a particular set of ODEs may not have a unique answer. We will discuss this point in more detail in the concluding chapter. This is different to the process of establishing ODEs from chemical reactions in section 1.3.2 and 1.3.3 for which a given system of chemical reactions always produces a unique set of mean-field ODEs. Moreover, the construction of the stochastic model is subject to a number of natural constraints, for example that all reaction rates are at all times non-negative.

For the "replicator" part of the dynamics in (2.16) we propose the chemical reactions

$$A + B \xrightarrow{1} B + B, \quad B + C \xrightarrow{1} C + C, \quad C + A \xrightarrow{1} A + A, \tag{2.17}$$

$$A + B + B \xrightarrow{\beta} B + B + B, \tag{2.18}$$

$$A + A + C \xrightarrow{\beta} A + A + A, \tag{2.19}$$

$$B + C + C \xrightarrow{\beta} C + C + C, \tag{2.20}$$

As before, mutations are included in the model through the additional six reactions

$$\begin{aligned} A \xrightarrow{\mu} B, \quad B \xrightarrow{\mu} C, \quad C \xrightarrow{\mu} A, \\ A \xrightarrow{\mu} C, \quad B \xrightarrow{\mu} A, \quad C \xrightarrow{\mu} B. \end{aligned} \tag{2.21}$$

This information can be more usefully summarised in terms of a stoichiometric matrix $\boldsymbol{S}$, describing the changes to $\boldsymbol{x}$ caused by the various reactions (so element S_{ij} represents the increment or decrement of species i taking place in reaction j), and vector $\boldsymbol{r}(\boldsymbol{x})$ describing the reaction rates. For the reactions in (2.17) –(2.20) we have

$$\boldsymbol{S}_1 = \begin{pmatrix} -1 & 0 & 1 & -1 & 1 & 0 \\ 1 & -1 & 0 & 1 & 0 & -1 \\ 0 & 1 & -1 & 0 & -1 & 1 \end{pmatrix}, \tag{2.22}$$

and the reaction rate vector

$$\boldsymbol{r}_1 = (x_1 x_2, x_2 x_3, x_3 x_1, \beta x_1 x_2^2, \beta x_1^2 x_3, \beta x_2 x_3^2)^T. \tag{2.23}$$

Similarly the mutation reactions in (2.21) are specified by the jump matrix

$$\boldsymbol{S}_2 = \begin{pmatrix} -1 & 0 & 1 & -1 & 1 & 0 \\ 1 & -1 & 0 & 0 & -1 & 1 \\ 0 & 1 & -1 & 1 & 0 & -1 \end{pmatrix}, \tag{2.24}$$

and the reaction rate vector

$$\boldsymbol{r}_2 = \mu(x_1, x_2, x_3, x_1, x_2, x_3)^T. \tag{2.25}$$

The jump matrix and rate vector for the full scheme are found simply by concatenation:

$$\boldsymbol{S} = [\boldsymbol{S}_1, \boldsymbol{S}_2]\,, \quad \boldsymbol{r} = \begin{bmatrix} \boldsymbol{r}_1 \\ \boldsymbol{r}_2 \end{bmatrix}. \tag{2.26}$$

So that $\boldsymbol{S}$ is a 3×12 element matrix, and $\boldsymbol{r}$ is a 12×1 element vector.

We choose to express our reactions in this form in order to appeal to a very useful theorem of Kurtz [37] (introduced in section 1.3.3), which states that in the limit $N \to \infty$ of large populations, the stochastic process described by these reactions converges to the deterministic dynamical system

$$\dot{\boldsymbol{x}} = \boldsymbol{S}\boldsymbol{r}(\boldsymbol{x})\,,$$

where $\boldsymbol{x} = (x_1, x_2, x_3)$. It is easy to check that the above scheme thus reproduces the system (2.16). Although we will develop our analysis for this particular chemical reaction scheme, it is important to reiterate that it may not be unique in reproducing the replicator equations in the large population limit. For example, in paper [51] the author set a reaction scheme with an average payoff rate (e.g. $A+B \xrightarrow{1+f_1-\phi} B+B$ with $f_1 = \sum_{j=1}^{3} P_{1j}x_j$ and $\phi = \sum_{i=1}^{3}\sum_{j=1}^{3} x_i P_{ij} x_j$). The advantage of that model is that a reaction scheme consisting only of two-body interactions is a more natural system in the real world, so at the beginning of my research I tried to follow this method. However, when the mutation rate is very small, the average payoff rate might become negative. Consequently, we have chosen to adopt the current reaction scheme in order to carry out the stochastic simulations.

Simulations

To gain an initial insight into the differences between the deterministic and stochastic viewpoints for the win-lose asymmetric RPS game with mutation, we use the Gillespie algorithm 1.1 (introduced in the section 1.3.1) [21], to simulate the chemical reactions (2.17)-(2.21) in order to illustrate the typical dynamics in the stochastic case and to compare that with the deterministic case. The standard and widely used stochastic simulation algorithm is referred to as the 'SSA' in the legend of subsequent figures.

Figure 2-6 presents results comparing the stochastic and deterministic cases for two different values of the mutation rate μ. In each plot we show a typical realisation of the stochastic simulation algorithm, for two different finite, but large, population sizes $N = 2^8$ (green dashed line) and $N = 2^{16}$ (red dashed line), together with a trajectory of the ODEs (blue solid line).

The solution to the ODEs shown by the blue line in 2-6(a) is the same as that

shown in figure 2-5. The red dashed line in 2-6(a) starts from a very similar initial condition and evolves similarly: spiralling out towards the boundary of phase space and at large times occupying a region of phase space near to the limit cycle but with small fluctuations around it. The green dashed line in 2-6(a) shows much larger fluctuations around the limit cycle, including excursions that take the simulation onto the boundaries of the phase space, and much closer to the corners. Note that because of the mutations, the boundaries of the phase space are not absorbing states for the random process (or invariant lines for the ODE dynamics).

Figure 2-6(b) illustrates the behaviour for a significantly larger value of μ for which the limit cycle for the ODEs (blue curve) lies much closer to the centre of the phase space. The SSA for $N = 2^{16}$ lies close to the limit cycle but fluctuates around it; for $N = 2^8$ the fluctuations are much larger and the sample path of the stochastic process lies outside the limit cycle for a large proportion of the simulation time.

To quantify the differences between the three results shown in each part of figure 2-6, we focus on one specific aspect of the dynamics: **the period of the oscillations** around the central equilibrium point at $(1/3, 1/3, 1/3)$. For the ODEs, the period of the limit cycle can be defined to be the smallest elapsed time between successive crossings of a hyperplane in the same direction, for example the plane $x_1 = 1/2$ (this is a sensible choice because, as we will later show, the effect of noise is smallest at this part of the cycle). We denote by T_{ODE} the period of the deterministic limit cycle. In stochastic simulations, a trajectory may by chance cross a hyperplane back and forth several times in quick succession, thus the time between crossings may not represent a full transit of the cycle. We avoid this complication by measuring the period as three times the transit time between the first interaction with a given hyperplane and the first subsequent interaction with its $2\pi/3$ rotation in the barycentric coordinates. The expected value of this oscillation period in the stochastic case we denote by T_{SSA}.

Figure 2-7 provides a quantitative comparison of the different dependencies of the average period T_{SSA} of the stochastic simulations and the period T_{ODE} of the deterministic ODEs on the mutation rate μ, for $0 < \mu < \mu_c$. The blue solid line indicates the relatively slow increase in the period T_{ODE} as μ decreases. The red error bars indicate the range of values of the oscillation period in the stochastic case, with the averages of those values shown by the red dots. The data in this figure for the stochastic simulations was obtained from simulations for a total number of oscillation periods $T_{\mathrm{sim}} = 2000$ at a fixed value $N = 2^{17} = 131072$ with μ varying. When the simulation is running, we record the time that the state passes $x_1 = 0.5$, $x_2 = 0.5$ and x_3=0.5 in turns. The last 6000 $(3 \times T_{\mathrm{sim}})$ sets of recorded timings are chosen for illustrating the 'period' T_{SSA}. These data obey a distribution, so we use error-

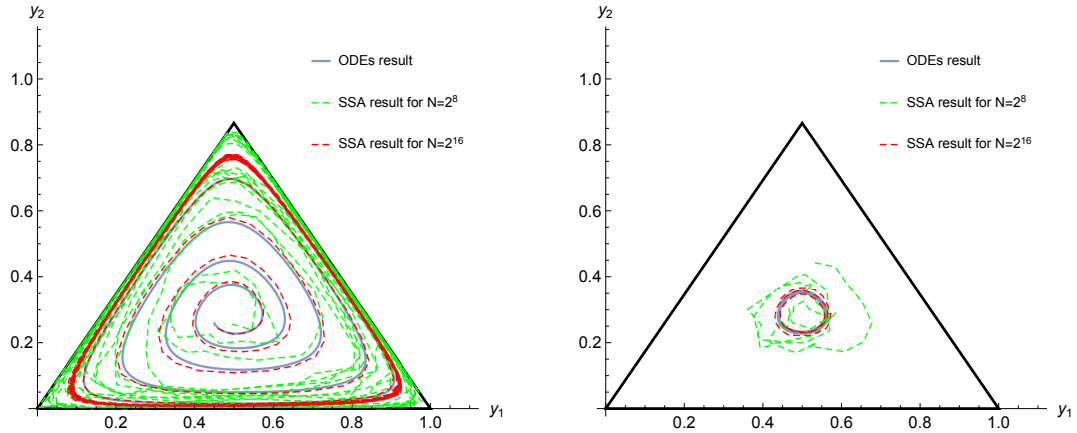

Figure(图) 2-6: Illustrative comparisons between trajectories of the ODEs (blue solid lines) and realisations of the stochastic simulations (red and green dashed lines). Horizontal direction $y_1 = x_1 + x_2/2$ and vertical direction $y_2 = \sqrt{3}x_2/2$. The time step in the simulation is 0.5 and the initial value is $(x_1, x_2, x_3) = (0.3, 0.3, 0.4)$. (a) When $\mu \ll \mu_c$ the trajectories lie close to the boundary of the phase space. Parameter values are $\beta = 1/2$, $\mu = 1/216$, $t \in [0, 300]$. (b) When μ is only slightly smaller than μ_c, trajectories lie much closer to the central equilibrium point. Parameter values are $\beta = 1/2$, $\mu = 5/198$, $t \in [0, 25]$.

bar to show the main statistical properties (raw mean and variance). However, for presentational reasons that will become clearer later in the chapter we have chosen to plot the scaled quantity $\mu N \ln N$ on the horizontal axis. We then observe that if μ is sufficiently small then the difference between T_{ODE} and T_{SSA} is very significant: the oscillations in the stochastic simulation have a much longer period, on average, than that predicted by the ODEs, while if $\mu N \ln N$ is larger than unity, the agreement in terms of the oscillation period, between the deterministic and stochastic simulations is very good. We label these two regimes 'Region III' and 'Region I' respectively. The cross-over region where $\mu N \ln N \approx 1$ we label 'Region II'.

To summarise, in this section, we introduced two extensions of the RPS model by considering (i) mutation and (ii) a win-lose asymmetric payoff matrix. For the symmetric model, with mutation, trajectories are always attracted to the central equilibrium point. Demographic noise drives stochastic oscillations around the equilibrium point. For the asymmetric model, there is a stable limit cycle when mutation rate is small, and the demographic noise slows down the oscillations.

The innovation of our work here includes: (1) scheme of translating the ODEs derived from asymmetric payoff matrix to chemical reactions; (2) identification of three

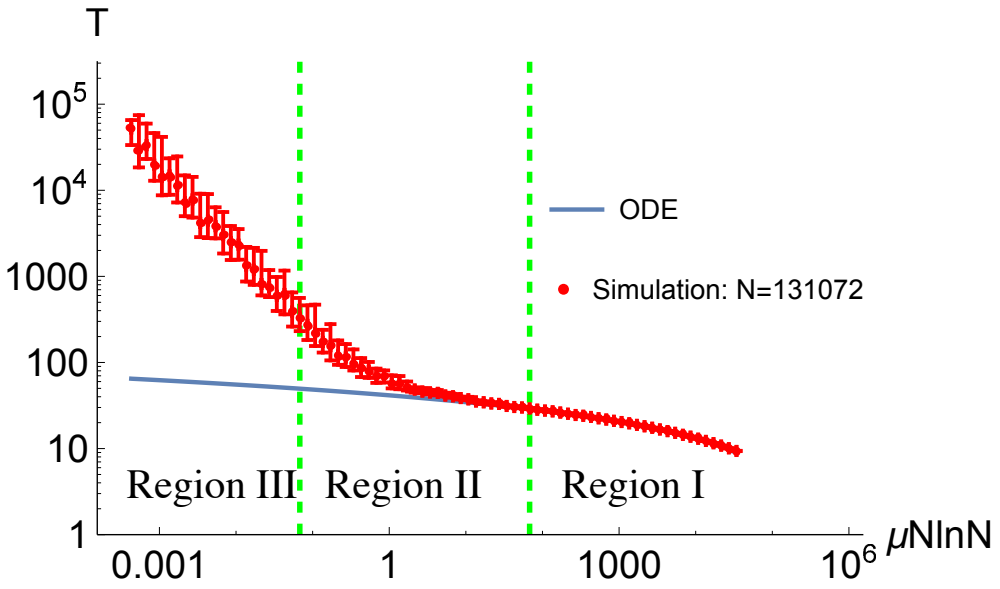

Figure(图) 2-7: Comparison between the period T_{ODE} of the limit cycle in the deterministic case and the average period T_{SSA} of oscillations in the stochastic case, as a function of the parameter μ at fixed $N = 2^{17}$. The blue line shows T_{ODE} and red dots indicate T_{SSA}. As μ decreases, the two periods start to separate from each other in Region II where $\mu N \log N \approx 1$.

regimes in the parameter space, distinguished by the value of $\mu N \log N$, in which the period of the stochastic oscillations are almost the same as in the ODEs, a little greater, or of totally different period, respectively.

In the next section, we will analyse these three regions in detail with different mathematical techniques, to understand how the noise affects the cycles.

2.2 Behaviour of the Limit Cycle in Regions I–III

We have previously proposed a division of the interval $(0, \mu_c)$ into three regions. In this section we will focus on each of the three regions. In the section 2.2.1 we study the period of the limit cycle in the ODEs (region I). In the section 2.2.2 we analyse the stochastic dynamics to determine the average period of cycles in region III. In the section 2.2.3 the cross-over between the deterministic and stochastic regions is understood through the analysis of an SDE that combines both deterministic and stochastic effects, thus describing region II.

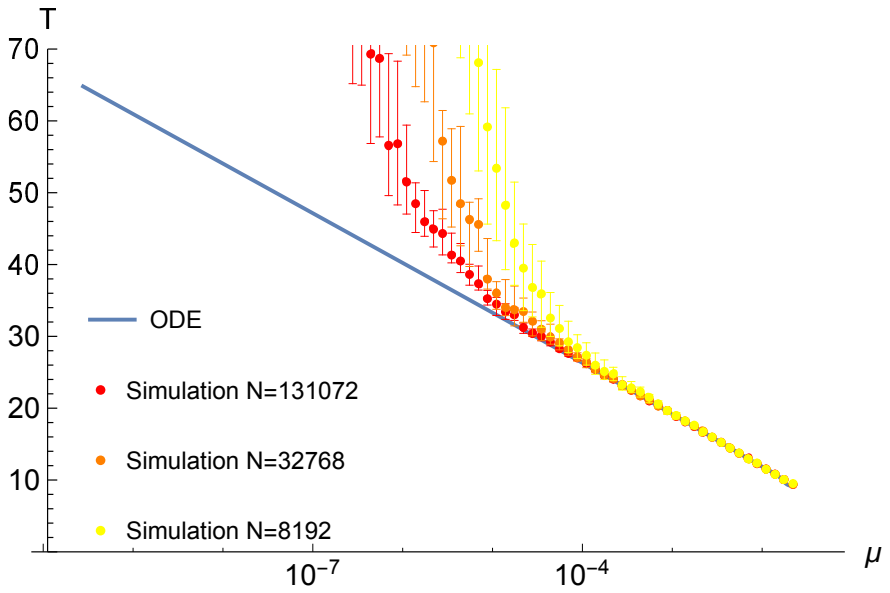

Figure(图) 2-8: Period T_{SSA} for three different values of N, compared with the result for T_{ODE} (blue solid line) on a log-linear plot indicating the scaling law $T_{\mathrm{ODE}} \propto -3\log\mu$ which applies in region I where the stochastic simulations behave in a similar way to the ODEs. The method used to record the 'period' of the stochastic simulations is the same as previously explained.

2.2.1 Analysis of the Periodic Orbit in Region I

Region I is defined to be the right hand side of figure 2-7; more precisely, it is the regime in which $N \gg 1$ and $(N\log N)^{-1} \ll \mu < \mu_c$. In this region, stochastic simulation results show only very small fluctuations about a mean value, and this mean value coincides well with numerical solutions to the ODEs. This is evidence that the behaviour of the deterministic ODEs provides a very good guide to the stochastic simulation results in this region. Hence our goal in this section is to explain the asymptotic result that the period, $T_{\mathrm{ODE}} \propto -3\log\mu$ for μ small, but for large, even infinite, N as shown in figure 2-8.

The standard approach to the analysis of trajectories near the limit cycle, in the regime where it lies close to the corners of the phase space, is to construct local maps that analyse the flow near the corners, and global maps that approximate the behaviour of trajectories close to the boundaries [24]. Figure 2-9 shows the construction of a local map in the neighbourhood of the corner where $x_3 = 1$, followed by the global map from this neighbourhood to a neighbourhood of the corner where $x_1 = 1$. In this section we consider local and global maps in turn and we then study their composition, and deduce an estimate for the period T_{ODE} of the limit cycle.

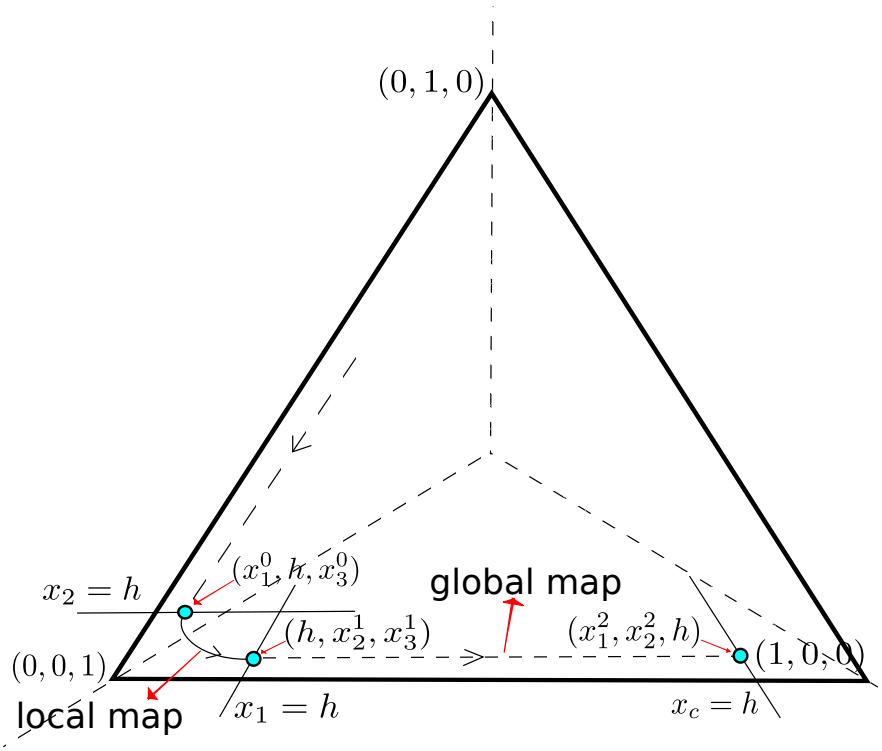

Figure(图) 2-9: This picture shows the local map and the global map starting from initial position (x_1^0, h, x_3^0), which shown in the picture is (x_a^0, h, x_c^0). Here all the subscripts $\{a, b, c\}$ can be replaced by $\{1, 2, 3\}$ respectively.

Local map

Using the notation as in figure 2-9, we begin by defining a neighbourhood of the corner $x_3 = 1$ by setting $0 < h \ll 1$ to be a small positive constant. We assume that the trajectory for the ODEs (2.16) starts at the point (x_1^0, h, x_3^0) at time $t = 0$, and arrives at the point (h, x_2^1, x_3^1) at time $t = T_1 > 0$. For the whole time $0 < t < T_1$ the trajectory lies close to the corner $(0, 0, 1)$, so we suppose that $0 < x_1, x_2, u \ll 1$ where $u := 1 - x_3$. Note that we have $x_1 + x_2 - u = 0$ since $x_1 + x_2 + x_3 = 1$.

Then the behaviour of the ODEs (2.16) in this neighbourhood is very similar to that of their linearisation obtained by dropping terms higher than linear order in the small quantitites $0 < x_1, x_2, u \ll 1$. For the linearised system we obtain

$$\begin{cases} \dot{x}_1 = \mu - x_1(3\mu - 1), \\ \dot{x}_2 = \mu - x_2(1 + \beta + 3\mu), \\ \dot{u} = -x_2(1 + \beta) + x_1 + 2\mu - 3\mu u. \end{cases} \tag{2.27}$$

The equations (2.27) are linear and constant coefficient and so can be solved analytically; note that the first and second equation are actually decoupled from each other and from the u equation. Integrating from $t = 0$ to the time $t = T_1$, we denote the point on the trajectory by $(x_1(T_1), x_2(T_1), x_3(T_1)) \equiv (x_1^1 = h, x_2^1, x_3^1)$ where

$$x_2^1 = \frac{\mu}{\gamma}\left(1 - \mathrm{e}^{-\gamma T_1}\right) + h\mathrm{e}^{-\gamma T_1}, \tag{2.28}$$

$$x_1^1 = h = \frac{\mu}{\hat{\gamma}} + \mathrm{e}^{-\hat{\gamma} T_1}\left(x_1^0 - \frac{\mu}{\hat{\gamma}}\right), \tag{2.29}$$

where $\gamma := 1 + \beta + 3\mu$ and $\hat{\gamma} := 3\mu - 1$. Equation (2.29) allows us to express T_1 in terms of x_1^0:

$$T_1 = -\frac{1}{\hat{\gamma}} \log\left(\frac{h - \mu/\hat{\gamma}}{x_1^0 - \mu/\hat{\gamma}}\right), \tag{2.30}$$

and we can now use (2.30) to eliminate T_1 from (2.28) and obtain a relationship between x_1^0 and x_2^1 which takes the form

$$x_2^1 = \frac{\mu}{\gamma} + \left(h - \frac{\mu}{\gamma}\right)\left(\frac{h - \mu/\hat{\gamma}}{x_1^0 - \mu/\hat{\gamma}}\right)^{\gamma/\hat{\gamma}}. \tag{2.31}$$

This relationship is the key part of the local map near the point $(x_1, x_2, x_3) = (0, 0, 1)$ that we will use in what follows.

Global Map

For the global map, we observe that trajectories remain close to one of the boundaries (in this case, the boundary $x_2 = 0$) and so we propose that the trajectory starting from $(x_1^1 = h, x_2^1, x_3^1)$ arrives at the point (x_1^2, x_2^2, h) at time $t = T_2$. Referring to (2.16), the ODE for x_2 near the boundary can be well approximated by taking just $\dot{x}_2 = \mu$ (since $x_1 + x_3 = 1$ when $x_2 = 0$), so its solution is

$$x_2^2 = x_2^1 + (T_2 - T_1)\mu = x_2^1 + \mathcal{C}_0\mu, \tag{2.32}$$

where we denote the elapsed time by $\mathcal{C}_0 := T_2 - T1$. As is typical in these analyses, trajectories take a relatively short time to arrive at the hyperplane $x_3^2 = h$ starting from x_3^1, compared to the time taken to move along the part of the trajectory from x_3^0 to x_3^1; this is intuitively because the absolute value of $\dot{x}_3$ on the global part of the map between T_1 and T_2 is much larger than on the local part, i.e. when $0 < t < T_1$. As a result, the time taken on the global part of the map, $\mathcal{C}_0 := T_2 - T_1$ is much less than the local travel time T_1; the majority of the time spent on the limit cycle is taken up with travel near the corners.

Composition of maps

The composition of local and global maps near the corner $x_3 = 1$ and boundary $x_2 = 0$ is now straightforward: we combine (2.31) and (2.32) to obtain:

$$x_2^2 = \mathcal{C}_0\mu + \frac{\mu}{\gamma} + \left(h - \frac{\mu}{\gamma}\right)\left(\frac{h - \mu/\hat{\gamma}}{x_1^0 - \mu/\hat{\gamma}}\right)^{\gamma/\hat{\gamma}}. \tag{2.33}$$

We can now use the permutation symmetry inherent in the dynamics to complete the analysis. Due to the fact that the model is rotationally symmetric, the next stage of the evolution is a local map again with the same parameter values. The trajectory will start from (x_1^2, x_2^2, h) and stay near the corner $(1, 0, 0)$ for long time before arriving at a point, say, (x_1^3, h, x_3^3) where we will construct another global map, and so on:

$$x_1^0 \xrightarrow{local} x_2^1 \xrightarrow{global} x_2^2 \xrightarrow{local} x_3^3 \xrightarrow{global} x_3^4 \xrightarrow{local} x_1^5 \xrightarrow{global} x_1^6 \to \cdots \tag{2.34}$$

which can be summarised further as

$$y_0 \xrightarrow{local\ \&\ global} y_1 \xrightarrow{local\ \&\ global} y_2 \xrightarrow{local\ \&\ global} y_3 \to \cdots \tag{2.35}$$

Equations (2.34) and (2.35) above define a one-to-one correspondence between the points $\{(x_1^n, x_2^n, x_3^n)\}$ on a trajectory and a sequence of values (selecting appropriate coordinates) $\{y_n\}$. From the previous discussion on local and global maps, the map that generates the sequence $\{y_n\}$ takes the form

$$y_{n+1} = \mathcal{C}_0\mu + \frac{\mu}{\gamma} + \left(h - \frac{\mu}{\gamma}\right)\left(\frac{h - \mu/\hat{\gamma}}{y_n - \mu/\hat{\gamma}}\right)^{\gamma/\hat{\gamma}}, \tag{2.36}$$

where, as before, $\gamma := 1 + \beta + 3\mu$ and $\hat{\gamma} := 3\mu - 1$.

If iterates of the map (2.36) converge to a fixed point then this corresponds to a stable limit cycle for the ODE dynamics. We now estimate the location of this fixed point and deduce an estimate for the period of the resulting limit cycle.

Let $z_n := y_n/\mu$ be a scaled version of y_n, then (2.36) can be written as:

$$\begin{aligned} z_{n+1} &= \mathcal{C}_0 + \frac{1}{\gamma} + \left(h - \frac{\mu}{\gamma}\right)\frac{1}{\mu}\left(\frac{\mu z_n + \frac{\mu}{1-3\mu}}{h + \frac{\mu}{1-3\mu}}\right)^{\frac{1+3\mu+\beta}{1-3\mu}} \\ &= \mathcal{C}_0 + \frac{1}{\gamma} + \left(h - \frac{\mu}{\gamma}\right)\mu^{\frac{1+3\mu+\beta}{1-3\mu}-1}\left(\frac{z_n(1-3\mu)+1}{h(1-3\mu)+\mu}\right)^{\frac{1+3\mu+\beta}{1-3\mu}}, \end{aligned} \tag{2.37}$$

where $\gamma := 1+\beta+3\mu$. Denoting the fixed point of the map by z^*, from (2.37) we see that $z^* = \mathcal{C}_0 + 1/\gamma + o(\mu)$ in the limit $\mu \to 0$. This observation is crucial in order to ensure

that we obtain the correct leading-order behaviour and distinguish carefully between the various small quantities in the problem. Then it follows that $y^* = \mu z^* \approx \mathcal{C}_1 \mu$, where $\mathcal{C}_1 = \mathcal{C}_0 + 1/(1+\beta)$, in the limit $\mu \to 0$.

Introducing this leading-order approximation for y^* into (2.30), we obtain an estimate of the time spent in a neighbourhood of the corner T_1 of the stable limit cycle:

$$T_1 = \frac{1}{1-3\mu} \log\left(\frac{h + \mu(1-3\mu)}{\mathcal{C}_1\mu + \mu(1-3\mu)}\right). \tag{2.38}$$

Since in this case μ is assumed to be very small, (2.38) takes the form, at leading order,

$$T_1 = \frac{1}{1-3\mu} \log\left(\frac{1}{\mu}\right) + \mathcal{B}_0 \text{ as } \mu \to 0. \tag{2.39}$$

where $\mathcal{B}_0$ is a constant.

Finally, as remarked on above, because trajectories remain near each corner for large parts of the period of the orbit, the local map travel time T_1 is the dominant contribution, compared to the time spent on the global map. Hence the period of the limit cycle is given at leading order by considering only the contribution from the three local maps required in one full period of the limit cycle. Hence our estimate for T_{ODE} becomes

$$T_{\text{ODE}} \approx 3T_1 = -3\log\mu + \mathcal{B}_1, \tag{2.40}$$

as $\mu \to 0$. In Region I, $\mu < \mu_c = 1/36$ is small enough to make equation (2.40) valid. Therefore it gives a good approximation of the period in Region I.

2.2.2 Analysis of the Periodic Orbit in Region III

We now turn our attention to Region III, where the period of the orbit in the stochastic simulations increases much more rapidly as μ decreases, at fixed finite N, than the prediction from the analysis of the ODEs in section 2.2.1 above suggests. Figure 2-10 illustrates this by plotting the period T_{SSA} as a function of $\mu N \ln N$ for three different values of N. By plotting, on a log-log scale, the mean values of the periods and the error bars from an ensemble of stochastic simulations we observe that the period $T_{\text{SSA}} \approx (\mu N \ln N)^{-1}$ for small μ, with a constant that does not demonstrate any systematic dependence on N. In fact, the range of values of N presented here is small: we cannot distinguish from these numerical results the precise form of the dependence on N.

As well as the dependence of the period T_{SSA} on μ it is also of interest to determine the extent of Region III in which this scaling behaviour applies; in other words how small is μ required to be in order to move into this regime? The numerical data in

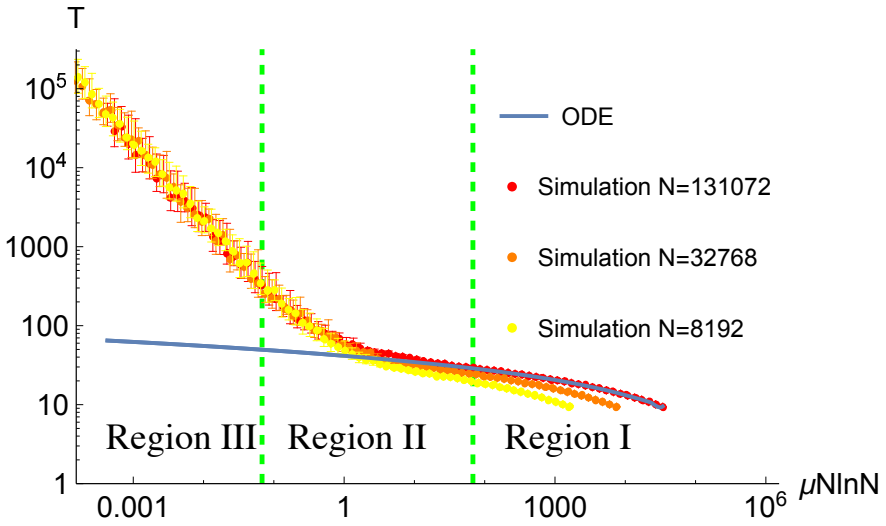

Figure(图) 2-10: Log-log plot of the period T_{SSA} as a function of the mutation rate μ for three different values of N, showing that in region III the mean period scales roughly as $T_{\mathrm{SSA}} \approx (\mu N \ln N)^{-1}$.

figure 2-10 indicate that the cross-over from the ODE result to this new stochastic scaling arises when $\mu N \log N \approx 1$.

In this section, then, our aim is to explain firstly why this new scaling regime in Region III exists, and secondly, why it extends as far as $\mu N \ln N = 1$. We will find that in fact the period should scale as $T_{\mathrm{SSA}} \approx (\mu N)^{-1}$ for small μ (due to time spent waiting for rare mutations), but that the observation that the cross-over occurs when $\mu N \ln N \approx 1$ is correct; this explains why we have chosen to plot figure 2-10 in the form that it appears.

Careful examination of the numerical simulations in this regime show that their behaviour is qualitatively different from that in Region I discussed above. In stochastic simulations the system becomes strongly attracted to the corner states (which would be absorbing states in the absence of mutation) and then can only escape from a corner in the correct direction when a mutation occurs; mutations are rare when μ is small. Our analysis later in this section shows that the mean period of oscillation is dominated by the contribution from the time needed to escape one step from a corner. If the system takes a step directly towards the next corner in the sequence, then it will leave the neighbourhood of the corner quickly and continue moving towards the next corner; if the system takes a step in a different direction then the system will remain near the corner until it moves off in the correct direction. Trajectories then typically move along a boundary towards the next corner. We show below that, although this latter part

requires at least $N-1$ steps, the expected total time required is less than the waiting time to escape from the corner. Our schematic approach is illustrated in figure 2-11, in which the separation of these two parts to the dynamics is sktched: a first step away from a corner, followed by movement along the adjoining boundary.

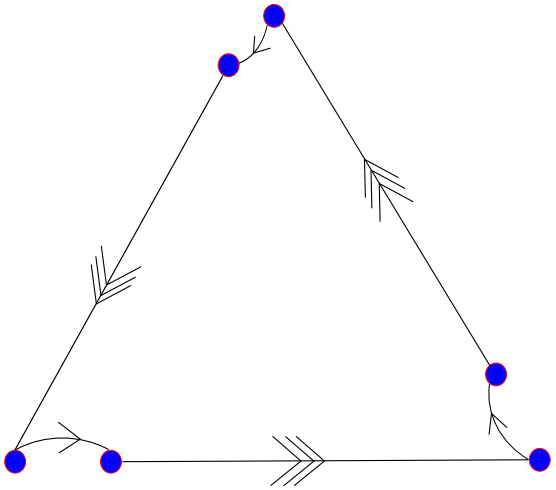

Figure(图) 2-11: Sketch of the dynamics in the small-μ stochastic limit. The system is strongly attracted to corner states where the population is all in one state. Mutation is then the only mechanism for escape, and the expected time for the first mutation (curved arrows) is longer than the expected time required for subsequent steps along a boundary towards the next corner (straight lines with arrows).

In the following subsections we consider in detail three issues: firstly, in the part **'Probability of hitting the absorbing state'** we show that the probability that the motion along a boundary is towards the next corner in the sequence, and that the system state hits this next corner tends to 1 as $N \to \infty$. Since we are interested in the regime in which the mutation rate is very small, we carry out this calculation in the limit $\mu = 0$. In the part **'Average hitting time'** we compute the expected time until the system hits this next corner, again setting $\mu = 0$. Finally, in the part **'The effect of mutation on the stochastic dynamics'** we compare this expected time for the system state to evolve along the boundary with the expected time until a mutation occurs. Together, this analysis confirms the intuitive picture outlined in the previous paragraph.

Probability of hitting the absorbing state

Here we consider the discrete–state and continuous–time Markov Chain dynamics of the system evolving along a boundary, ignoring the effect of mutation. In this case

the system is a one dimensional chain of $N+1$ states with transition probabilities p_i and q_i defined diagrammatically as follows:

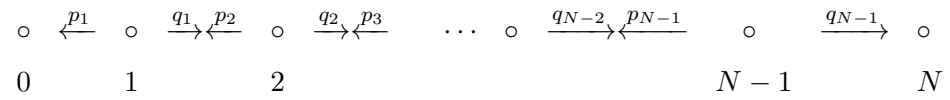

The $N+1$ states are labelled 0 to N, corresponding to, for example, the number of strategy B individuals invading a population of size N initially composed of all strategy A individuals. Let $h_i = \mathbb{P}_i(\text{hit } 0)$ be the probability that the system hits (and is therefore absorbed by) state 0 having started at node i, and similarly let $\bar{h}_i = \mathbb{P}_i(\text{hit } N)$ be the probability of hitting state N having started at node i.

When the system is in state i there are two possible moves: jumps to the left or to the right. The rate at which jumps to the left occur is $p_i = (N-i)i^2/N^2$; the rate at which jumps to the right occur is $q_i = (N-i)i^2(1+\beta)/N^2 + (N-i)i/N$. The transition probabilities of moving to the left and to the right are then $\ell_i = p_i/(p_i+q_i)$ and $r_i = q_i/(p_i+q_i)$; clearly $\ell_i + r_i = 1$. We remark that the ratio of transition probabilities can be simplified to be

$$\begin{aligned} \frac{\ell_i}{r_i} = \frac{p_i}{q_i} &= \frac{(N-i)i^2/N^2}{(N-i)i^2(1+\beta)/N^2 + (N-i)i/N} \\ &= \frac{i}{i(1+\beta)+N} = \frac{1}{(1+\beta)+\frac{N}{i}}. \end{aligned} \tag{2.41}$$

This allows us to derive a recurrence relation for the probability h_i that the system hits the state 0 starting from state i:

$$\begin{cases} h_0 = 1, \\ h_i = \ell_i h_{i-1} + r_i h_{i+1}, \quad \text{for } i = 1 \dots N-1, \\ h_N = 0. \end{cases} \tag{2.42}$$

Recurrence relations of this type are straightforward to solve by standard methods [60]. From the recurrence formulas (2.42), and using $r_i + \ell_i = 1$ we have the relation

$r_i(h_i - h_{i+1}) = \ell_i(h_{i-1} - h_i)$ which implies that

$$\begin{aligned} h_i - h_{i+1} &= \frac{\ell_i}{r_i}(h_{i-1} - h_i) \\ &= \frac{\ell_i \ell_{i-1}}{r_i r_{i-1}}(h_{i-2} - h_{i-1}) \\ &= \cdots \\ &= \frac{\ell_i \ell_{i-1} \ldots \ell_1}{r_i r_{i-1} \ldots r_1}(h_0 - h_1) =: \gamma_i(h_0 - h_1), \end{aligned}$$

defining the ratio γ_i for $1 \leq i \leq N-1$, where we also define $\gamma_0 = 1$, so that we can write the recurrence relation between the h_i as

$$h_i - h_{i+1} = \gamma_i(h_0 - h_1). \tag{2.43}$$

We note that the following inequality, bounding γ_i, will be very useful:

$$\gamma_i := \prod_{j=1}^{i} \frac{\ell_j}{r_j} = \prod_{j=1}^{i} \frac{j}{j(1+\beta) + N} < \frac{i!}{N^i} \tag{2.44}$$

Summing (2.43) from $i = 0$ to $i = N-1$ enables us now to compute h_1 in terms of h_0 and h_N:

$$\begin{aligned} h_0 - h_N &= \sum_{i=0}^{N-1} (h_i - h_{i+1}) \\ &= (1 + \gamma_1 + \gamma_2 + \cdots + \gamma_{N-1})(h_0 - h_1). \end{aligned} \tag{2.45}$$

Finally, h_1 can be calculated directly since $h_0 = 1$ and $h_N = 0$:

$$h_1 = \frac{\sum_{i=1}^{N-1} \gamma_i}{1 + \sum_{i=1}^{N-1} \gamma_i}, \tag{2.46}$$

and of course $\bar{h}_1 = 1 - h_1 = \left(1 + \sum_{i=1}^{N-1} \gamma_i\right)^{-1}$.

We now examine the limiting behaviour of this result and prove that $h_1 \to 1$ as $N \to \infty$. Since

$$0 < \gamma_{i+1} = \frac{p_{i+1}}{q_{i+1}} \gamma_i,$$

and $p_{i+1}/q_{i+1} < 1$, it follows that $\gamma_{i+1} < \gamma_i$. Also, since $\gamma_i < i!/N^i$, we conclude that

$$0 < \sum_{i=1}^{N-1} \gamma_i = \gamma_1 + \sum_{i=2}^{N-1} \gamma_i \leq \gamma_1 + \sum_{i=2}^{N-1} \gamma_2 \leq \frac{1}{N} + (N-2)\frac{2}{N^2},$$

which clearly tends to zero as $N \to \infty$. Hence

$$\lim_{N\to\infty} \sum_{i=1}^{N-1} \gamma_i = 0. \tag{2.47}$$

In conclusion, we have shown that, given that it starts at state 1, the probability of the system hitting the absorbing state at N tends to 1 as $N \to \infty$.

Average hitting time

Having shown that the system reaches state N with high probability, we now consider the expected time until this happens. Let T_i be the first time at which the system hits an absorbing state starting from state i at time 0, i.e. the time at which the system hits either 0 or N. Define $\tau_i = \mathbb{E}(T_i)$ for $0 \leq i \leq N$, the expected hitting time starting from state i. Clearly we have that $\tau_0 = \mathbb{E}(T_0) = 0$ and $\tau_N = \mathbb{E}(T_N) = 0$. Through a similar calculation to the part **'Probability of hitting the absorbing status'** [60], we now compute τ_1, the mean time taken to reach either 0 or N, starting from state 1.

The recurrence formula for expected hitting times τ_i can be computed as the sum of the expected time spent in state i before jumping either left or right, plus the expected future time required when in that new state:

$$\tau_i = \frac{1}{p_i + q_i} + \ell_i \tau_{i-1} + r_i \tau_{i+1}, \qquad \text{for } i = 1 \ldots N-1. \tag{2.48}$$

This recurrence relation can be rearranged to give

$$\begin{aligned} (p_i + q_i)\tau_i &= p_i\tau_{i-1} + q_i\tau_{i+1} + 1 \\ \implies q_i(\tau_i - \tau_{i+1}) &= p_i(\tau_{i-1} - \tau_i) + 1 \\ \implies \tau_i - \tau_{i+1} &= \frac{p_i}{q_i}(\tau_{i-1} - \tau_i) + \frac{1}{q_i} \end{aligned} \tag{2.49}$$

Repeated substitution of the term $\tau_{i-1} - \tau_i$ in (2.49) gives

$$\begin{aligned}
\tau_i - \tau_{i+1} &= \frac{p_i}{q_i}\left(\frac{p_{i-1}}{q_{i-1}}(\tau_{i-2} - \tau_{i-1}) + \frac{1}{q_{i-1}}\right) + \frac{1}{q_i} \\
&= \frac{p_i p_{i-1}}{q_i q_{i-1}}(\tau_{i-2} - \tau_{i-1}) + \frac{p_i}{q_i}\frac{1}{q_{i-1}} + \frac{1}{q_i} \\
&= \cdots \\
&= \frac{p_i p_{i-1}\cdots p_2 p_1}{q_i q_{i-1}\cdots q_2 q_1}(\tau_0 - \tau_1) + \frac{p_i p_{i-1}\cdots p_3 p_2}{q_i q_{i-1}\cdots q_3 q_2}\frac{1}{q_1} \\
&\quad + \frac{p_i p_{i-1}\cdots p_4 p_3}{q_i q_{i-1}\cdots q_4 q_3}\frac{1}{q_2} + \cdots + \frac{p_i}{q_i}\frac{1}{q_{i-1}} + \frac{1}{q_i}.
\end{aligned} \tag{2.50}$$

To simplify notation, note that (2.50) can also written in the form:

$$\tau_i - \tau_{i+1} = \gamma_i(\tau_0 - \tau_1) + \sum_{j=1}^{i} \frac{\gamma_i}{\gamma_j}\frac{1}{q_j}\,.$$

In order manipulate this, we write out the first and last terms explicitly, for clarity:

$$\begin{cases}
\tau_0 - \tau_1 &= \tau_0 - \tau_1\,, \\
\tau_1 - \tau_2 &= \gamma_1(\tau_0 - \tau_1) + \frac{1}{q_1}\,, \\
&\vdots \\
\tau_{N-2} - \tau_{N-1} &= \gamma_{N-2}(\tau_0 - \tau_1) + \frac{\gamma_{N-2}}{\gamma_1}\frac{1}{q_1} + \frac{\gamma_{N-2}}{\gamma_2}\frac{1}{q_2} + \cdots + \frac{\gamma_{N-2}}{\gamma_{N-3}}\frac{1}{q_{N-3}} + \frac{1}{q_{N-2}}\,, \\
\tau_{N-1} - \tau_N &= \gamma_{N-1}(\tau_0 - \tau_1) + \frac{\gamma_{N-1}}{\gamma_1}\frac{1}{q_1} + \frac{\gamma_{N-1}}{\gamma_2}\frac{1}{q_2} + \cdots + \frac{\gamma_{N-1}}{\gamma_{N-2}}\frac{1}{q_{N-2}} + \frac{1}{q_{N-1}}\,.
\end{cases} \tag{2.51}$$

Summing the equations in (2.51), and rewriting the summation of the terms on the right hand side, we now write this as

$$\tau_0 - \tau_N = \left(1 + \sum_{i=1}^{N-1}\gamma_i\right)(\tau_0 - \tau_1) + \sum_{i=1}^{N-1}\left(\frac{1}{q_i\gamma_i}\sum_{j=i}^{N-1}\gamma_j\right) \tag{2.52}$$

Since $\tau_0 = \tau_N = 0$ we can solve this to obtain τ_1 directly:

$$\tau_1 = \left(1 + \sum_{i=1}^{N-1}\gamma_i\right)^{-1}\sum_{i=1}^{N-1}\left(\frac{1}{q_i}\sum_{j=i}^{N-1}\frac{\gamma_j}{\gamma_i}\right). \tag{2.53}$$

We now wish to examine the asymptotic behaviour of this expression for the expected hitting time, in the limit when $N \gg 1$. Initial numerical explorations lead us to propose that $\tau_1 \propto \ln N$ when N is sufficiently large. In the remainder of this section we will deduce this estimate systematically.

First, note that from (2.47) we know that

$$\lim_{N\to\infty}\left(1+\sum_{i=1}^{N-1}\gamma_i\right)=1. \tag{2.54}$$

From the discussion before (2.41) we have that

$$\begin{aligned} q_i &= i(N-i)\frac{1}{N}\left[\frac{i}{N}(1+\beta)+1\right] \\ \Rightarrow \frac{1}{q_i} &= \frac{N}{i(N-i)}\frac{1}{1+(1+\beta)\frac{i}{N}}. \end{aligned} \tag{2.55}$$

Since

$$\frac{1}{2+\beta}<\frac{1}{1+(1+\beta)\frac{i}{N}}<1,$$

(as $1\le i\le N-1$), we can bound $\sum_{i=1}^{N-1}1/q_i$ as follows

$$\begin{aligned} \frac{1}{2+\beta}\sum_{i=1}^{N-1}\frac{N-i+i}{(N-i)i} &\le \sum_{i=1}^{N-1}\frac{1}{q_i}\le\sum_{i=1}^{N-1}\frac{N-i+i}{(N-i)i} \\ \implies \frac{1}{2+\beta}\sum_{i=1}^{N-1}\left(\frac{1}{N-i}+\frac{1}{i}\right) &\le \sum_{i=1}^{N-1}\frac{1}{q_i}\le\sum_{i=1}^{N-1}\left(\frac{1}{N-i}+\frac{1}{i}\right) \\ \implies \frac{2}{2+\beta}\sum_{i=1}^{N-1}\frac{1}{i} &\le \sum_{i=1}^{N-1}\frac{1}{q_i}\le 2\sum_{i=1}^{N-1}\frac{1}{i} \\ \implies \frac{2}{2+\beta}\ln(N-1) &\le \sum_{i=1}^{N-1}\frac{1}{q_i}\le 2\left(1+\ln(N-1)\right). \end{aligned} \tag{2.56}$$

Next we prove that, for any $1\le i\le N-1$, $\sum_{j=i}^{N-1}\gamma_j/\gamma_i$ is bounded as $N\to\infty$. From the definition of γ_j we see that

$$\frac{\gamma_j}{\gamma_i}=\prod_{k=i+1}^{j}\frac{1}{(1+\beta)+\frac{N}{k}}<\prod_{k=i+1}^{j}\frac{k}{N+k}=\frac{j!}{i!}\frac{(N+i)!}{(N+j)!}. \tag{2.57}$$

Therefore,

$$\sum_{j=i}^{N-1}\frac{\gamma_j}{\gamma_i}<\sum_{j=i}^{N-1}\frac{j!}{i!}\frac{(N+i)!}{(N+j)!}=\frac{1}{N-1}\left[i+N-2N\frac{N!(N+i)!}{i!(2N)!}\right]\le 2.$$

We note that if we set $i=N-1$ in the above, then the limiting value is small, due

to the influence of the negative term that is a ratio of factorials, but the limit must still be positive; in the case $i = 1$ we have a limit that is closer to 1. In all cases, since $1 \leq i \leq N-1$ the limiting value must be non-negative, and at most 2. Hence we see that

$$\lim_{N\to\infty} \sum_{j=i}^{N-1} \frac{\gamma_j}{\gamma_i} \leq 2. \tag{2.58}$$

We now apply the results (2.54), (2.56) and (2.58) to (2.53) in order to deduce the result

$$\tau_1 \leq 4\,(1 + \ln(N-1)) \tag{2.59}$$

which is an upper bound on the expected time, starting in state 1, until the system hits one of the two absorbing states 0 or N. Together with the conclusion of the previous section, in which we computed that the probability that the system arrives in state N tends to 1 as $N \to \infty$, we can conclude that the expected time required for the system to hit state N is no greater than $4(1 + \ln N)$. In using this result later, we will omit the subdominant constant term 1 since we are concerned primarily with values of N for which $\ln N \gg 1$, in the limit $N \to \infty$.

The effect of mutation on the stochastic dynamics

The analysis in the previous two subsections ignored the role of mutation in order to understand the dynamics on the boundary of phase space and, in particular, to estimate the time required to travel along the boundary to a corner.

Since in the absence of mutation the corners are absorbing states, mutation plays an important role in moving the system from a corner (state 0) to state 1 on the boundary, allowing it then to travel further towards the next corner. The mutation rate μ, together with our assumptions on the stochastic dynamics, imply that, for any system state, the time until the next mutation event, M, occurs is exponentially distributed:

$$\mathbb{P}(M > t) = e^{-\mu N t}$$

For system states on the boundary of phase space, we would expect that mutations would move them away, into the interior, where the analysis in the previous sections might become less useful. This is unlikely to happen if mutations are not expected during the time taken for the system to move along the whole boundary, i.e. if

$$\mathbb{P}(\text{hit state } N \text{ before mutation}) = \mathbb{P}(M > 4\ln N) = \mathrm{e}^{-4\mu N \ln N}\,. \tag{2.60}$$

is close to 1. From the form of (2.60), if N is fixed and $\mu \to 0$, then this probability of hitting state N before any mutation occurs tends to 1, which implies that the system remains in boundary states and so the analysis of the parts **'Probability of hitting the absorbing state'** and **'Average hitting time'** applies. On the other hand, if $N \to \infty$, and μ remains fixed, then mutation is expected to occur before the system reaches the next corner, and so the system state tends to leave the boundary. The intermediate balance between these two regimes occurs when $\mu \sim (N \ln N)^{-1}$.

An equivalent discussion can be framed in terms of the sketch of the dynamics indicated in figure 2-11. The time required for a full period of the oscillation is composed of two contribution on each boundary piece: the first contribution τ_{m} is the time required to jump, via mutation, from a corner to a state with one new individual of the appropriate kind. This mutation takes an expected time $\tau_{\mathrm{m}} \sim 1/(N\mu)$ since there are N individuals and each mutates independently at a rate μ. The second contribution τ_1 is the time required to traverse the boundary starting from state 1. This is approximately $\tau_1 = 4 \ln N$. If $\tau_{\mathrm{m}} \gg \tau_1$, i.e. $\mu \ll (4N \ln N)^{-1}$, then the largest contribution to the mean period of oscillation is from the mutation events, and so we expect in this regime to have the period of the orbit being dominated by the time required for three independent mutations to occur, i.e. $T_{SSA} \sim 3/(N\mu)$.

2.2.3 Analysis of the Periodic Orbit in Region II

Region II is the cross-over region between 'large μ' where the ODE approximation is valid, and 'small μ' where the stochastic approach, based on a Markov Chain, is appropriate. Using the analysis of the previous section we see mathematically speaking that region II arises where $\mu \sim (N \ln N)^{-1}$. In region II the stochastic simulations show large fluctuations around the ODE predictions, but the system does not spend time always near the boundaries of phase space, so it is not clear that the analysis of region III should apply directly.

In this section we examine region II, and explain why the fluctuations in the stochastic system act to increase the period of the oscillations rather than to decrease it. This involves a third approach to the dynamics, using a stochastic differential equation derived from the chemical reaction model and which is valid for large, but not infinite, system sizes (this method was introduced in the section 1.3.2). We show that the SDE approach captures, in some detail, the transition between the deterministic and the fully stochastic regimes described in the previous sections.

Stochastic differential equation

It was proved by Kurtz [37] that trajectories of Markov jump processes specified in terms of a stoichiometric matrix $\boldsymbol{S}$ and rate vector $\boldsymbol{r}(\boldsymbol{x})$, as discussed in the sections 1.3.2 and 1.3.3, are well approximated for large N by the trajectories of the SDE

$$\mathrm{d}\boldsymbol{x} = \boldsymbol{u}(\boldsymbol{x})\mathrm{d}t + \frac{1}{\sqrt{N}}\boldsymbol{M}(\boldsymbol{x})\mathrm{d}\boldsymbol{W}(t)\,. \tag{2.61}$$

Here $\mathrm{d}\boldsymbol{W}(t)$ is a vector, each element of which is an independent Wiener process [19], and the vector $\boldsymbol{u}$ and matrix $\boldsymbol{M}$ are given by

$$\boldsymbol{u}(\boldsymbol{x}) = \boldsymbol{S}\boldsymbol{r}(\boldsymbol{x})\,, \quad \boldsymbol{M}(\boldsymbol{x})\boldsymbol{M}^T(\boldsymbol{x}) = \boldsymbol{B}(x)\,. \tag{2.62}$$

where $\boldsymbol{B}_{ij}(\boldsymbol{x}) = \sum_{\boldsymbol{s}_k \in \boldsymbol{S}} r_k s_{ki} s_{kj}$ following (1.38) and $\boldsymbol{S}$ and $\boldsymbol{r}(\boldsymbol{x})$ are given by (2.26). In the calculation of the statistical properties of this equation, it is more useful to consider the matrix $\boldsymbol{B} = \boldsymbol{M}\boldsymbol{M}^T$. For our system we obtain the explicit formulas

$$\begin{aligned}
\boldsymbol{u}_1 &= x_1[x_3 - (1+\beta)x_2 + \beta(x_1x_2 + x_2x_3 + x_1x_3)] + \mu(x_2 + x_3 - 2x_1),\\
\boldsymbol{u}_2 &= x_2[x_1 - (1+\beta)x_3 + \beta(x_1x_2 + x_2x_3 + x_1x_3)] + \mu(x_1 + x_3 - 2x_2),
\end{aligned} \tag{2.63}$$

$$\begin{aligned}
\boldsymbol{B}_{11} &= x_1x_2 + x_3x_1 + (x_1x_2^2 + x_3x_1^2)(2+\beta) + \mu(2x_1 + x_2 + x_3),\\
\boldsymbol{B}_{12} &= \boldsymbol{B}_{21} = -(x_1x_2 + x_1x_2^2(2+\beta) + \mu(x_1 + x_2)),\\
\boldsymbol{B}_{22} &= x_1x_2 + x_2x_3 + (x_1x_2^2 + x_2x_3^2)(2+\beta) + \mu(x_1 + 2x_2 + x_3)\,,
\end{aligned} \tag{2.64}$$

because $x_1 + x_2 + x_3 = 1$. Here we preserve x_3 in these equations to make the expression compact. It does not matter for the next calculation.

Asymptotic phase of points near the periodic orbit

In order to explain the increase in the period of the orbit as the fluctuations grow, we use the SDE (2.61) to derive a SDE equation for the angular velocity around the limit cycle, and we then compute the period of the limit cycle by integrating the angular velocity. Here we extend this idea by deriving an SDE for the angular velocity. This allows us to investigate the effects of noise on the period of the orbit. A fully analytic approach is unfortunately not possible, so our approach is a combination of numerical and analytic methods. Identifying the correct scalings for features of the limit cycle however enables us to confirm the various asymptotic scalings found in regions I and III and to see how they both contribute in this region, region II.

We borrow the idea of asymptotic phase from [58]; figure 2-12 shows an example of the concept. If there is an attracting periodic orbit, then even though given a small

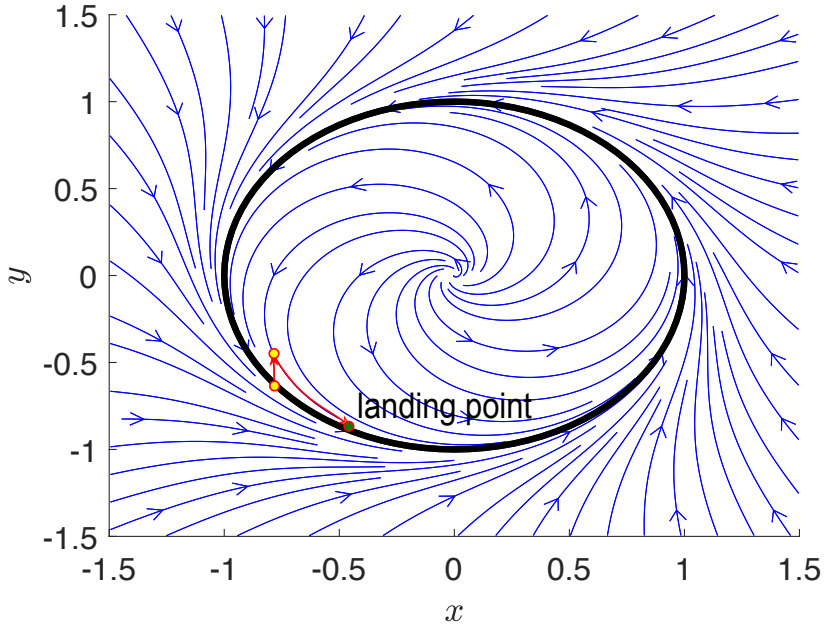

Figure(图) 2-12: Idea from the Newby's paper [58]. Reproduced with permission from [58]. The limit cycle is produced by ODEs in polar coordinates: $\dot{\theta} = \omega, \dot{\rho} = -\rho(\rho^2 - 1)$. Given a small perturbation a point on the stable limit cycle is pushed away from the cycle, but then it goes back by the attraction but located in a different place.

perturbation, the state will find a 'landing point' (green point in figure 2-12) following the flow.

To pursue this analysis we next focus on coordinate transformation to express my model in the form of angular velocity. Since the phase space is two dimensional, we follow the presentation started in the section 1.3.1, showing the periodic orbit in the plane $\mathbb{R}^2$ using coordinates

$$\boldsymbol{y} = (y_1, y_2) = \left(x_1 + \frac{1}{2}x_2, \frac{\sqrt{3}}{2}x_2 \right). \tag{2.65}$$

These, and the following definitions for our coordinate systems, are all illustrated in figure 2-13.

Let $\Gamma \subset \mathbb{R}^2$ be the set of points on the limit cycle, e.g. the red curve in figure 2-13. We further define the polar coordinates (ρ, θ) to be based on the centre of the triangle,

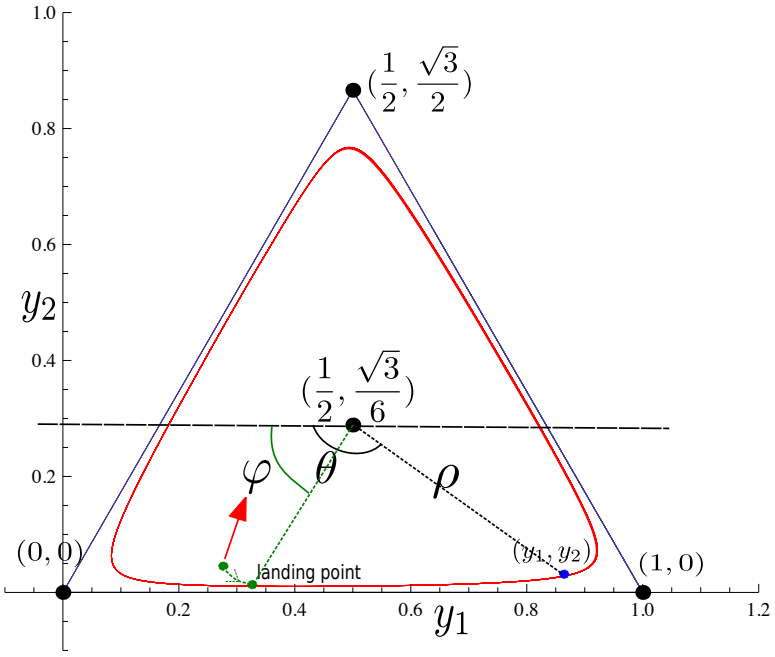

Figure(图) 2-13: The red curve is the limit cycle when $\beta = 1/2, \mu = 1/216$, the blue curve is the limit cycle when $\beta = 1/2, \mu = 10^{-6}$. When μ is very small, it is hard to tell the difference between triangle boundary and limit cycle without zooming-in.

in the $\boldsymbol{y}$ coordinates, i.e. let

$$\rho(\boldsymbol{y}) = \sqrt{\left(y_1 - \frac{1}{2}\right)^2 + \left(y_2 - \frac{\sqrt{3}}{6}\right)^2},$$

and

$$\theta(\boldsymbol{y}) = \arctan\left(\frac{y_1 - 1/2}{\sqrt{3}/6 - y_2}\right).$$

Let T be the period of the limit cycle, i.e. T is the smallest positive value such that $\forall \boldsymbol{y} \in \Gamma$, $\boldsymbol{y}(t) = \boldsymbol{y}(t+T)$ but for any $0 < T' < T$, $\boldsymbol{y}(t) \neq \boldsymbol{y}(t+T')$. All points in the interior of the limit cycle (except the equilibrium point at $\boldsymbol{y} = (1/2, \sqrt{3}/6)$ are attracted to the limit cycle, enabling us to define a 'landing point' on Γ to which they are asymptotically attracted. Although the ω-limit set of a point $\boldsymbol{y}_0 \in \mathbb{R}^2$ would clearly be the entire orbit Γ, by looking at the sequence defined by advancing for multiples of the period T we can identify a single limit point $p_\infty(\boldsymbol{y}_0)$. Specifically we write the time-evolution map for the ODEs as $\phi_t(\boldsymbol{y}_0) := \boldsymbol{y}(t)$ where $\boldsymbol{y}(t)$ solves the ODEs (2.16)

subject to the initial condition $\boldsymbol{y}(0) = \boldsymbol{y}_0$. Then we define the sequence $\{p_n\}_{n\geq 0}$ by

$$p_n = \phi_{nT}(\boldsymbol{y}_0), \quad \text{and} \quad p_0 = \boldsymbol{y}_0.$$

and the limit point

$$p_\infty(\boldsymbol{y}_0) := \lim_{n\to\infty} \phi_{nT}(\boldsymbol{y}_0).$$

Note that $p_\infty(\boldsymbol{y}_0) \in \Gamma$ always, and that if $\boldsymbol{y}_0 \in \Gamma$ then $p_\infty(\boldsymbol{y}_0) = \boldsymbol{y}_0$.

We can now define the asymptotic phase $\varphi(\boldsymbol{y}_0)$ of a point near, but not necessarily on, the limit cycle by setting

$$\varphi(\boldsymbol{y}_0) := \theta(p_\infty(\boldsymbol{y}_0)). \tag{2.66}$$

So that if $\boldsymbol{y}_0 \in \Gamma$, then $\varphi(\boldsymbol{y}_0) = \theta(\boldsymbol{y}_0)$, and curves on which $\varphi(\boldsymbol{y}_0)$ is constant cross through Γ at these points. We can use $\varphi(\boldsymbol{y}_0)$ to consider the influence of noise, which pushes trajectories off the limit cycle, causing time advances or delays, as illustrated in figure 2-14(b). This concept has been explored recently for a more general class of limit cycles in [58] (see figure 2-14(a)), whose approach we follow here. It is analogous to the noise-induced drift observed in various ecological models including invasions [64] and the evolution of altruism [8]; see [65] for an introduction.

The three-fold rotation symmetry of the problem suggests that it is enough to focus on the interval $\varphi \in [-\pi/3, \pi/3]$. In general, in this subsection we transform the state with the vector variable (x_1, x_2, x_3) to a scalar variable θ. This dimensional reduction simplifies our understanding and calculation of asymptotic phase φ of the state in the 'triangle' of figure 2-13.

A stochastic differential equation for φ

Since φ is a function on the phase space, we can derive an SDE for the evolution of φ using (2.61) and Itô's formula [19] (see in appendix A). We obtain

$$\begin{aligned} \mathrm{d}\varphi(\boldsymbol{x}) = &\left\{ \sum_i \boldsymbol{u}_i(\boldsymbol{x},t)\partial_i\varphi(\boldsymbol{x}) + \frac{1}{2N}\sum_{i,j} \left[\boldsymbol{B}(\boldsymbol{x},t)\right]_{ij} \partial_i\partial_j\varphi(\boldsymbol{x}) \right\} \mathrm{d}t \\ &+ \frac{1}{\sqrt{N}} \sum_{i,j} \boldsymbol{M}_{ij}(\boldsymbol{x},t)\partial_i\varphi(\boldsymbol{x})\mathrm{d}\boldsymbol{W}_j(t). \end{aligned} \tag{2.67}$$

Note that our notation $\varphi(\boldsymbol{x})$ really means $\varphi(\boldsymbol{y}(\boldsymbol{x}))$ since φ is defined by (2.66) which uses the coordinates $\boldsymbol{y}$ defined in (2.65). The advection vector $\boldsymbol{u}$ and the matrix

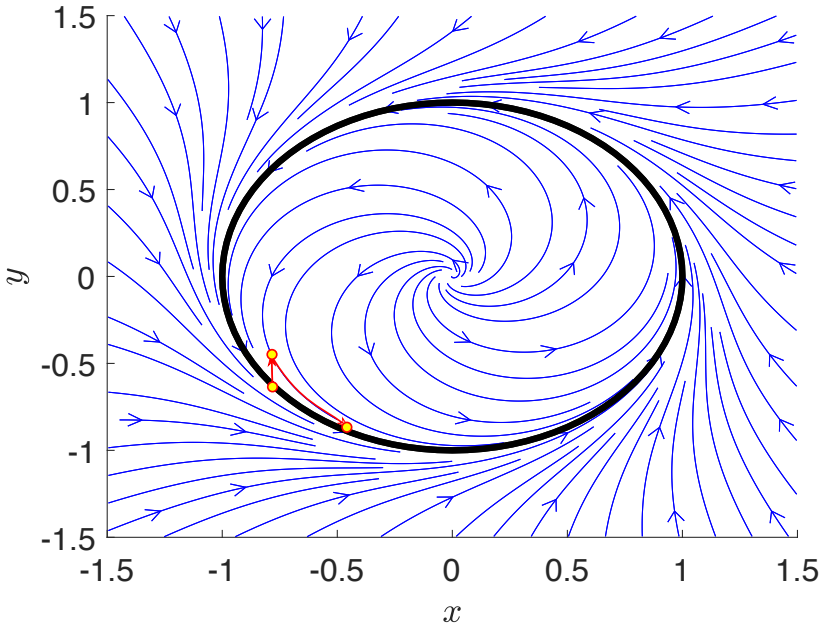

(a)

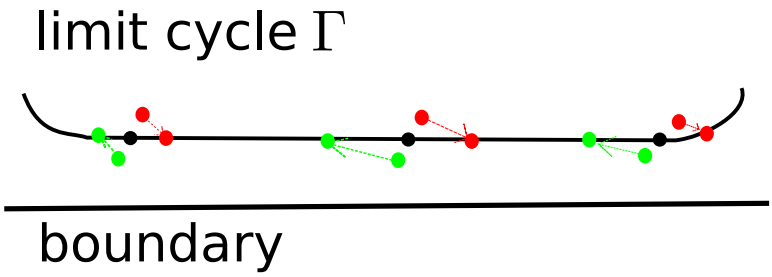

(b)

Figure(图) 2-14: (a) Idea from the Newby's paper [58]. (b) Application of the idea to our model, using the lower part of Γ as shown in the (y_1, y_2) plane. Each of the three black points lies on the limit cycle Γ: trajectories evolve along Γ from left to right in the figure. Perturbations of these points (in green) towards the boundary lead to trajectories that have longer periods than Γ has, hence the green arrows indicate the asymptotic convergence of trajectories back to the limit cycle to points that lie to the left of the black dots. In contrast, perturbations (red dots) towards the interior of Γ lead to states that are accelerated by trajectories and converge asymptotically to points on Γ that are ahead of the black dots.

$\boldsymbol{B} \equiv \boldsymbol{M}\boldsymbol{M}^T$ are those given previously in (2.63) and (2.64).

Although analytic expressions for φ and its first and second derivatives in phase space, i.e. $\partial_1\varphi$, $\partial_2\varphi$, $\partial_1^2\varphi$, $\partial_1\partial_2\varphi$, and $\partial_2^2\varphi$ are unknown, they can be estimated numerically. Since we are interested in the behaviour of perturbations near Γ, we have estimated these derivatives at points on Γ and then used them to define two functions of φ:

$$\begin{aligned} \omega_\infty(\varphi(\boldsymbol{x})) &:= \sum_i \boldsymbol{u}_i(\boldsymbol{x},t)\partial_i\varphi(\boldsymbol{x}), \quad \text{and} \\ \omega_1(\varphi(\boldsymbol{x})) &:= -\frac{\mu}{2}\sum_{i,j}\left[\boldsymbol{B}(\boldsymbol{x},t)\right]_{ij}\partial_i\partial_j\varphi(\boldsymbol{x}). \end{aligned} \tag{2.68}$$

Note that we have included in the definition of ω_1 a prefector of μ. This is necessary since the stochastic slowdown effect is stronger for smaller μ, as indicated by the previous stochastic analysis, and shown numerically in the left panel of figure 2-16. We can conclude that, curiously, whilst the noise itself has negligible strength (order $1/N$) in region II, the noise-induced slowdown has an order one impact on the dynamics. Specifically, the leading order form of equation (2.67) in large N and small μ is simply

$$\frac{\mathrm{d}}{\mathrm{d}t}\varphi = \omega_\infty(\varphi) - \frac{1}{N\mu}\omega_1(\varphi), \tag{2.69}$$

which enables us investigate the contributions to the period of the limit cycle of the advection term $\boldsymbol{u}$ and the fluctuation-related contribution $\boldsymbol{B}$, separately.

Figures 2-15 and 2-16 show numerically-computed approximations to the two functions $\omega_\infty(\varphi)$ and $\omega_1(\varphi)$, respectively. We observe that ω_∞ remains positive as φ increases, with a maximum near, but not exactly at, $\varphi = 0$. This shows that points on Γ move in the direction of increasing φ; there is no reason for any symmetry about $\varphi = 0$ due to the cyclic nature of the dynamics. The shape of the curve $\omega_\infty(\varphi)$ varies little with μ except near the equilibrium points in the corners, near $\varphi = \pm\pi/3$. Figure 2-16 shows the variation in $\omega_1(\varphi)$ as μ increases. Note that the definition of ω_1 in (2.68) contains a factor of μ: including this factor of μ yields curves for $\omega_1(\varphi)$ that are extremely close to each other even as μ increases by a factor of 16. Note also that the curves tend to zero at both ends, indicating that the changes in μ do not change the contribution from $\omega_1(\varphi)$ to the time spent near each equilibrium point. In the first part of the plot, $\omega_1(\varphi)$ is negative, indicating that the angular velocity here overall, from (2.69), is increased, so that the period of the orbit would be decreased. But this effect is more than compensated for by the behaviour in the second part of the plot where $\omega_1(\varphi)$ becomes more strongly positive, leading to a decrease in the overall angular velocity here, and hence a larger increase in the period of the orbit. The combined

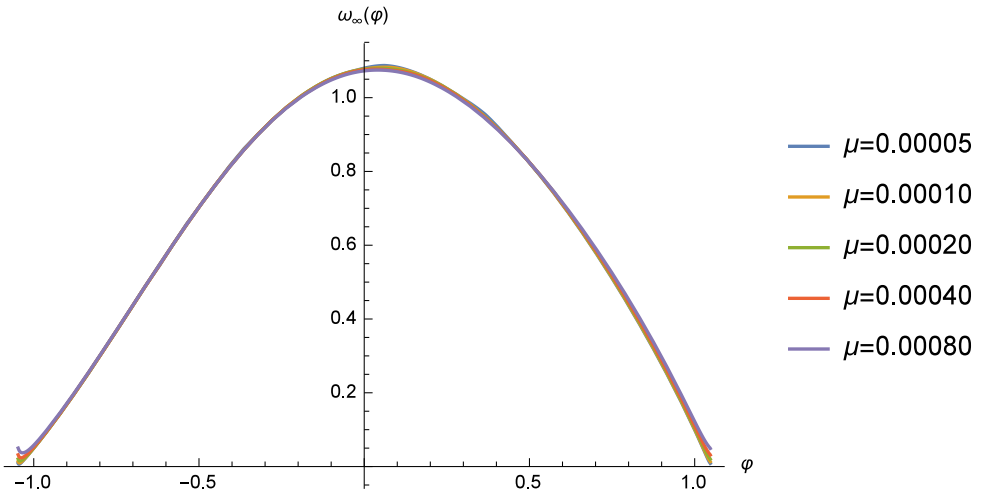

Figure(图) 2-15: Numerically-computed function $\omega_\infty(\varphi)$ for five different values of μ from 5×10^{-5} up to 8×10^{-4}.

effect is therefore to increase the period of the deterministic orbit which is only given by ω_∞, and this increase is driven directly by the fluctuations described by the matrix $\boldsymbol{B}$ in the original SDE.

Equation (2.67) can be used to quantify these contributions to the period of the orbit since the expected period of the limit cycle can be computed from the SDE (2.67) by writing

$$T_{\mathrm{SDE}} = 3\int_{-\frac{\pi}{3}}^{\frac{\pi}{3}} \frac{\mathrm{d}\varphi}{\dot{\varphi}} = 3\int_{-\frac{\pi}{3}}^{\frac{\pi}{3}} \frac{\mathrm{d}\varphi}{\omega_\infty(\varphi) - \frac{1}{N\mu}\omega_1(\varphi)}, \tag{2.70}$$

which, considering the case $N \gg 1$, can be approximated by

$$T_{\mathrm{SDE}} = 3\int_{-\frac{\pi}{3}}^{\frac{\pi}{3}} \frac{\mathrm{d}\varphi}{\omega_\infty(\varphi)} + \frac{3}{N\mu}\int_{-\frac{\pi}{3}}^{\frac{\pi}{3}} \frac{\omega_1(\varphi)}{\omega_\infty^2(\varphi)}\mathrm{d}\varphi + O\left(\frac{1}{N^2}\right).$$

The first integral on the right hand side corresponds to the ODE approximation $T_{\mathrm{ODE}} \approx 3\ln(1/\mu)$, valid for larger μ; we infer that $\omega_\infty(\varphi)$ depends (relatively weakly) on μ. The second integral contains the leading-order N-dependent behaviour and shows that this is a contribution to the period that scales as $T \propto 1/(N\mu)$. Although ω_∞ depends on μ, as observed above, this dependence is visible most obviously near to the equilibrium points at which points $\omega_1(\varphi)$ is close to zero. Overall we might therefore expect the μ-dependence of the second integral to be even weaker than than $\ln\mu$ dependence of the $\omega_\infty(\varphi)$ function itself. If this were the case, we would be left with just the $T \propto 1/(N\mu)$ dependence that would come to dominate the expression for T_{SDE} for small μ.

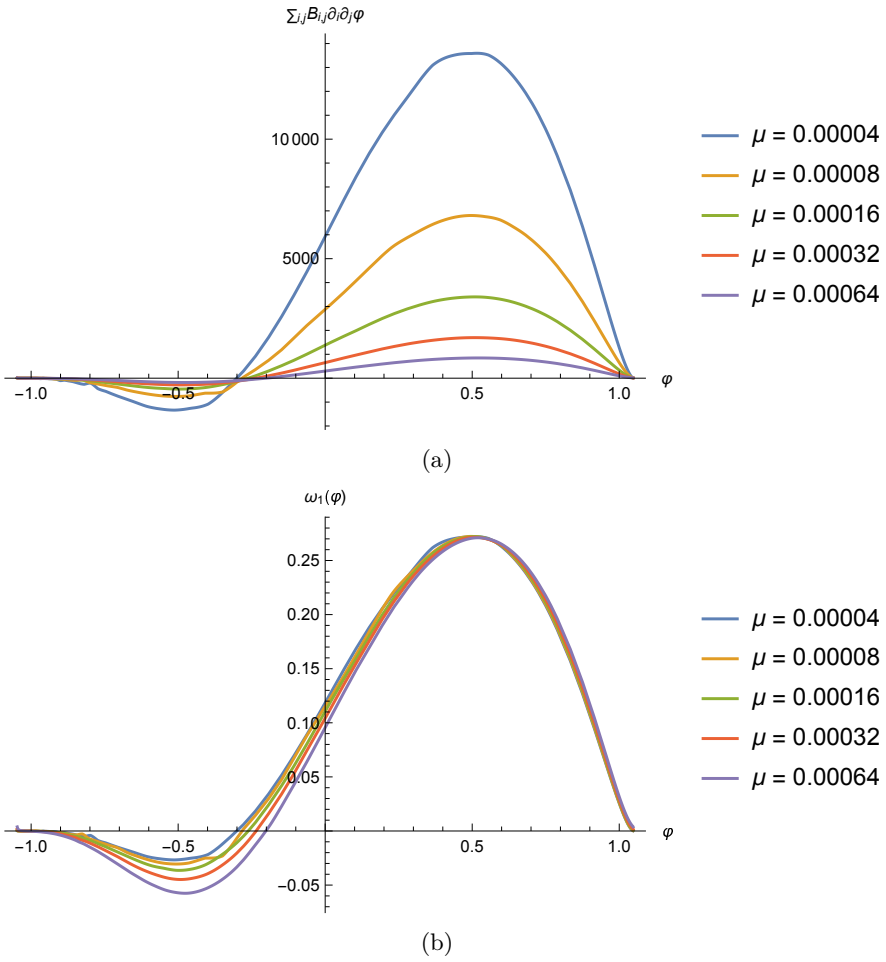

Figure(图) 2-16: (a) Numerically-computed functions $\sum_{i,j} [\boldsymbol{B}(\boldsymbol{x},t)]_{ij} \partial_i \partial_j \varphi$ for five different values of μ. (b) Numerically-computed function $\omega_1(\varphi)$, the data collapse visible here justifies the inclusion of the explicit factor of μ in the defintion (2.68). Note that ω_1 appears to cross through zero close to $\varphi = \pm\pi/3$.

In this way we observe that the SDE is able to capture the effects of fluctuations near the limit cycle and yields an expression for the period of oscillations that indicates that the period increases as μ decreases, leading into region III-type scaling at small μ. Moreover, at larger μ (and larger N at fixed μ) we observe that the period of oscillations is given by the deterministic expression computed for region I. Hence this analysis of region II is able to capture the cross-over in scalings for the periodic orbit as we move between regions I and III.

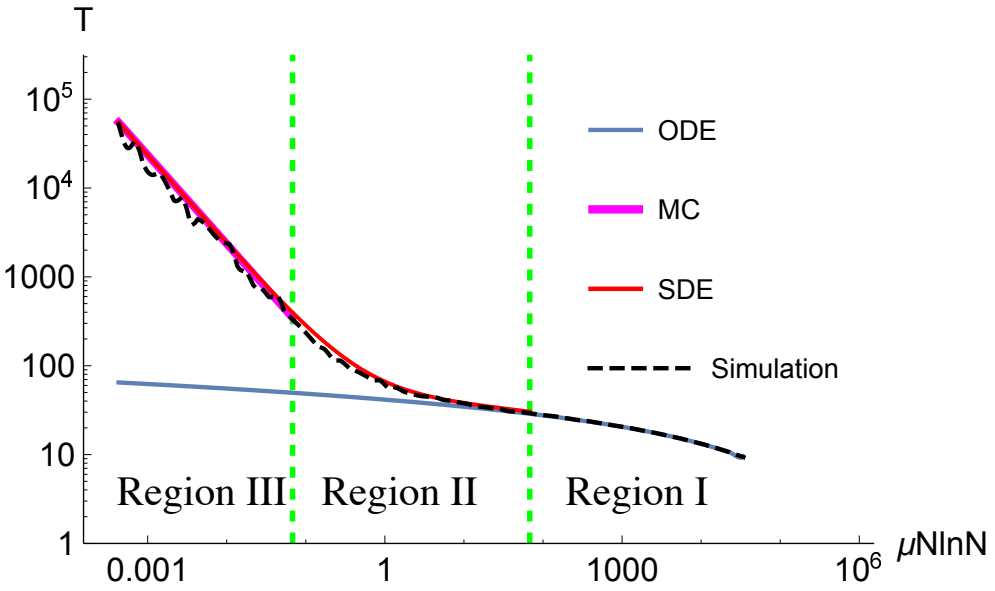

Figure(图) 2-17: A summary of the three regions for the dynamics, comparing the theoretical predictions for the mean period T of oscillations each region with the results of stochastic simulations for $N = 2^{17}$.

2.2.4 Short Summary

At the end of section 2.1.2, we presented figure 2-7 to illustrate the goal of analysing the mean period of oscillations in three different regions of μ. In section 2.2, we use three different theoretical analyses to explain the three regions in detail. The conclusions are summerised in figure 2-17 tells us everything.

In figure 2-17, the solid blue curve and the dashed black curve are taken from figure 2-7. They represent ODE solution about period of the limit cycle and the mean period of the stochastic simulations respectively. Then in different regions, our theoretical derivations are confirmed by the simulation results. In region I, the ODE result coincides with the simulation well. We combine local and global maps to predict the period of cycles by analysing ODEs. In region II, the SDE result in section 2.2.3 (which is drawn as a red solid line) also explains the crossover between I and III well. In region III, we analysed an effective Markov process to estimate the 'period' of the cycles occurring in the stochastic simulations, and the thick magenta line fits the simulation perfectly.

Chapter 3

Four Species Competition 四种群竞争

The Rock-Paper-Scissors model discussed in chapter 2 is the simplest setting in which to discuss cyclic domainance between multiple species. 'Simplest' means that the phase space has the lowest possible dimension; when the constraint of a constant population size N is taken into account, the system is effectively two dimensional. This, in turn, restricts the possible kinds of dynamics present in the mean-field ODEs (for example, chaotic dynamics are not possible). It also simplifies the Markov Chain analysis in region III since the dynamics takes place near the boundary of the phase space, which is a one-dimensional set.

Competition between four or more species allows the dynamics to potentially become qualitatively more complicated, introduces new bifurcations and additional problem parameters, and means that analysis (in both the mean-field ODE and Markov Chain cases) becomes more complicated to carry out. In the last few years, there has been a number of studies dedicated to various aspects of the dynamics of 4 species in cyclic competition. In [16], deterministic trajectories (e.g. saddles, arrows, and spirals) were studied in cyclic competition of four species. In [14], the authors considered the cyclic four-species Lotka–Volterra model and investigated the stochastic behaviour in the extinction process. In [33], global stability properties of Lotka-Volterra networks (with four or five species) were investigated. Lastly in 2018, Dobramysl and Mobilia offered a very detailed review for four species cyclic competition in section 4 of [13].

In this chapter we set out the same initial investigations for the simplest four-species extension of the RPS model investigated in detail in chapter 2. Most of our attention is focussed on the mean-field ODE regime, and we outline directions for future research that would link this to the result of stochastic individual-based simulations

more closely.

The RPS model is the simplest toy model for studying the oscillations of species competition. The model looks simple, while it produces rich variants and shows us many possible interesting behaviours (discussed in chapter 2). In this chapter, we extend the RPS model (which is about three-species competition) into a four-species competition model. As before, we first express the model with a payoff matrix, which represents the average earning and losing in the competition, and develop from the mean-field model chemical reactions and perform stochastic simulations.

3.1 Model

We consider the simplest extension of the RPS dynamics to the case of four species $\{X_1, X_2, X_3, X_4\}$ competing in a closed environment, i.e. the total population size is held constant. The competitive relations between the four species can be summurised by the payoff matrix below.

	X_1	X_2	X_3	X_4
X_1	0	1	ε_3	$-1-\beta$
X_2	$-1-\beta$	0	1	ε_4
X_3	ε_1	$-1-\beta$	0	1
X_4	1	ε_2	$-1-\beta$	0

Table(表) 3.1: Payoff to the species in the row label of pairwise interactions between the species $\{X_1, X_2, X_3, X_4\}$.

As in chapter 3 we allow for unbalanced, win-lose asymmetric, interactions when $\beta > 0$. We note also that the payoffs $\varepsilon_1, ..., \varepsilon_4$ are new and have no analogue in the three-species interactions. The value of the ε_j allow for greater variety in the dynamics. The corresponding payoff matrix P is given by:

$$P := \begin{pmatrix} 0 & -1-\beta & \varepsilon_1 & 1 \\ 1 & 0 & -1-\beta & \varepsilon_2 \\ \varepsilon_3 & 1 & 0 & -1-\beta \\ -1-\beta & \varepsilon_4 & 1 & 0 \end{pmatrix} \tag{3.1}$$

3.1.1 Replicator Equations

We write x_i as the proportion of species X_i in the system, so that $x_1+x_2+x_3+x_4 = 1$. Following section 1.3.1, the evolution of $x_i(t)$ in the mean field limit is supposed to be given by the replicator equations according to equation (1.1), assuming an infinite

population:

$$\dot{x_i}(t) = x_i(t)\left(\sum_j P_{ij}x_j(t) - \sum_{j,k} P_{jk}x_j(t)x_k(t)\right), \quad i,j,k \in \{1,2,3,4\}. \tag{3.2}$$

If P is an anti-symmetric matrix, the double sum on the right will vanish and the simplest corresponding reactions are clear (i.e. similar to the case discussed in section 2.1.1). This would be the case if $\beta = 0$ and $\varepsilon_1 = -\varepsilon_3$ and $\varepsilon_2 = -\varepsilon_4$. Now we are more interested in a more general case when P is not anti-symmetric. Note from (3.2) that it is only the symmetric part of P that is important; i.e. we can replace P by $\frac{1}{2}(P + P^T)$ in (3.2) without changing the dynamics of the replicator equations.

Writing the 4 equations for $x_1, \ldots, x_4$ out explicitly from (3.2), including mutation, as previously, we obtain the system of ODEs

$$\begin{aligned}
\dot{x}_1 &= x_1[x_4 - (1+\beta)x_2 + \varepsilon_1 x_3 + \beta X - Y] + \mu(x_2 + x_3 + x_4 - 3x_1),\\
\dot{x}_2 &= x_2[x_1 - (1+\beta)x_3 + \varepsilon_2 x_4 + \beta X - Y] + \mu(x_1 + x_3 + x_4 - 3x_2),\\
\dot{x}_3 &= x_3[x_2 - (1+\beta)x_4 + \varepsilon_3 x_1 + \beta X - Y] + \mu(x_1 + x_2 + x_4 - 3x_3),\\
\dot{x}_4 &= x_4[x_3 - (1+\beta)x_1 + \varepsilon_4 x_2 + \beta X - Y] + \mu(x_1 + x_2 + x_3 - 3x_4).
\end{aligned} \tag{3.3}$$

with $X := x_1x_2 + x_2x_3 + x_3x_4 + x_4x_1$ and $Y := (\varepsilon_1 + \varepsilon_3)x_1x_3 + (\varepsilon_2 + \varepsilon_4)x_2x_4$.

3.1.2 Technique of Finding Reactions

Similar to section 2.1.2, we can deduce a set of chemical reactions from the ODEs (3.3). The reaction scheme has the same dynamics in mean-field but provides a way to carry out explicit simulations at the individual level.

Specifically, to find a chemical reaction scheme that contains only positive rates (assuming β is positive in finding the reactions scheme) we replace the term $\varepsilon_i x_i^2 x_{i+2}$ in i-th equation with the exactly equivalent term $\varepsilon_i x_i x_{i+2}(1 - \sum_{j\neq i} x_j)$ (here $i+2 = (i+1) \pmod 4 + 1$). After tidying up (3.3), we can obtain a system of n reactions with positive rates by considering $\dot{\boldsymbol{x}} = \boldsymbol{S}\boldsymbol{r}(\boldsymbol{x})$, where $\boldsymbol{S}$ is jump matrix with size $4 \times n$ and entries $\{0,+1,-1\}$, and $\boldsymbol{r}$ is the rate matrix with n positive entries. The number n is the total number of reactions. These notations follow the earlier section 1.3.3. For the ODEs (3.3), we obtain the corresponding $\boldsymbol{S}$ and $\boldsymbol{r}(\boldsymbol{x})$ as follows:

$$\boldsymbol{S} := (\boldsymbol{S}_1, \boldsymbol{S}_2, \boldsymbol{S}_3, \boldsymbol{S}_4), \tag{3.4}$$

$$\boldsymbol{r} := \begin{bmatrix} \boldsymbol{r}_1 \\ \boldsymbol{r}_2 \\ \boldsymbol{r}_3 \\ \boldsymbol{r}_4 \end{bmatrix}, \tag{3.5}$$

constructed out of four separate pieces given by

$$\boldsymbol{S}_1 = \begin{pmatrix} -1 & 0 & 0 & 1 \\ 1 & -1 & 0 & 0 \\ 0 & 1 & -1 & 0 \\ 0 & 0 & 1 & -1 \end{pmatrix}, \boldsymbol{r}_1 = (x_1x_2, x_2x_3, x_3x_4, x_4x_1)^T. \tag{3.6}$$

$$\boldsymbol{S}_2 = \begin{pmatrix} 1 & 1 & 1 & -1 & 0 & 0 & 0 & 0 & -1 & -1 & 0 & 0 \\ -1 & 0 & 0 & 1 & 1 & 1 & -1 & 0 & 0 & 0 & 0 & -1 \\ 0 & -1 & 0 & 0 & -1 & 0 & 1 & 1 & 1 & 0 & -1 & 0 \\ 0 & 0 & -1 & 0 & 0 & -1 & 0 & -1 & 0 & 1 & 1 & 1 \end{pmatrix}, \tag{3.7}$$

$$\begin{aligned} \boldsymbol{r}_2 = (&\varepsilon_1 x_1x_2x_3, \varepsilon_1 x_1x_3x_4, \varepsilon_1 x_1x_3^2, \varepsilon_2 x_1x_2x_4, \varepsilon_2 x_1x_3x_4, \varepsilon_2 x_2x_4^2, \\ &\varepsilon_3 x_1x_2x_3, \varepsilon_3 x_2x_3x_4, \varepsilon_3 x_1^2x_3, \varepsilon_4 x_1x_2x_4, \varepsilon_4 x_2x_3x_4, \varepsilon_4 x_2^2x_4)^T. \end{aligned} \tag{3.8}$$

$$\boldsymbol{S}_3 = \begin{pmatrix} -1 & -1 & 0 & 0 & 0 & 0 & 1 & 1 \\ 1 & 1 & -1 & -1 & 0 & 0 & 0 & 0 \\ 0 & 0 & 1 & 1 & -1 & -1 & 0 & 0 \\ 0 & 0 & 0 & 0 & 1 & 1 & -1 & -1 \end{pmatrix}, \tag{3.9}$$

$$\boldsymbol{r}_3 = \beta(x_1x_2^2, x_1x_2x_4, x_2x_3^2, x_2x_3x_1, x_3x_4^2, x_3x_4x_2, x_4x_1^2, x_4x_1x_3)^T. \tag{3.10}$$

$$\boldsymbol{S}_4 = \begin{pmatrix} -1 & -1 & -1 & 1 & 0 & 0 & 1 & 0 & 0 & 1 & 0 & 0 \\ 1 & 0 & 0 & -1 & -1 & -1 & 0 & 1 & 0 & 0 & 1 & 0 \\ 0 & 1 & 0 & 0 & 1 & 0 & -1 & -1 & -1 & 0 & 0 & 1 \\ 0 & 0 & 1 & 0 & 0 & 1 & 0 & 0 & 1 & -1 & -1 & -1 \end{pmatrix}, \tag{3.11}$$

$$\boldsymbol{r}_4 = \mu(x_1, x_1, x_1, x_2, x_2, x_2, x_3, x_3, x_3, x_4, x_4, x_4)^T. \tag{3.12}$$

The jump matrix $\boldsymbol{S}_1$ and vector $\boldsymbol{r}_1$ represent the cyclic competition between the four species. The jump matrix $\boldsymbol{S}_2$ and vector $\boldsymbol{r}_2$ illustrate all the allowed reactions with rates ε_i. The jump matrix $\boldsymbol{S}_3$ and vector $\boldsymbol{r}_3$ represent all reactions with rate β which allow the payoff to be unbalanced. Finally, the jump matrix $\boldsymbol{S}_4$ and vector $\boldsymbol{r}_4$ represent all the mutation reactions with rate μ.

The complete system contains a total of 36 chemical reactions:

$$X_i + X_{i+1} \xrightarrow{1} 2X_{i+1}, \qquad i \in \{1,2,3,4\}, \tag{3.13}$$

$$X_i + X_j + X_{i+2} \xrightarrow{\varepsilon_i} 2X_i + X_{i+2}, \qquad i,j \in \{1,2,3,4\}, \text{ and } i \neq j, \text{ if } \varepsilon_i > 0 \tag{3.14}$$

$$X_i + X_j + X_{i+2} \xrightarrow{-\varepsilon_i} 2X_j + X_{i+2}, \qquad i,j \in \{1,2,3,4\}, \text{ and } i \neq j, \text{ if } \varepsilon_i < 0 \tag{3.15}$$

$$X_i + X_{i+1} + X_{i+1} \xrightarrow{\beta} 2X_{i+1} + X_{i+1}, \quad i \in \{1,2,3,4\}, \text{ if } \beta > 0 \tag{3.16}$$

$$X_i + X_{i+1} + X_{i+3} \xrightarrow{\beta} 2X_{i+1} + X_{i+3}, \quad i \in \{1,2,3,4\}, \text{ if } \beta > 0 \tag{3.17}$$

$$X_i + X_{i+1} + X_{i+1} \xrightarrow{-\beta} 2X_i + X_{i+1}, \quad i \in \{1,2,3,4\}, \text{ if } \beta < 0 \tag{3.18}$$

$$X_i + X_{i+1} + X_{i+3} \xrightarrow{-\beta} 2X_i + X_{i+3}, \quad i \in \{1,2,3,4\}, \text{ if } \beta < 0 \tag{3.19}$$

$$X_i \xrightarrow{\mu} X_j, \qquad i,j \in \{1,2,3,4\}, \text{ and } i \neq j \tag{3.20}$$

here all indices should be interpreted cyclically, i.e. $i+k := (i+k-1) \pmod 4 + 1$ and in the reactions with rate ϵ_i or β there are catalytic effects: species are necessary for a reaction to proceed but are not used up in the reaction itself. The parameters ε_i and β can be positive, negative and zero, so we list all possible reactions here in different cases.

3.1.3 Existence and Stability of Equilibria

First of all, to make the derivation of stability tractable, we assume that the mutation rate $\mu = 0$ and all $\varepsilon_i = \varepsilon$. The steady states from the ODEs (3.3) can be classified into 3 types: (1) interior equilibrium. (1/4,1/4,1/4,1/4); (2) edge equilibrium. $v_{13} = (1/2, 0, 1/2, 0)$, $v_{24} = (0, 1/2, 0, 1/2)$, or $v_{12} = ((1+\beta)/\beta, -1/\beta, 0, 0)$ and its permutations with $\beta \leq -1$; (3) vertex equilibria. (1,0,0,0) and its permutations. Figure 3-1 describes the stability of all the equilibria in the $\beta - \varepsilon$ plane. Different regions in figure 3-1 correspond to different attractors for typical trajectories of the ODEs (3.3) in the case $\mu = 0$.

In the following subsections, we will present the detailed mathematical analysis of these equilibria, and based on their stability we obtain some inequalities about parameters β and ε. All the relationships are illustrated in digram 3-1.

Inner equilibrium.

The interior equilibrium $(1/4, 1/4, 1/4, 1/4)$ is stable if the eigenvalues of the Jacobian Matrix evaluated at the equilibrium, have negative real parts. Direct computation

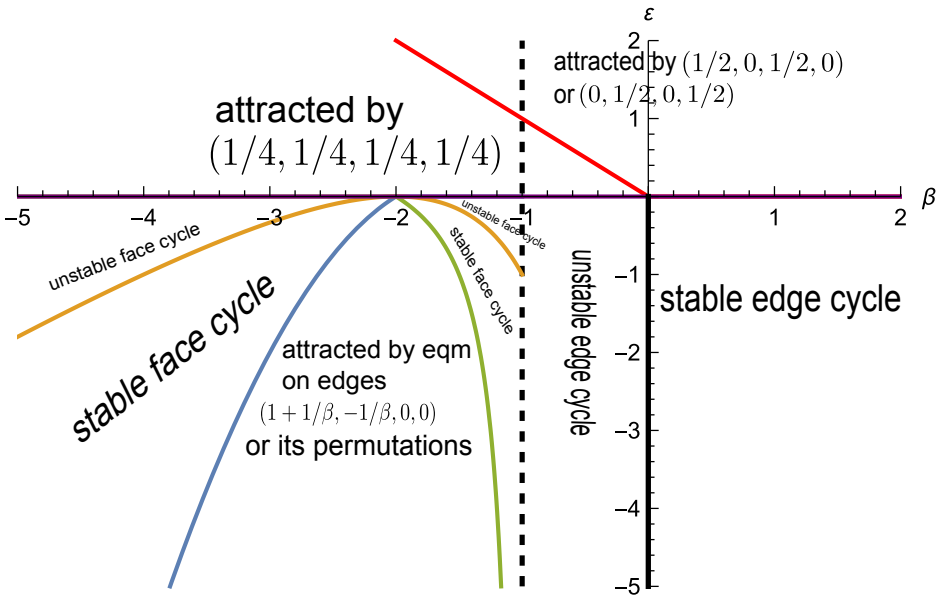

Figure(图) 3-1: Dynamics in different regions of the (β, ε) plane when $\mu = 0$. The purple line is $\varepsilon = 0$, and the red line is $\varepsilon = -\beta$, which are both derived from the stability analysis of the inner equilibrium and the edge equilibria $(1/2, 0, 1/2, 0)$. The black dashed line is $\beta = -1$, which is the critical value of existence of equilibrium $v_{12} = (\frac{1+\beta}{\beta}, -\frac{1}{\beta}, 0, 0)$. The blue solid curve is $\varepsilon = -(\beta+1)(\beta+2)$, and the green solid curve is $\varepsilon = (2+\beta)/(1+\beta)$. These two are critical curves of stable equilibria v_{12} and its permutations. The yellow curve is $\varepsilon = (\beta+2)^2/\beta$ and the black line is $\beta = 0$. They are critical curves which are derived in stability analysis of heteroclinic cycles in section 3.2.1. The 'face cycle' and 'edge cycle' are shown in figure 3-4

shows that the eigenvalues are:

$$\left\{\frac{\beta-\varepsilon}{4}, \frac{1}{4}[-\varepsilon-(\beta+2)\mathrm{i}], \frac{1}{4}[-\varepsilon+(\beta+2)\mathrm{i}], \frac{\beta+\varepsilon}{4}\right\}.$$

This equilibrium point is therefore stable when $0 < \varepsilon < -\beta$ (all trajectories finally are stable in figure 3-2). In Figure 3-1, this corresponds to the region in the second quadrant between the red line $\varepsilon = -\beta$ and the purple line $\varepsilon = 0$.

Edge equilibria.

1. For these equilibria on the edges, i.e. $v_{13} := (1/2, 0, 1/2, 0)$ or $v_{24} := (0, 1/2, 0, 1/2)$, the eigenvalues of the Jacobian matrix are:

$$\left\{\frac{1}{2}(-\beta-\varepsilon), \frac{1}{2}(-\beta-\varepsilon), -\frac{\varepsilon}{2}, -\frac{\varepsilon}{2}\right\}.$$

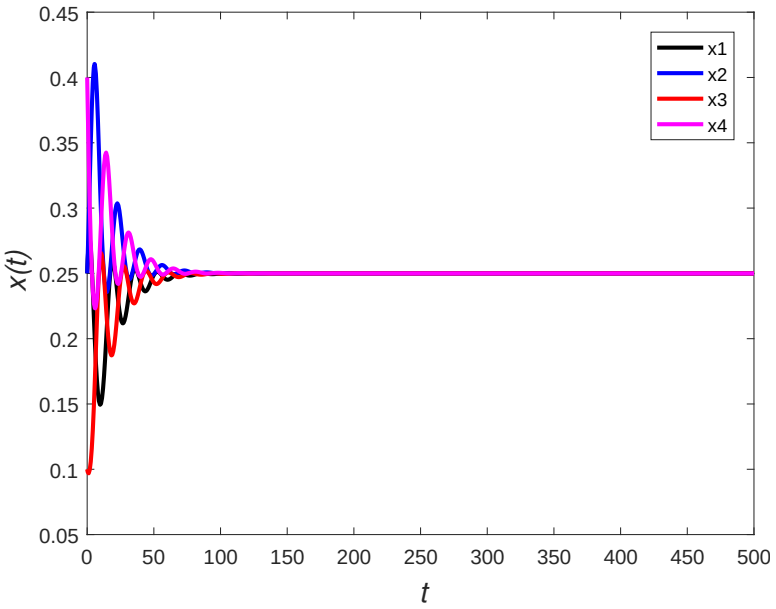

Figure(图) 3-2: A solution of ODEs (3.3). It is an example of the inner equilibrium with $\beta = -0.5$ and $\varepsilon = 0.25$.

Hence these equilibria are stable when $\varepsilon > 0$, and $\varepsilon > -\beta$ (the blue and the magenta trajectories are stable at $1/2$ and the black and red ones are stable at 0 in figure 3-3(a)). The relationship $\beta - \varepsilon$ is illustrated in the region above red line and purple line (the whole of the first quadrant and half of the second quadrant) in Figure 3-1.

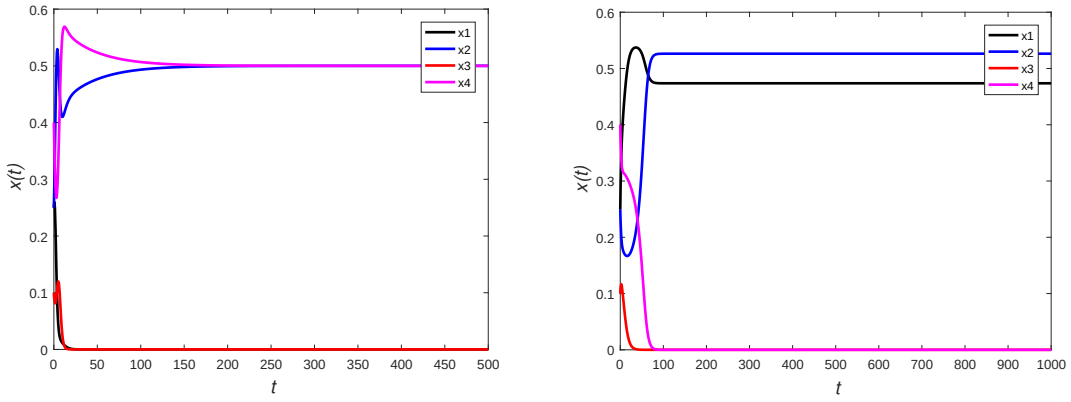

(a) (b)

Figure(图) 3-3: Solutions of ODEs (3.3). Panel (a) shows an example of the edge equilibrium $v_{24} = (0, 1/2, 0, 1/2)$ with $\beta = 0.8$ and $\varepsilon = 0.05$. Panel (b) shows an example of the edge equilibrium $(v_{12}, v_{23}, 0, 0) = (1 + 1/\beta, -1/\beta, 0, 0)$ with $\beta = -1.9$ and $\varepsilon = -0.3$.

2. Similarly, by studying the local dynamics around the point $v_{12} := ((1+\beta)/\beta, -1/\beta, 0, 0)$, we obtain the Jacobian matrix

$$J_1 = \begin{pmatrix} -\frac{\beta+1}{\beta} & 0 & -\frac{(\beta+1)(\varepsilon\beta+\beta+2\varepsilon)}{\beta^2} & \frac{(\beta+1)\left(\beta^2+2\beta+2\varepsilon\right)}{\beta^2} \\ 0 & -\frac{\beta+1}{\beta} & \frac{\beta^2+2(\varepsilon+1)\beta+2\varepsilon}{\beta^2} & -\frac{\beta^2+\varepsilon\beta+\beta+2\varepsilon}{\beta^2} \\ 0 & 0 & \frac{\beta(\varepsilon-1)+\varepsilon-2}{\beta} & 0 \\ 0 & 0 & 0 & -\frac{\beta^2+3\beta+\varepsilon+2}{\beta} \end{pmatrix} \tag{3.21}$$

Note, first, that the equilibrium point exists when $\beta < -1$ because $0 < x_1, x_2 < 1$. This corresponds to the region in the figure 3-1 to the left side of the dashed line $\beta = -1$. Secondly, it is stable when all eigenvalue of J_1 are negative. Obviously, we see that when v_{12} exists, $-(\beta+1)/\beta < 0$. These are sometimes referred to as 'radial' eigenvalues since they correspond to perturbations in the two coordinate directions in which we have non-zero components. The third and the forth eigenvalues are negative when ε and β satisfy $\varepsilon < \min\{(2+\beta)/(1+\beta), -(\beta+1)(\beta+2)\}$. The region of the (β, ε) plane in which these inequalities hold is shown in figure 3-1 between the blue and the green curve. An example of edge equilibrium $(v_{12}, v_{23}, 0, 0)$ can be seen in figure 3-3(b)). The blue curve is $\varepsilon = -(\beta+1)(\beta+2)$, and the green solid curve is $\varepsilon = (2+\beta)/(1+\beta)$.

In the region between the purple line and the blue (or green) curves (assuming $\beta < -1$ and $\varepsilon < 0$), there exists a heteroclinic 'face cycle' $\{v_{12}, v_{23}, v_{34}, v_{41}\}$ in the system (see in figure 3-4(b)). The cycle is only stable when $\varepsilon < (\beta+2)^2/\beta$, which is indicated by the sub-region between the yellow curve $\varepsilon = (\beta+2)^2/\beta$ and the blue (or green) curve in figure 3-1. The mathematical detail of the dynamics here will be discussed further, later.

Vertex equilibria.

For the equilibrium $v_1 := (1, 0, 0, 0)$, the Jacobian matrix is:

$$\begin{pmatrix} 0 & -1 & -\varepsilon & \beta+1 \\ 0 & 1 & 0 & 0 \\ 0 & 0 & \varepsilon & 0 \\ 0 & 0 & 0 & -\beta-1 \end{pmatrix}. \tag{3.22}$$

Note that the Jacobian matrix evaluated at the equilibrium v_2, v_3, v_4 are related by symmetry to $\boldsymbol{J}(v_1)$ and have the same eigenvalues. The points v_1, v_2, v_3, v_4 are therefore never stable states, but are connected to each other by heteroclinic orbits that form a heteroclinic 'edge cycle' (see figure 3-4(a)). This cycle exists when $\beta > -1, \varepsilon < 0$ and

is stable when $\beta > 0, \varepsilon < 0$. The mathematical details of this will be discussed in the next subsection.

3.2 Heteroclinic Cycles

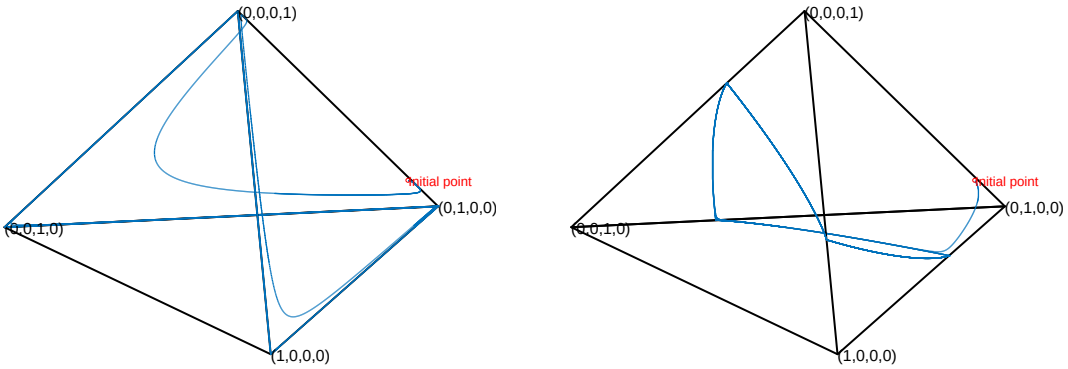

(a) Edge Cycles. (b) Face Cycles.

Figure(图) 3-4: Numerical examples of the two kinds of both heteroclinic cycle. The blue lines are data from the numerical integration of the ODEs (3.3). (a) $\beta = 0.5$, $\varepsilon = -0.1$. The cycle is formed by connecting the vertices v_1, v_2, v_3 and v_4. We call it the 'edge cycle' because it follows the edge of the convex polygon. (b) $\beta = -1.5$, $\varepsilon = -0.2$. The cycle is formed by connecting the vertices v_{12}, v_{23}, v_{34} and v_{41}. It is called 'face cycle' because the connecting orbits lie within faces of the tetrahedron.

In the previous subsection, we have investigated the stability of different kinds of equilibrium and found that most of them are stable when $\varepsilon > 0$, which corresponds to the first and second quadrants in figure 3-1. In this section, we will focus on the case $\varepsilon < 0$ (the third and fourth quadrant in figure 3-1). There are two possible kinds of heteroclinic cycle that form, connecting equilibria. The cycle formed by connections between the four vertices of the tetrahedron $\{v_1, v_2, v_3, v_4\}$ is called the 'edge cycle' because its connecting orbits follow edges of the tetrahedron. The cycle formed by connections between the four edge equilibria $\{v_{12}, v_{23}, v_{34}, v_{41}\}$ is called the 'face cycle' because its connecting orbits lie in faces if the tetrahedron, but not on edges. These two kinds of cycle are illustrated in figure 3-4.

3.2.1 Stability of Cycles

Edge cycle.

As can be seen from the Jacobian matrix (3.22), for the point $v_1 = (1, 0, 0, 0)$ we have four eigenvalues $\{0, 1, \varepsilon, -\beta - 1\}$. There exists an edge heteroclinic cycle when

$\varepsilon < 0$ and $\beta > -1$, so that v_1 has only a single unstable direction. We follow the standard definitions for robust heteroclinic cycles, see for example the book by Chossat and Lauterbach [7] and the papers by Krupa [35] and Krupa and Melbource [36]. Since the observed order of visiting neighbourhoods of the equilibria is $v_1 \to v_2 \to v_3 \to v_4 \to v_1 \to \cdots$ we label the v_2 direction (at v_1) 'expanding' and the v_4 direction (at v_1) 'connecting'. Then the expanding eigenvalue is $e = 1$ and the contracting eigenvalue is $-c = -\beta - 1$ here. Classic results in the literature, see the references above, show that if $c/e > 1$ the heteroclinic cycle is stable. Figure 3-5 shows numerical simulation near the edge cycle.

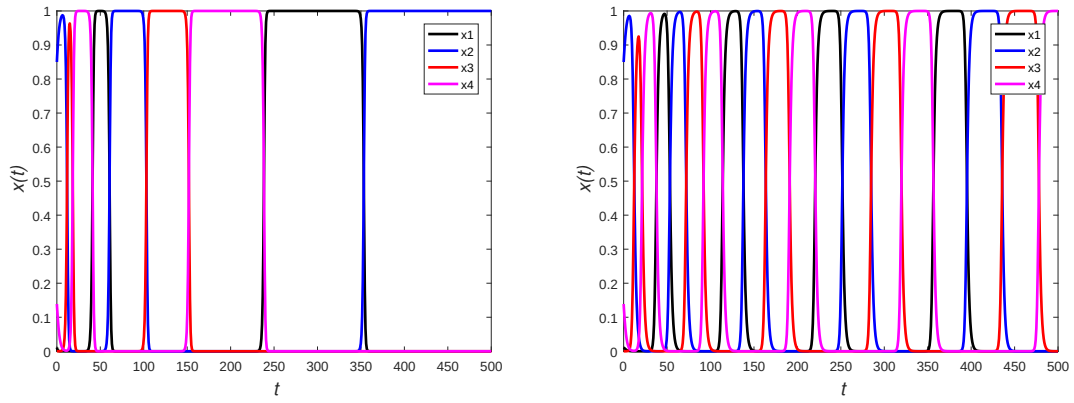

(a) Stable edge cycle.

(b) Unstable edge cycle.

Figure(图) 3-5: These figures show oscillations in the dynamics, near the 'edge cycles'. (a) $\beta = 0.5, \varepsilon = -0.5$; (b) $\beta = -0.5, \varepsilon = -0.5$. The edge cycle exists in both cases, since $\varepsilon < 0$ and $\beta > -1$. The four species proportions are represented by $\{x_1, x_2, x_3, x_4\}$. All the data is from the numerical simulations of the ODEs (3.3).

In figure 3-5(a) the trajectory spends increasingly long times near each saddle point v_j before moving rapidly to the neightbourhood of the next one. The trajectory becomes closer to the heteroclinic cycles as $t \to \infty$. In figure 3-5(b) the trajectory settles to a periodic oscillation close to, but not at, the edge cycle. This case is valid when $-1 < \beta < 0$, the edge cycle is unstable.

Face cycle.

Similar to the 'edge cycle', we find that the 'face cycle' exists when its four eigenvalues of the Jacobian matrix of points $\{v_{12}, v_{23}, v_{34}, v_{41}\}$ have two radial eigenvalues $-r_1, -r_2$ $(r_1, r_2 > 0)$, a expanding eigenvalue $e > 0$ and a contracting eigenvalue $-c$ $(c > 0)$. The model is cyclicly symmetric, so we pick $v_{12} = ((1+\beta)/\beta, -1/\beta, 0, 0)$ as an example. The point exists when $\beta < -1$ since we must keep $0 < x_1, x_2 < 1$. As

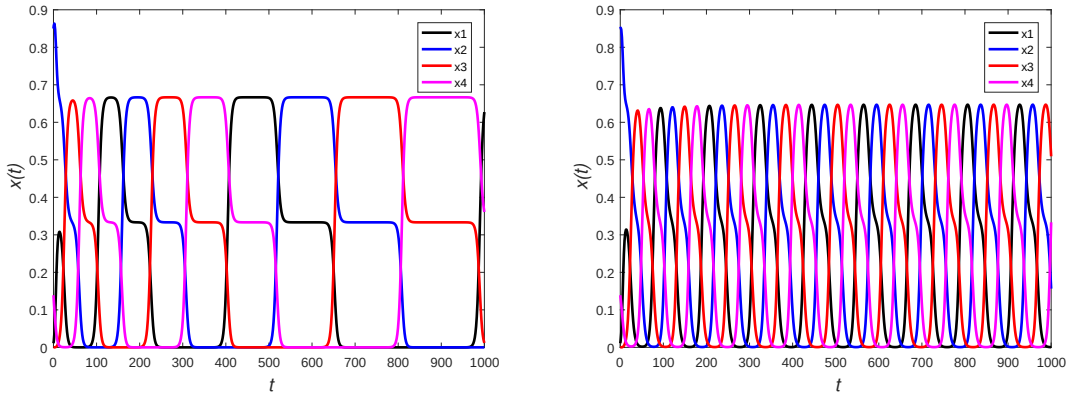

(a) Stable face cycle.

(b) Unstable face cycle.

Figure(图) 3-6: These figures show the oscillation in the dynamics, known as the 'face cycles'. Four species proportion is represented as $\{x_1, x_2, x_3, x_4\}$. All the data is from the numerical result of ODEs (3.3). The cycle is stable when $\varepsilon < (\beta+2)^2/\beta$, specifically $\beta = -1.5, \varepsilon < -1/6$. (a) $\beta = -1.5$, $\varepsilon = -0.2$. (b) $\beta = -1.5$, $\varepsilon = -0.1$.

shown by matrix (3.21), the eigenvalues are $\{-\frac{\beta+1}{\beta}, -\frac{\beta+1}{\beta}, \frac{\beta(\varepsilon-1)+\varepsilon-2}{\beta}, -\frac{\beta^2+3\beta+\varepsilon+2}{\beta}\}$. If we define $e := \frac{\beta(\varepsilon-1)+\varepsilon-2}{\beta}$ and $c := \frac{\beta^2+3\beta+\varepsilon+2}{\beta}$, the inequalities $e > 0$ and $c > 0$ imply $\varepsilon > (2+\beta)/(1+\beta)$ and $\beta > -2$, which is the region between the green curve and the purple line when $-2 < \beta < -1$ in figure 3-1. If we define $e := -\frac{\beta^2+3\beta+\varepsilon+2}{\beta}$ and $c := -\frac{\beta(\varepsilon-1)+\varepsilon-2}{\beta}$, similarly we get $\varepsilon > -(\beta+1)(\beta+2)$ and $\beta < -2$, which corresponds to the region between the blue curve and the purple line when $\beta < -2$ in figure 3-1. These two kinds of face cycle differ in the ordering of the vertices along the cycle.

As in the case of the edge cycle, the face cycle may be stable or unstable. In the region where the face cycle is stable, trajectories slow down as the approach neighbourhoods of the saddle points, see figure 3-6(a). When the face cycle is unstable, a stable periodic orbit exists close to it, as illustrated in figure 3-6(b). The curve $\varepsilon = (\beta+2)^2/\beta$ is the yellow curve in figure 3-1. It divides the existence region of 'face cycle' into two parts.

Since the face cycles have no counterpart in chapter 2, we focus on them here. We have found the corresponding reactions of ODEs (3.3) with the technique used in section 2.1.2, next we pick the specific value of $\beta = -1.5$, to study the relation between the period of oscillations and the parameter ε. We choose this value of β because at this point a face cycle occurs and with different value of ε, the stability is changed. The critical value $\varepsilon = -1/6$ of its stability is determined by the yellow curve for $c/e = 1$ in diagram figure 3-1. By local and global maps, we investigate the dependence of the oscillation period, denoted by T as we vary ε. Finally, we compare simulations of the chemical reactions with our theoretical analysis.

3.2.2 Maps of Cycles

In this subsection we analyse the dynamics near the face cycle using 'Poincare' return maps composed of local maps near each equilibrium point and global maps between them. The ODEs for $\{x_1(t), \ldots, x_4(t)\}$ are as derived previously in the infinite-population limit:

$$\dot{x}_1 = x_1\left[x_4 - (1+\beta)x_2 + \varepsilon x_3 + \beta X) - 2\varepsilon(x_1x_3 + x_2x_4)\right] + \mu(x_2 + x_3 + x_4 - 3x_1)\,, \quad (3.23)$$

from which the other three equations can be deduced by cyclically permuting the indices. Note that $\mu \geq 0$ is the mutation rate. If μ vanishes then the subsets of the phase space given by setting coordinates equal to zero (in any combination) are invariant for the dynamics. If $\mu > 0$ then they are no longer invariant.

We have analysed the equilibrium points when $\mu = 0$ by setting two of the coordinates to be zero (without loss of generality we set $x_3^* = x_4^* = 0$). The equilibrium point $x_1^* = (1+\beta)/\beta$, $x_2^* = -1/\beta$ exists as long as $\beta \leq -1$ (since all coordinates are non-negative).

Looking near this equilibrium point we define

$$x_1 = \frac{1+\beta}{\beta} + u_1, \qquad x_2 = -\frac{1}{\beta} + u_2\,,$$

where we consider $0 < u_1, u_2 \ll 1$ and we linearise in these variables and in x_3 and x_4 (which are also small). Keeping only the linear terms we obtain

$$\begin{aligned}
\dot{u}_1 =& \frac{1+\beta}{\beta}\left[-(\varepsilon + 1 + \frac{2\varepsilon}{\beta})x_3 - u_1 + x_4\left(2 + \beta + \frac{2\varepsilon}{\beta}\right)\right] \\
&+ \mu\left(u_2 + x_3 + x_4 - 3u_1 - 3 - \frac{4}{\beta}\right)\,, \\
\dot{u}_2 =& -\frac{1}{\beta}\left(-(2+\beta)x_3 + (1+\varepsilon+\beta)x_4 + (1+\beta)u_2 - 2\varepsilon\frac{1+\beta}{\beta}x_3 + 2\frac{\varepsilon}{\beta}x_4\right) \\
&+ \mu\left(1 + \frac{4}{\beta} + u_1 + x_3 + x_4 - 3u_2\right)\,, \\
\dot{x}_3 =& x_3\left(\frac{\varepsilon(1+\beta) - (2+\beta)}{\beta}\right) + \mu(1 + u_1 + u_2 + x_4 - 3x_3)\,, \\
\dot{x}_4 =& -x_4\left(\frac{\varepsilon + (1+\beta)(2+\beta)}{\beta}\right) + \mu(1 + u_1 + u_2 + x_3 - 3x_4)\,.
\end{aligned} \quad (3.24)$$

The x_3 and x_4 equations together describe the evolution of trajectories close to the equilibrium point and are valid even when $\mu > 0$. We write these in the more compact form, assuming μ is small and dropping terms where μ is multiplied by any

of the coordinate variables (which are also small).

$$\begin{aligned} \dot{x}_3 &= e x_3 + \mu\,, \\ \dot{x}_4 &= -c x_4 + \mu\,, \end{aligned} \tag{3.25}$$

where we set $\beta = -1.5$, so the contracting eigenvalue is $-c$ where $c := \frac{\varepsilon+(1+\beta)(2+\beta)}{\beta} = (1-4\varepsilon)/6 > 0$ and the expanding eigenvalue $e := \frac{\varepsilon(1+\beta)-(2+\beta)}{\beta} = (\varepsilon+1)/3 > 0$ in the range of ε that we consider, i.e. $-1 < \varepsilon < 0$ (see the range in figure 3-1 for $\beta = -1.5$).

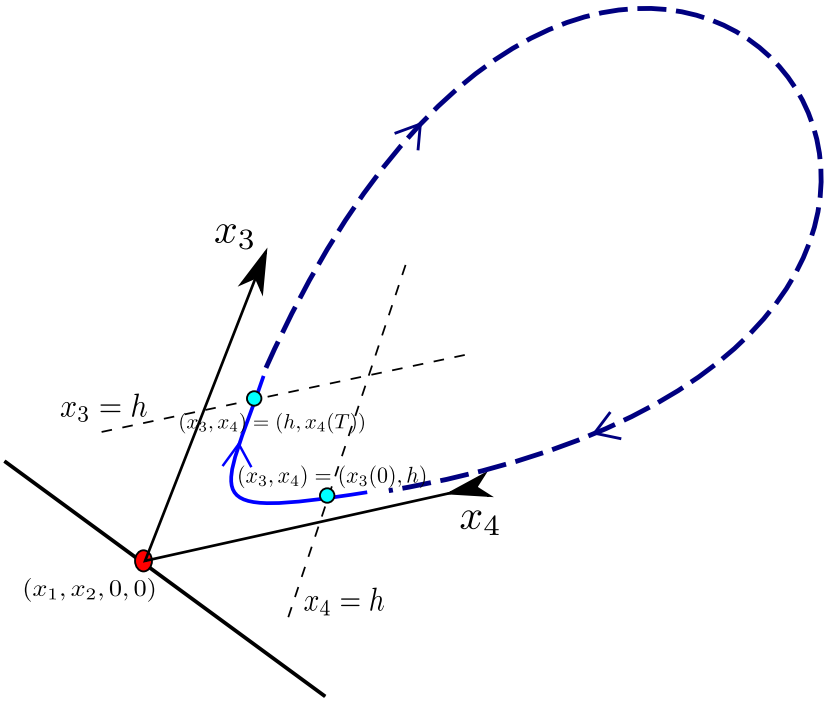

Figure(图) 3-7: A sketch of the local and global maps near v_{12}. The light blue solid line is the local map in a small box-shaped region near the point $v_{12} = (1+1/\beta, -1/\beta, 0, 0)$. The dark blue dashed line indicates other global and local maps before the trajectory returns to near v_{12} again.

We now consider integrating the x_3 and x_4 equations from the point $(x_3, x_4) = (x_3(0), h)$ at time $t = 0$ to the point $(h, x_4(T))$ at time $t = T$, where h is a fixed parameter that describes the location of the relevant hyperplanes between which we integrate (3.25) (see figure 3-7). The local integrations result in

$$\begin{aligned} x_4(T) - \mu/c &= (h - \mu/c)\exp(-cT), \\ h + \mu/e &= (x_3(0) + \mu/e)\exp(eT). \end{aligned} \tag{3.26}$$

In the case $\mu = 0$ the global map is given to leading order by multiplication by a

constant factor, due to the invariance of the coordinate hyperplanes. We assume that even when μ is small and positive this is still a valid assumption and the form of the map would vary only through the addition of $O(\mu)$ correction terms.

From the second equation (3.26) we can write the integration time T as

$$T = \frac{1}{e} \log \left(\frac{h + \mu/e}{x_3(0) + \mu/e} \right) , \tag{3.27}$$

and hence we can eliminate T between the two equations above, to give the relation between $x_3(0)$ and $x_4(T)$ on the $(n+1)^{th}$ time the trajectory passes near this equilibrium point:

$$\frac{x_4^{(n+1)}(T) - \mu/c}{h - \mu/c} = \left(\frac{x_3^{(n+1)}(0) + \mu/e}{h + \mu/e} \right)^{c/e} . \tag{3.28}$$

Now we consider the global map from $x_4^{(n)}(T)$ to $x_3^{(n+1)}(0)$. When $\mu = 0$ this is expected to be just multiplication by a scalar at leading order. When $\mu > 0$ the global map should probably also contain a factor of μ; when composed with the local map this factor of μ is expected only to make a small contribution. So for the global map we write

$$x_3^{(n+1)}(0) = K x_4^{(n)}(T) , \tag{3.29}$$

where $K > 0$ is a constant. Composing the global and local maps results in the map for $x_n := x_4^{(n)}(0)$ given by

$$\frac{x_{n+1} - \mu/c}{h - \mu/c} = \left(\frac{K x_n + \mu/e}{h + \mu/e} \right)^{c/e} \tag{3.30}$$

Note that the eigenvalue parameters c and e are determined as functions of ε and β, but the parameters h and K are an determined but should not depend, at least to leading order on μ, ε, or β. We verify the form of the map (3.30) against numerical simulations. Since we expect that if $\mu N \gg 1$ the ODEs are in good agreement with stochastic simulation results, we run stochastic simulation for $N = 3 \times 10^5$, and $\mu = 10^{-4}$, see figure 3-8. We fit the result of iterating the map (3.30), setting $K = 0.12$ and $h = 0.9$ which yields the lower blue dashed curve in figure 3-8. Then without changing values of K and h but only setting $N = 5 \times 10^5$ and $\mu = 10^{-5}$ we now compare theory and numerical simulations again. This results in the upper pair of curves in figure 3-8, showing that the form of the map has validity over a range of μ values.

When ε tends to -1 the expanding eigenvalue e tends to zero, indicating that a local bifurcation takes place at v_{12}. The period of stochastic oscillations also becomes very large as $\varepsilon \to -1$, as shown in figure 3-9. This increase is not captured so well

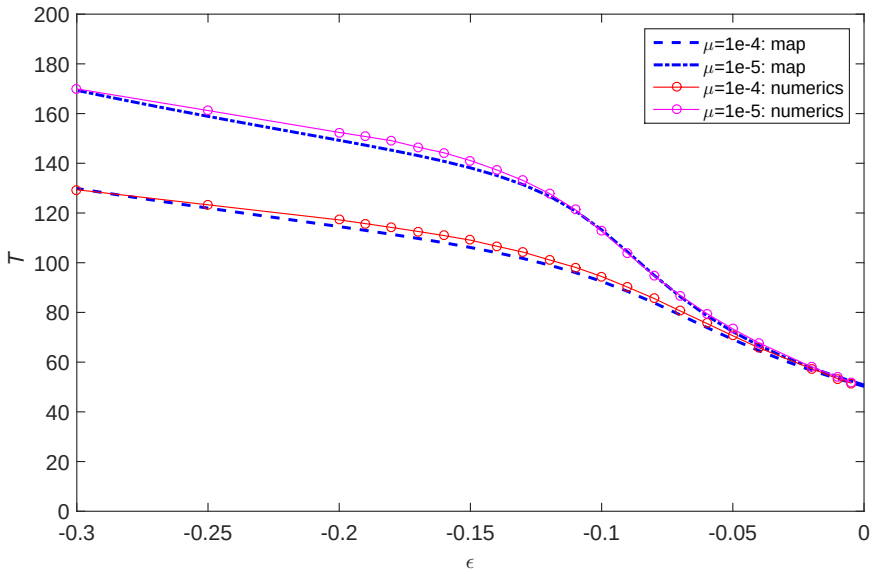

Figure(图) 3-8: Comparison between iterating map results and stochastic simulations by setting $x_0 = 0.001$, $K = 0.12$ and $h = 0.9$. Lower: $\mu = 10^{-4}$ and $N = 3 \times 10^5$. Upper: $\mu = 10^{-5}$ and $N = 5 \times 10^5$. The dashed 'map' curves illustrate equation (3.30) and (3.27). The dot curves are the simulation data which comes from Gillespie simulations: we record the first time that x_1, x_2, x_3, x_4 increase and jump over 0.25, and iterate 1000 times. The dots are the mean value of the last 800 cycles.

by the map (3.30); future work could consider adjustments to (3.30) to improve it near $\varepsilon = -1$. When μN is not so large, the mean period of stochastic oscillations increases for all $-1 < \varepsilon < 0$. These results are qualitatively in line with chapter 2 where the increase in stochasticity increased the mean period for above the mean-field ODE prediction.

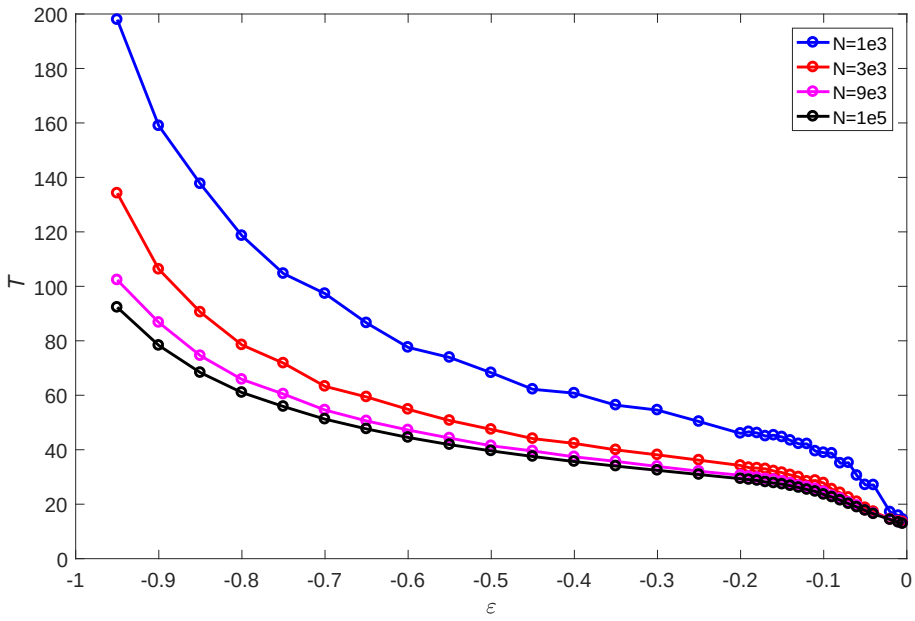

Figure(图) 3-9: Mean period of face cycles of stochastic simulations of chemical reactions when $\mu = 10^{-4}$, $\beta = -1.5$ with different size of population. The dot curves are the simulation data which comes from Gillespie simulations: we record the first time that x_1, x_2, x_3, x_4 increase and jump over 0.25, and iterate 1000 times. The dots are the mean value of the last 800 cycles. More simulation points of the parameter ε are taken near $\varepsilon_c = -1/6$ (which is given by the yellow cure for $c/e = 1$ in diagram figure 3-1), because we are interested in the 'turning' around the critical value.

Chapter 4

Interactions between Species and Complex Environment 种群竞争与环境互动

In the previous discussion, we pay most attention to the interactions (such as cyclic dominance and mutation) in some (3 or 4) species. We establish the corresponding equations, analyse the evolution of species in the population level and the stochastic oscillations in the individual level. However, these models and equations are fully specified, and assumed to be essentially isolated from their environment. The species, named as 'A', 'B', 'C' or 'D' only interact with each other, never communicate with others. For real-world systems such a clean separation is simply not possible. In ecology, for example, the interactions of a few species of interest are complicated by fluctuations in the wider ecosystem of which they are part.

In this chapter, we start to consider the communication between these main species and other species which live in the surrounding area. This kind of interaction might be much weaker than the internal cyclic competitions among the previous species, but the effects from the surroundings should not be ignored.

We study this case to understand if and how the environment affects the dynamics of the small species set which we are interested in.

4.1 An Isolated 'Island'

First of all, we should establish a model to describe the surrounding complicated environment. By assuming the existence of thousands species on an 'island', we believe that there are many interactions among these species. So we begin by introducing a

model of a general autocatalytic reaction networks.

4.1.1 Model

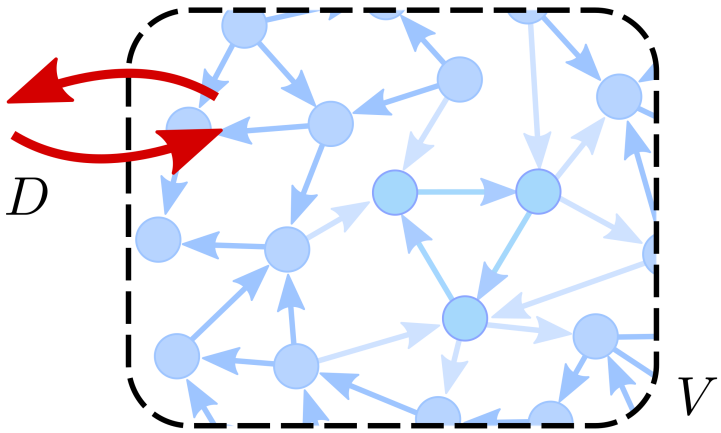

Figure(图) 4-1: Illustration of the environment: an autocatalytic network in a volume V, with dynamics damped by diffusion of strength D. The blue circle points represent a species. The blue arrow from a species to another one means the competition: one beats another one.

Fig.4-1 shows an example of the possible environment. We consider a biochemical reaction network composed of N chemical 'types' (equivalently representing animal species), labelled $\{X_i\}_{i=1}^N$. Reactions take place in a compartment of large but finite volume $V \gg 1$ (for example an isolated island). Molecules enter and leave the compartment with rate $D \ll 1$, and engage in two-body reactions (like the competitive interactions between different species) of the autocatalytic form $X_i + X_j \to 2X_j$, with rate constants r_{ij} encoded in an interaction matrix $\boldsymbol{R}$. According to method in the section 1.3.1, the payoff matrix of the two-body interactions is then given by $\boldsymbol{P} = \boldsymbol{R}^T - \boldsymbol{R}$. From equation (1.1) we obtain ODEs to describe the dynamics:

$$\dot{x}_i = x_i \sum_j (r_{ji} - r_{ij}) x_j + D(1 - x_i). \tag{4.1}$$

Here, to obtain the equilibrium quickly, we consider the particular case in which the reaction network obeys Kirchoff's first law: for all i we have $\sum_j r_{ij} = \sum_j r_{ji}$. This assumption gives us the equilibrium $\boldsymbol{x} = (1, ..., 1)$. This is a technical assumption whose purpose is to simplify the analsis. Solving for the equilibrium is not our key interest here; the main features of our research results apply more widely in other cases

with different equilibria. Also note that, the rate of influx of particles D has same function with the mutation rate μ in chapter 2 and chapter 3: to make the equilibrium stable.

For clarity of exposition, we choose the model so as to ensure that the deterministic dynamics for chemical concentrations derived in the infinite-volume limit has a globally attractive equilibrium state. The eigenvalues of the Jacobian around this state all have negative real part, implying stability, while any imaginary part of the spectrum gives rise to damped oscillations as the system relaxes to equilibrium. In finite volumes intrinsic noise excites the system and induces sustained stochastic oscillations [48, 59], such as those in figure 2-3.

Write x_i for the concentration of chemical species i, and $\boldsymbol{x}$ for the column-vector of all concentrations, specifying the system state. Following the standard techniques described in sections 1.3.3 and 1.3.2, for large V the dynamics of the autocatalytic networks the chemical concentrations obey the SDEs:

$$\dot{x}_i = x_i \sum_j (r_{ji} - r_{ij}) x_j + D(1 - x_i) + \frac{1}{\sqrt{V}} \eta_i(t) \,. \tag{4.2}$$

The noise $\eta_i(t)$ here is Gaussian with correlator $\langle \eta_i(t), \eta_j(t') \rangle = \delta(t - t')[\delta_{ij} x_i((\boldsymbol{R} + \boldsymbol{R}^T)\boldsymbol{x})_i - \boldsymbol{x}^T(\boldsymbol{R} + \boldsymbol{R}^T)\boldsymbol{x}]$.

In the limit $V \to 0$ the system becomes deterministic, and it is straightforward to observe that the homogeneous state $x_i \equiv 1$ is a stable equilibrium, with Jacobian matrix $\boldsymbol{A} = \boldsymbol{R}^T - \boldsymbol{R} - D\boldsymbol{I}$. The equilibrium is globally attractive, meaning relaxation to homogeneity is the only possible deterministic dynamical behaviour. In a finite volume, however, intrinsic noise radically alters this behaviour, which is similar to the case discussed in the symmetric RPS model in the section 2.1.1. Similarly, linearising around the stable equilibrium we obtain the linearised SDEs:

$$\mathrm{d}\boldsymbol{x} = \boldsymbol{A}\boldsymbol{x}\mathrm{d}t + \frac{1}{\sqrt{V}} \boldsymbol{M}\mathrm{d}\boldsymbol{W}(t) \tag{4.3}$$

driven by Gaussian noise that is delta-correlated in time and has $\boldsymbol{M}\boldsymbol{M}^T = \boldsymbol{B}$ where B has entries $\boldsymbol{B}_{ij} = \delta_{i,j} \sum_k (\boldsymbol{R}_{ik} + \boldsymbol{R}_{ki}) - (\boldsymbol{R}_{ij} + \boldsymbol{R}_{ji})$.

Following the technique in 1.3.4, the stochastic oscillations of the chemical concentration here are captured by the power spectral density of $\boldsymbol{x}$, given by the matrix coefficients $\boldsymbol{A}$ and $\boldsymbol{B}$ derived for this model:

$$\boldsymbol{\mathcal{P}}(\omega) = \frac{1}{2\pi} (\boldsymbol{A} - \mathrm{i}\omega\boldsymbol{I})^{-1} \boldsymbol{B} (\boldsymbol{A} - \mathrm{i}\omega\boldsymbol{I})^{-\dagger}. \tag{4.4}$$

Here the equation (4.4) is the general form of PSD for stochastic oscillations; only the

form of the matrices $\boldsymbol{A}$ and $\boldsymbol{B}$ are model–specific.

4.1.2 Analysis of Oscillations

Lacking specific knowledge of the 'island' interaction network, we propose to consider a random autocatalytic network. Following algorithm 1.2, we can generate a random matrix using parameters N, M, c, μ_1 and μ_2. Recall that N is the number of species which are involved, M is the total number of reactions, c is the mean number of reactions per chemical species, and μ_1 and μ_2 are the first and second moment of reaction rate distribution, just as defined previously in section 1.3.5. We choose the distribution of the elements of the random matrix to be 'lognormal' or 'exponential' to satisfy the nonnegative rate condition, of course other choices are possible. This matrix is the reaction matrix $\boldsymbol{R}$ defined in section 4.1.1. Technically, it is not possible to choose fully IID reaction rates as we have previously imposed Kirchoff's law, which implies a correlation between rates. However, we find these correlations are negligible for even moderate values of N and c, so the algorithm 1.2 is suitable here.

After generating a random matrix $\boldsymbol{R}$ which satisfies all the above rules, we obtain the simplest possible description of an autocatalytic reaction network on an 'island'. From equation (4.4) for the PSD it may appear that the power spectral density of the environment network depends in detail on the configuration of the rate matrix. However, it can be shown that this is not the case: in the limit of large N and c, all chemical species in the network exhibit the same universal quarter-circle power spectrum, which depends only on the parameters D, c, μ_1 and μ_2. The quarter-circle power spectrum is a variant of Wigner semicircle distribution [73], whose graph of its probability density function is a semi-circle of radius R centered at $(0, 0)$.

Calculation of $\boldsymbol{\mathcal{P}}(\omega)$

Given the reaction rate matrix $\boldsymbol{R}$, it is straightforward to compute the coefficient matrices $\boldsymbol{A}$ and $\boldsymbol{B}$ in the PSD equation (4.4). $\boldsymbol{A}$ and $\boldsymbol{B}$ are, however, high-dimensional, and random, so direct calculations are almost impossible. We will instead apply the 'cavity method' to solve the problem.

The cavity method was invented to analyse the spin glass model of Sherrington and Kirkpatrick [55, 49], by exploiting the graph structure of that model. More generally, it can be used for any system in which a calculation may be broken down into contributions from the sites and bonds of an underlying network structure. In particular, in [73, 72] the method was adapted to study the distribution of eigenvalues of random matrices, via an analogy between Gaussian integrals and spin systems. Here we follow similar lines and use the cavity method without considering its physical background.

First of all, as $\boldsymbol{\mathcal{P}}$ is Hermitian, it can be expressed as a complex Gaussian integral. With this interpretation, $\boldsymbol{\mathcal{P}}$ can be transformed into the form of partition function. In following part, we first introduce three forms of Gaussian integral. They help us to represent $\boldsymbol{\mathcal{P}}$ as an exponential integral.

Theorem 4.1 (Gaussian integral)**.** *If $\boldsymbol{\Gamma}$ is an $N \times N$ Hermitian matrix, $\boldsymbol{z}, \boldsymbol{\mu} \in \mathbb{C}^N$ are column vectors, we have*

$$\frac{1}{\pi^N det(\boldsymbol{\Gamma})} \int_{\mathbb{C}^N} e^{-(\boldsymbol{z}-\boldsymbol{\mu})^\dagger \boldsymbol{\Gamma}^{-1}(\boldsymbol{z}-\boldsymbol{\mu})} \mathrm{d}\boldsymbol{z} = 1 \tag{4.5}$$

$$\frac{1}{\pi^N det(\boldsymbol{\Gamma})} \int_{\mathbb{C}^N} e^{-(\boldsymbol{z}-\boldsymbol{\mu})^\dagger \boldsymbol{\Gamma}^{-1}(\boldsymbol{z}-\boldsymbol{\mu})} \boldsymbol{z}\boldsymbol{z}^\dagger \mathrm{d}\boldsymbol{z} = \boldsymbol{\Gamma} \tag{4.6}$$

$$\frac{1}{\pi^N det(\boldsymbol{\Gamma})} \int_{\mathbb{C}^N} e^{\{-(\tilde{\boldsymbol{z}}-\boldsymbol{\mu})^\dagger \boldsymbol{\Gamma}^{-1}(\tilde{\boldsymbol{z}}-\boldsymbol{\mu}) + \boldsymbol{u}^\dagger \tilde{\boldsymbol{z}} + \tilde{\boldsymbol{z}}^\dagger \boldsymbol{v}\}} \mathrm{d}\tilde{\boldsymbol{z}} = e^{\boldsymbol{u}^\dagger \boldsymbol{\Gamma} \boldsymbol{v}} \tag{4.7}$$

where $\boldsymbol{z}$ is an N–dimensional vector of complex variables with $z_i = x_i + \mathrm{i}y_i$ and we introduce the shorthand

$$\int_{\mathbb{C}^N} \mathrm{d}\boldsymbol{z} = \int_{\mathbb{C}} \cdots \int_{\mathbb{C}} \prod_{i=1}^{N} \mathrm{d}Rez_i \, \mathrm{d}Imz_i = \int_{\mathbb{C}} \cdots \int_{\mathbb{C}} \prod_{i=1}^{N} \mathrm{d}x_i \, \mathrm{d}y_i.$$

The first and second of these results follow since this is a normalised probability distribution, and the second moment is precisely Γ. The third equation, (4.7), is evaluated directly by writing real and imaginary parts of the vector and integrating them.

From equation (4.6), the PSD equation, by setting $\Gamma = \mathcal{P}(\omega)$ and observing that $\det(\mathcal{P}(\omega)) = |B|/|A - \mathrm{i}\omega \boldsymbol{I}|^2$ and ignoring the constant coefficient $(2\pi)^{-1}$, is transformed into:

$$\boldsymbol{\mathcal{P}}(\omega) = \frac{|\boldsymbol{A} - \mathrm{i}\omega \boldsymbol{I}|^2}{\pi^N |\boldsymbol{B}|} \int_{\mathbb{C}^N} e^{-\boldsymbol{z}^\dagger (\boldsymbol{A} - \mathrm{i}\omega \boldsymbol{I})^\dagger \boldsymbol{B}^{-1} (\boldsymbol{A} - \mathrm{i}\omega \boldsymbol{I}) \boldsymbol{z}} \boldsymbol{z}\boldsymbol{z}^\dagger \mathrm{d}\boldsymbol{z} \, . \tag{4.8}$$

There is still an inverse matrix $\boldsymbol{B}^{-1}$ in (4.8), which is difficult to calculate. With equation (4.7), we set the terms

$$\Gamma = \boldsymbol{B}^{-1}, \quad \boldsymbol{u}^\dagger = -\boldsymbol{z}^\dagger (\boldsymbol{A} - \mathrm{i}\omega \boldsymbol{I})^\dagger, \quad \boldsymbol{v} = (\boldsymbol{A} - \mathrm{i}\omega \boldsymbol{I}) \boldsymbol{z} \, , \tag{4.9}$$

then we may rewrite (4.8) as

$$\boldsymbol{\mathcal{P}}(\omega) = \frac{|\boldsymbol{A} - \mathrm{i}\omega|^2}{\pi^{2N}} \int_{\mathbb{C}^N} \boldsymbol{z}\boldsymbol{z}^\dagger \mathrm{d}\boldsymbol{z} \int_{\mathbb{C}^N} e^{-\mathcal{H}(\boldsymbol{z}, \tilde{\boldsymbol{z}})} \mathrm{d}\tilde{\boldsymbol{z}} \, , \tag{4.10}$$

where

$$\mathcal{H}(\boldsymbol{z}, \tilde{\boldsymbol{z}}) := \boldsymbol{z}^\dagger(\boldsymbol{A} - \mathrm{i}\omega\boldsymbol{I})^\dagger\tilde{\boldsymbol{z}} - \tilde{\boldsymbol{z}}^\dagger(\boldsymbol{A} - \mathrm{i}\omega\boldsymbol{I})\boldsymbol{z} + \tilde{\boldsymbol{z}}^\dagger\boldsymbol{B}\tilde{\boldsymbol{z}}\,. \tag{4.11}$$

This expression is more simple because matrices are not in a product, and $\boldsymbol{B}$ is not inverted. The technique of achieving such a simplification by introducing additional integration variables originates in statistical physics and is known as a Hubbard-Stratonovich transformation [28]. We choose the notation $\mathcal{H}(\boldsymbol{z}, \tilde{\boldsymbol{z}})$ to imply an analogy between this integral and partition function of a spin system with 'Hamiltonian' given by (4.11).

The approach named as cavity method has been discussed in section 1.3.5. Equation (4.10) now has similar form with equation (1.51), which is friendly to cavity method. Our approach here is to treat ω as a parameter (in the following we drop the explicit dependence from the notation), and consider the integral (4.8) as something akin to the computation of the covariance matrix of a system of complex-valued spins with quenched disorder. This technique has a long tradition in random matrix theory [17, 71, 50, 74, 38, 73], where the statistical mechanics analogy allows one to import a powerful set of techniques developed in that field.

What we are really interested in is the diagonal terms of $\boldsymbol{\mathcal{P}}(\omega)$, which shows frequency distribution of time series $x_i(t)$. In the setting based on a spin system, we have $\boldsymbol{\mathcal{P}}_{ii} = \langle|z_i|^2\rangle$ where angle brackets refer to integrating against the complex density (which is different from the definition in chapter 1 in that it is not a probability measure, but the method remain the same)

$$F(\boldsymbol{z}, \tilde{\boldsymbol{z}}) = \mathcal{Z}^{-1}e^{-\mathcal{H}(\boldsymbol{z},\tilde{\boldsymbol{z}})}\,, \tag{4.12}$$

with $\mathcal{Z} = \pi^{2N}/|\boldsymbol{A} - \mathrm{i}\omega|^2$, i.e.

$$\boldsymbol{\mathcal{P}}_{ii} = \int_{\mathbb{C}} |z_i|^2 \mathrm{d}z_i \int_{\mathbb{C}} F(\boldsymbol{z}, \tilde{\boldsymbol{z}})\mathrm{d}\tilde{\boldsymbol{z}}\,. \tag{4.13}$$

Now the interactions between spins in the Hamiltonian (4.11) map directly to those of the underlying chemical reaction network. In particular, in analogy with (1.48) we can split the Hamiltonian into site and bond contributions:

$$\mathcal{H} = \sum_i \mathcal{H}_i + \sum_{i\sim j} \mathcal{H}_{ij}\,, \tag{4.14}$$

where we write $i \sim j$ to denote the event that species i and j are involved in a reaction together. With compound spins $\boldsymbol{\varphi}_i = (z_i, \tilde{z}_i)^T$ each part in the Hamiltonian (4.14) can

be written in a compact form:

$$\begin{aligned} \mathcal{H}_i &= \boldsymbol{\varphi}_i^\dagger \boldsymbol{Q}_i \boldsymbol{\varphi}_i \,, \\ \mathcal{H}_{ij} &= \boldsymbol{\varphi}_i^\dagger \boldsymbol{Q}_{ij} \boldsymbol{\varphi}_j \,, \end{aligned} \tag{4.15}$$

with transfer matrices

$$\begin{aligned} \boldsymbol{Q}_i &= \begin{pmatrix} 0 & \boldsymbol{A}_{ii} + \mathrm{i}\omega \\ -\boldsymbol{A}_{ii} + \mathrm{i}\omega & \boldsymbol{B}_{ii} \end{pmatrix} = \begin{pmatrix} 0 & -D + \mathrm{i}\omega \\ D + \mathrm{i}\omega & \sum_k (R_{ik} + R_{ki}) \end{pmatrix} , \\ \boldsymbol{Q}_{ij} &= \begin{pmatrix} 0 & \boldsymbol{A}_{ji} \\ -\boldsymbol{A}_{ij} & \boldsymbol{B}_{ij} \end{pmatrix} = \begin{pmatrix} 0 & R_{ij} - R_{ji} \\ R_{ij} - R_{ji} & -R_{ij} - R_{ji} \end{pmatrix} . \end{aligned} \tag{4.16}$$

To obtain the power spectrum of species i it is necessary to compute the single-site covariance matrix $\boldsymbol{U}_i := \langle \boldsymbol{\varphi}_i \boldsymbol{\varphi}_i^\dagger \rangle$, from which $\boldsymbol{\mathcal{P}}_{ii}$ is obtained as the top left entry. Following the large connectivity limit of the cavity method in section 1.3.5, we write f_i for the marginal density at site i, obtained by integrating the density (4.12) over all other variables. Then the covariance matrix $\boldsymbol{U}_i$ can be expressed as:

$$\boldsymbol{U}_i = \int_{\mathbb{C}} \boldsymbol{\varphi}_i \boldsymbol{\varphi}_i^\dagger f_i(\boldsymbol{\varphi}_i) \mathrm{d}\boldsymbol{\varphi}_i \,. \tag{4.17}$$

Using (4.6), the matrix $\boldsymbol{U}_i$ is also transformed as:

$$\boldsymbol{U}_i = \frac{1}{\pi^2 \det \boldsymbol{U}_i} \int_{\mathbb{C}} \boldsymbol{\varphi}_i \boldsymbol{\varphi}_i^\dagger e^{-\boldsymbol{\varphi}_i^\dagger \boldsymbol{U}_i^{-1} \boldsymbol{\varphi}_i} \mathrm{d}\boldsymbol{\varphi}_i \,, \tag{4.18}$$

setting $\Gamma = \boldsymbol{U}_i$ and $\boldsymbol{z} = \varphi_i$ in (4.6). So by equating (4.17) and (4.18), we know that:

$$f_i(\boldsymbol{\varphi}_i) = \frac{1}{\pi^2 \det \boldsymbol{U}_i} e^{-\boldsymbol{\varphi}_i^\dagger \boldsymbol{U}_i^{-1} \boldsymbol{\varphi}_i} \,. \tag{4.19}$$

At the same time exploiting the sparsity of the reaction network we have the almost exact relation

$$f_i(\boldsymbol{\varphi}_i) \approx \frac{1}{\mathcal{Z}_i} e^{-\mathcal{H}_i} \int_{\mathbb{C}} \prod_{j \sim i} \left(e^{-\mathcal{H}_{ij} - \mathcal{H}_{ji}} f_j^{(i)}(\boldsymbol{\varphi}_j) \mathrm{d}\boldsymbol{\varphi}_j \right) , \tag{4.20}$$

where $f_j^{(i)}$ is the so-called cavity marginal, describing the single site density at j in the network with site i removed. The normalized coefficient is $\mathcal{Z}_i$. Introducing (4.19) into (4.20), parameterizing the site and cavity densities with 2×2 covariance matrices and

performing the integration in (4.20) yields

$$\begin{aligned} e^{-\boldsymbol{\varphi}_i^\dagger \boldsymbol{U}_i^{-1}\boldsymbol{\varphi}_i} &= \frac{1}{Z_i} e^{-\mathcal{H}_i} \int_{\mathbb{C}} \prod_{j\sim i} \left(e^{-\mathcal{H}_{ij}-\mathcal{H}_{ji}} e^{-\boldsymbol{\varphi}_j^\dagger \left(\boldsymbol{U}_j^{(i)}\right)^{-1}\boldsymbol{\varphi}_j} \mathrm{d}\boldsymbol{\varphi}_j \right) , \\ &= \frac{1}{Z_i} e^{-\boldsymbol{\varphi}_i^\dagger \boldsymbol{Q}_i \boldsymbol{\varphi}_i} \int_{\mathbb{C}} \prod_{j\sim i} \left(e^{-\boldsymbol{\varphi}_i^\dagger \boldsymbol{Q}_{ij}\boldsymbol{\varphi}_j - \boldsymbol{\varphi}_j^\dagger \boldsymbol{Q}_{ji}\boldsymbol{\varphi}_i} e^{-\boldsymbol{\varphi}_j^\dagger \left(\boldsymbol{U}_j^{(i)}\right)^{-1}\boldsymbol{\varphi}_j} \mathrm{d}\boldsymbol{\varphi}_j \right) , \\ &= \frac{1}{Z_i} e^{-\boldsymbol{\varphi}_i^\dagger \boldsymbol{Q}_i \boldsymbol{\varphi}_i} \prod_{j\sim i} e^{\left(-\boldsymbol{\varphi}_i^\dagger \boldsymbol{Q}_{ij}\right)\boldsymbol{U}_j^{(i)}(\boldsymbol{Q}_{ji}\boldsymbol{\varphi}_i)} , \\ &= e^{-\boldsymbol{\varphi}_i^\dagger \left(\boldsymbol{Q}_i - \sum_{j\sim i}\boldsymbol{Q}_{ij}\boldsymbol{U}_j^{(i)}\boldsymbol{Q}_{ji}\right)\boldsymbol{\varphi}_i} . \end{aligned} \tag{4.21}$$

The third equivalence is valid with the integration (4.7) in Theorem 4.1. Naturally the equation (4.21) could be simplified by taking logarithm to obtain

$$\boldsymbol{U}_i^{-1} = \boldsymbol{Q}_i - \sum_{j\sim i} \boldsymbol{Q}_{ij}\boldsymbol{U}_j^{(i)}\boldsymbol{Q}_{ji} . \tag{4.22}$$

Lacking any special structure imposed on the reaction network, we surmise that the sum over network neighbours is approximately self-averaging, which means that the network can be described by averaging over a sufficiently large sample [22]. To make progress we take the expectation of the right-hand side of (4.22) to solve the equation. We can deal it in this way because the cavity network here is highly-connected and correlation between vertices is small. In statistical physics, this technique is named the 'TAP approach' [79, 73]. We may thus replace both the site and cavity covariance matrices with the average matrix $\boldsymbol{U}$, then obtain a self-consistent equation to solve:

$$\boldsymbol{U}^{-1} = \mathbb{E}\left(\boldsymbol{Q}_i\right) - \mathbb{E}\left(\sum_{j\sim i} \boldsymbol{Q}_{ij}\boldsymbol{U}\boldsymbol{Q}_{ji} \right) . \tag{4.23}$$

We parameterise

$$\boldsymbol{U} = \begin{pmatrix} s & r \\ -\overline{r} & 0 \end{pmatrix} , \tag{4.24}$$

where $\langle |z|^2 \rangle = s \in \mathbb{R}^+$ and $\langle \overline{z}\tilde{z} \rangle = r \in \mathbb{C}$. Taking expectation over the quenched disorder of the reaction rates in (4.23) obtains

$$\begin{pmatrix} s & r \\ -\overline{r} & 0 \end{pmatrix}^{-1} = \begin{pmatrix} 0 & -D+\mathrm{i}\omega \\ D+\mathrm{i}\omega & c\mu_1 \end{pmatrix} + c\mu_2 \begin{pmatrix} 0 & -\overline{r} \\ r & s \end{pmatrix} . \tag{4.25}$$

The parameters D, μ_1, μ_2, c are defined in generating reaction matrix $\boldsymbol{R}$. By setting

$r = a + b\mathrm{i}(a, b \in \mathbb{R})$, we get two equations from (4.25):

$$\begin{cases} \frac{a-b\mathrm{i}}{a^2+b^2} &= (D + c\mu_2 a) + \mathrm{i}(\omega + c\mu_2 b) \\ \frac{s}{a^2+b^2} &= c\mu_1 + c\mu_2 s, \end{cases} \tag{4.26}$$

Rearranging the two equations by replacing term $a^2 + b^2$ with $s/(c\mu_1 + c\mu_2 s)$, we find that the cross-spectrum (r) can be written succinctly in terms of the spectrum (s),

$$r(\omega) = \frac{s}{c}\left(\frac{D}{\mu_1} - \mathrm{i}\frac{\omega}{\mu_1 + 2s\mu_2}\right). \tag{4.27}$$

Plugging this result into Eq. (4.26) and solving for s determines the mean power spectrum of oscillations for chemical species in the bulk random reaction network. By assuming the diffusion rate $D \ll 1$, we obtain the solution expanded in order of D:

$$\begin{cases} \text{When } 4c\mu_2 > \omega^2, & r(\omega) = \dfrac{\mathrm{i}\omega - \sqrt{4c\mu_2 - \omega^2}}{2c\mu_2} + \mathcal{O}(D)\,, \\ & s(\omega) = \dfrac{\mu_1\sqrt{4c\mu_2 - \omega^2}}{2D\mu_2} - \dfrac{\mu_1}{2\mu_2} + \mathcal{O}(D)\,, \\ \text{When } 4c\mu_2 < \omega^2, & r(\omega) = \dfrac{\mathrm{i}(\sqrt{\omega^2 - 4c\mu_2} - \omega)}{2c\mu_2} + \mathcal{O}(D)\,, \\ & s(\omega) = \dfrac{\mu_1}{2\mu_2}\left(\dfrac{\omega}{\sqrt{\omega^2 - 4c\mu_2}} - 1\right) + \mathcal{O}(D). \end{cases} \tag{4.28}$$

Specifically, we find that the leading order expression in small D is given by the quarter circle law

$$s(\omega) = \begin{cases} \frac{\mu_1}{2D\mu_2}\sqrt{4c\mu_2 - \omega^2} & \text{for} \quad \omega \in [0, 2\sqrt{c\mu_2}) \\ \frac{\mu_1}{2\mu_2}\left(\frac{\omega}{\sqrt{\omega^2 - 4c\mu_2}} - 1\right) & \text{for} \quad \omega \in (2\sqrt{c\mu_2}, \infty)\,. \end{cases} \tag{4.29}$$

Numerical Confirmation

This result (4.29) is universal in the sense that it does not depend on the details of the distribution of reaction rates, but only on the first and second moments. Fig. 4-2 shows two examples; power spectra of single instances of random networks with log-normal and exponential distributions of reaction rates. It is worth pointing out that the leading order 'bulk' and 'tail' expressions written in (4.29) do not agree at the band edge $\omega = 2\sqrt{c\mu_2}$, due to the change from $\mathcal{O}(D^{-1})$ to $\mathcal{O}(1)$.

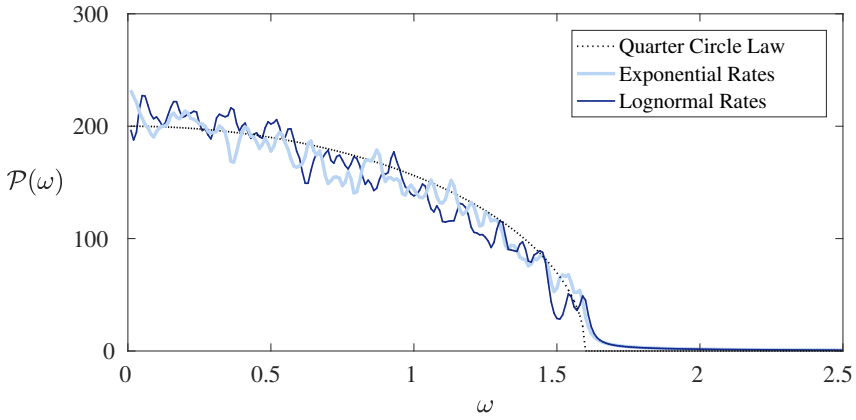

Figure(图) 4-2: Examples of the quarter-circle law for reaction networks with exponential and log-normal distributed rates. The arithmetic mean of the power spectrum for chemical species (solid lines) is compared to the theoretical result in the limit $N \to \infty, D \to 0$. In both cases the parameters are $N = 256, c = 32, D = 0.02, \mu_1 = 0.1, \mu_2 = 0.02$.

4.2 Adding Specific Species to the 'Island'

Our aim in this chapter is to explore the effect of coupling a small system of interest to a wider unknown network. After determining the large complicated interaction network in the last section, we focus on the symmetric Rock-Paper-Scissors model again, which has been discussed in detail in the sections 1.3.1 and 2.1.1.

Fig 4-3 illustrates the example of placing a competitive 3-species subsystem into the island. There are four kinds of interaction on the island. The first is the reactions which happen among all species in the environment. They are represented by blue points and arrows. The second is diffusion which is shown by red arrows. The third one is the cyclic dominance between the three species subsystem, which is shown by black points and arrows. It is exactly the RPS model discussed before. Lastly, represented by the light blue arrows, is the communication between the RPS subsystem and the environment. This interaction should be very weak, so we choose the lightest colour to show it. The numbers κ and 1 represent the reaction rates. We will introduce them in the description of the coupling model.

4.2.1 Coupling Model – Overlap of Two Evolving Systems

1. Rock-paper-scissors model - To make it clear, we first restate the subsystem. We use chemical reaction notation to describe the interactions of the subsystem at the individual level. Chemical reactions for the classic RPS (Rock-Paper-Scissors)

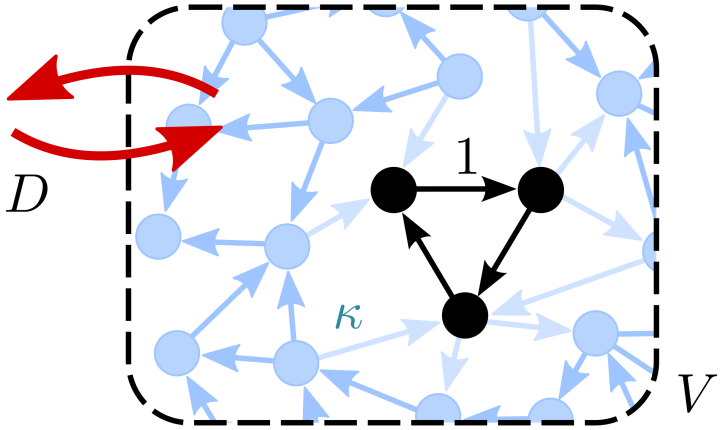

Figure(图) 4-3: Illustration of the autocatalytic network model, a three-species autocatalytic cycle with unit reaction rates (black) is contained in a volume V with dynamics damped by diffusion of strength D. This subsystem is coupled to a larger "bulk" network in the same volume, with coupling strength κ.

model are:

$$\begin{aligned} R + P &\xrightarrow{1} P + P, \\ P + S &\xrightarrow{1} S + S, \\ S + R &\xrightarrow{1} R + R. \end{aligned} \tag{4.30}$$

and the corresponding reactions for the diffusion are

$$R \xleftrightarrow{D} \varnothing, P \xleftrightarrow{D} \varnothing, S \xleftrightarrow{D} \varnothing. \tag{4.31}$$

with a constant $D \ll 1$, which is same as that mentioned before. Then following the definition in the last section, we define the two–body reaction rate matrix of subsystem (RPS) as $\boldsymbol{R}_{\mathrm{s}}$,

$$\boldsymbol{R}_{\mathrm{s}} := \begin{pmatrix} 0 & 1 & 0 \\ 0 & 0 & 1 \\ 1 & 0 & 0 \end{pmatrix} \tag{4.32}$$

So the deterministic dynamic of RPS is:

$$\begin{cases} \dot{x}_r = x_r(x_s - x_p) - Dx_r + D, \\ \dot{x}_p = x_p(x_r - x_s) - Dx_p + D, \\ \dot{x}_s = x_s(x_p - x_r) - Dx_s + D, \end{cases} \tag{4.33}$$

with the concentration of the three species being $\boldsymbol{x}_{\mathrm{s}} := (x_r, x_p, x_s)^T$. The equilibrium point of (4.33) is $\boldsymbol{x}_{\mathrm{s}}^\star = (x_r, x_p, x_s)^T = (1,1,1)^T$.

2. Random environment - The random environment is described by these chemical reactions:

$$X_i + X_j \xrightarrow{r_{ij}} 2X_j, \quad i,j \in \{1,...,N\}, \tag{4.34}$$

$$X_i \xleftrightarrow{D} \varnothing, \quad i \in \{1,...,N\}, \tag{4.35}$$

with r_{ij} sampled from prescribed distribution. The matrix $\boldsymbol{R}_{\mathrm{b}} := (r_{ij})$ is the two–element reaction rate matrix for the random environment, the 'bulk' network.

3. Coupling the RPS model and the random environment - Regard RPS as a subsystem, named X_{s}, with three elements (R, P, S). Coupling RPS X_{s} with X_j in the surrounding environment, here $j \in \{4,...,N+3\}$, we propose the following chemical reactions:

$$\begin{aligned} X_{\mathrm{s}} + X_j &\xrightarrow{r_{\mathrm{s}j}} 2X_j, \\ X_j + X_{\mathrm{s}} &\xrightarrow{r_{j\mathrm{s}}} 2X_{\mathrm{s}}. \end{aligned} \tag{4.36}$$

The rates $r_{\mathrm{s}j}$ and $r_{j\mathrm{s}}$ are also sampled from prescribed distribution, which can be chosen independent of the rate r_{ij} in the matrix $\boldsymbol{R}_{\mathrm{b}}$.

The overall reaction rate matrix of the coupled system is $\boldsymbol{R}$:

$$\boldsymbol{R} := \begin{pmatrix} \boldsymbol{R}_{\mathrm{s}} & (r_{\mathrm{s}j}) \\ (r_{j\mathrm{s}}) & \boldsymbol{R}_{\mathrm{b}} \end{pmatrix}. \tag{4.37}$$

This matrix is easily understood. The top-left 3×3 square matrix shows the reactions in the subsystem, while the bottom-right $N \times N$ square matrix describes the unknown 'bulk' network discussed in the last section. The remaining parts, a $3 \times N$ and a $N \times 3$ rectangular matrix, represent the couplings. Assuming a random distribution for the coupling reactions, we replace the sum of the row in the coupled matrix with the average, introducing $\kappa := \sum_j \mathbb{E}(\boldsymbol{R}_{ij}^2 + \boldsymbol{R}_{ji}^2)$. Again, we also assume that the reactions are not reciprocal, so $\boldsymbol{R}_{ij}\boldsymbol{R}_{ji} = 0$. Here, $i \in \{1,2,3\}$ and $j \in \{4,...,N+3\}$.

Similar to before, mean-field ODEs can also be used to describe the dynamics of the coupled system. If the vector of all chemical species is denoted by $\boldsymbol{x} = (x_1, x_2, x_3, x_4, ..., x_{N+3})^T$, there is an equilibrium point which is also the vector $\boldsymbol{x}^\star$ with all entries equal to 1. After linearization around the fixed point, the equation looks like:

$$\mathrm{d}\boldsymbol{x} = \boldsymbol{A}\boldsymbol{x}\mathrm{d}t + \frac{1}{\sqrt{V}}\boldsymbol{M}\mathrm{d}\boldsymbol{W}(t), \tag{4.38}$$

where $\boldsymbol{A}$ and $\boldsymbol{M}$ are:

$$\boldsymbol{A} = \boldsymbol{R}^T - \boldsymbol{R} - \boldsymbol{D} = \begin{pmatrix} \boldsymbol{A}_\mathrm{s} & \boldsymbol{A}_\mathrm{c} \\ -\boldsymbol{A}_\mathrm{c}^T & \boldsymbol{A}_\mathrm{b} \end{pmatrix}, \quad \boldsymbol{M}\boldsymbol{M}^T = \boldsymbol{B} = \begin{pmatrix} \boldsymbol{B}_\mathrm{s} & \boldsymbol{B}_\mathrm{c} \\ \boldsymbol{B}_\mathrm{c}^T & \boldsymbol{B}_\mathrm{b} \end{pmatrix}. \tag{4.39}$$

and B has entries $\boldsymbol{B}_{ij} = \delta_{i,j} \sum_k (\boldsymbol{R}_{ik} + \boldsymbol{R}_{ki}) - (\boldsymbol{R}_{ij} + \boldsymbol{R}_{ji})$.

4.2.2 Spectrum Calculation

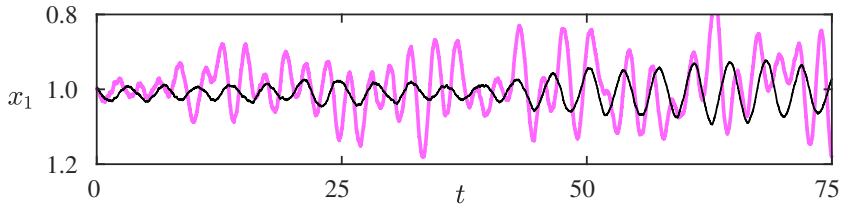

Figure(图) 4-4: Typical stochastic time series for the subsystem in isolation (thin black) and when coupled (thick pink).

Our aim here is to explore the effect of coupling a small system of interest to a wider unknown network. It can be seen in Fig. 4-4 that the interference between a small subsystem and a wider reaction network causes stochastic oscillations typically to increase in both frequency and amplitude. In this subsection, we will calculate the power spectral density to show by how much it is enhanced due to the surrounding network.

Following the relevant calculation in section 2.1.1 above, the power spectrum of the chemical species in the isolated subsystem is found to be

$$\mathcal{P}_\mathrm{s}(\omega) = (\boldsymbol{A}_\mathrm{s} - \mathrm{i}\omega\boldsymbol{I})^{-1}\boldsymbol{B}_\mathrm{s}(\boldsymbol{A}_\mathrm{s} - \mathrm{i}\omega\boldsymbol{I})^{-\dagger}. \tag{4.40}$$

For each species of the subsystem, we obtain:

$$\mathcal{P}_{ii} = \frac{2(\omega^2 + 3 + D^2)}{(\omega^2 - 3)^2 + 2D^2(\omega^2 + 3) + D^4}, \quad i \in \{1, 2, 3\}. \tag{4.41}$$

by directly calculating (4.40). The factor of $(\omega^2 - 3)^2$ in the denominator is responsible for a pronounced peak in the spectrum at $\omega = \sqrt{3}$, corresponding to the dominant frequency of oscillation (visible in the 'isolated' timeseries shown in Fig. 4-4).

We know from section 4.1.1 that the PSD of the 'bulk' random network obeys the universal quarter circle law, shown in equation (4.29). Similarly, we extend the cavity method and obtain $\mathcal{P}_{ii}$ of the subsystem with coupling.

To study the effect of a weak coupling between the three component cycle and an unknown bulk, we propose the Hamiltonian $\mathcal{H} = \mathcal{H}^{\mathrm{s}} + \mathcal{H}^{\mathrm{b}} + \mathcal{H}^{\mathrm{c}}$, with s,b,c respectively denoting contributions coming from the three component subsystem, the bulk, and the coupling. Writing $\boldsymbol{\varphi}_{\mathrm{s}}$ for the vector of compound spins corresponding to the subsystem, we generalize (4.20) to the case where we consider removing the entire subsystem, as opposed to just a single site. We then have

$$f_{\mathrm{s}}(\boldsymbol{\varphi}_{\mathrm{s}}) = \frac{1}{\mathcal{Z}_{\mathrm{s}}} e^{-\mathcal{H}^{\mathrm{s}}} \int_{\mathbb{C}} \prod_{i\in \mathrm{s}, j\in \mathrm{b}} \left(e^{-(\mathcal{H}^{\mathrm{c}}_{ij} + \mathcal{H}^{\mathrm{c}}_{ji})} f_j^{(i)}(\boldsymbol{\varphi}_j) \mathrm{d}\boldsymbol{\varphi}_j \right) , \tag{4.42}$$

where the cavity distribution $f_j^{(i)}$ is the bulk distribution with covariance matrix $\boldsymbol{U}$ derived previously, which is known as $\boldsymbol{U} = \begin{pmatrix} s & r \\ -\bar{r} & 0 \end{pmatrix}$. That is because after deleteing all $i \in \mathrm{s}$ from the network, the remaining vertices are exactly the bulk network which has been studied before. Here both s and r have been derived and presented in formula (4.28). This is reasonable if the connectivity of the bulk is high, but the coupling between the bulk and the subsystem is sufficiently sparse that there are very few species in the bulk that are involved in a reaction with more than one subsystem species. So the cavity distribution $f_j^{(i)}$ could be written directly as:

$$f_j^{(i)}(\boldsymbol{\varphi}_j) = \frac{1}{\mathcal{Z}_j} \exp\left(-\boldsymbol{\varphi}_j^{\dagger} \boldsymbol{U}^{-1} \boldsymbol{\varphi}_j\right). \tag{4.43}$$

Applying the transformation (4.7) to the integration term in (4.42), we obtain a simplification:

$$\begin{aligned}
f_{\mathrm{s}}(\boldsymbol{\varphi}_{\mathrm{s}}) &= \frac{1}{\mathcal{Z}_{\mathrm{s}}} e^{-\mathcal{H}^{\mathrm{s}}} \prod_{i\in \mathrm{s}, j\in \mathrm{b}} \int_{\mathbb{C}} \left(e^{-(\boldsymbol{\varphi}_{\boldsymbol{i}}^{\dagger} \boldsymbol{Q}_{ij} \boldsymbol{\varphi}_j + \boldsymbol{\varphi}_j^{\dagger} \boldsymbol{Q}_{ji} \boldsymbol{\varphi}_i + \boldsymbol{\varphi}_j^{\dagger} \boldsymbol{U}^{-1} \boldsymbol{\varphi}_j)} \mathrm{d}\boldsymbol{\varphi}_j \right) , \\
&= \frac{1}{\mathcal{Z}_{\mathrm{s}}} e^{-\mathcal{H}^{\mathrm{s}}} \prod_{i\in \mathrm{s}, j\in \mathrm{b}} \left(e^{\boldsymbol{\varphi}_{\boldsymbol{i}}^{\dagger} \boldsymbol{Q}_{ij} \boldsymbol{U} \boldsymbol{Q}_{ji} \boldsymbol{\varphi}_i} \right) , \\
&= \frac{1}{\mathcal{Z}_{\mathrm{s}}} \exp\left\{ -\mathcal{H}^{\mathrm{s}} + \sum_{i\in \mathrm{s}, j\in \mathrm{b}} \boldsymbol{\varphi}_i^{\dagger} \boldsymbol{Q}_{ij} \boldsymbol{U} \boldsymbol{Q}_{ji} \boldsymbol{\varphi}_i \right\}, \\
&= \frac{1}{\mathcal{Z}_{\mathrm{s}}} \exp\left\{ -\mathcal{H}^{\mathrm{s}} + \sum_{i\in \mathrm{s}} \boldsymbol{\varphi}_i^{\dagger} \begin{pmatrix} 0 & \kappa\bar{r} \\ -\kappa r & -\kappa s \end{pmatrix} \boldsymbol{\varphi}_i \right\}, \\
&= \frac{1}{\mathcal{Z}_{\mathrm{s}}} \exp\left\{ -\mathcal{H}^{\mathrm{s}} + \boldsymbol{\varphi}_{\mathrm{s}}^{\dagger} \begin{pmatrix} 0 & \kappa\bar{r}\boldsymbol{I} \\ -\kappa r\boldsymbol{I} & -\kappa s\boldsymbol{I} \end{pmatrix} \boldsymbol{\varphi}_{\mathrm{s}} \right\}.
\end{aligned} \tag{4.44}$$

where we obtain the second line with equation (4.7) in theorem 4.1, and the fourth line by assuming a random distribution for the coupling reactions (encoded in the $\boldsymbol{Q}_{ij}$

above), and replacing the sum with the average i.e. $\kappa = \sum_j \mathbb{E}(\boldsymbol{R}_{ij}^2 + \boldsymbol{R}_{ji}^2)$. The $\boldsymbol{I}$ in the last line is an identity matrix with the same size of the subsystem matrix.

Following $\mathcal{H}$ in (4.11), we have $\mathcal{H}^{\mathrm{s}}$:

$$\mathcal{H}^{\mathrm{s}}(\boldsymbol{z}, \tilde{\boldsymbol{z}}) = \boldsymbol{z}_{\mathrm{s}}^{\dagger}(\boldsymbol{A}_{\mathrm{s}} - \mathrm{i}\omega\boldsymbol{I})^{\dagger}\tilde{\boldsymbol{z}}_{\mathrm{s}} - \tilde{\boldsymbol{z}}_{\mathrm{s}}^{\dagger}(\boldsymbol{A}_{\mathrm{s}} - \mathrm{i}\omega\boldsymbol{I})\boldsymbol{z}_{\mathrm{s}} + \tilde{\boldsymbol{z}}_{\mathrm{s}}^{\dagger}\boldsymbol{B}_{\mathrm{s}}\tilde{\boldsymbol{z}}_{\mathrm{s}}\,. \tag{4.45}$$

Plugging it into (4.44), we finally obtain the cavity density of the coupled subsystem:

$$f_{\mathrm{s}}(\boldsymbol{\varphi}_{\mathrm{s}}) = \mathcal{Z}_{\mathrm{s}}^{-1} e^{-\tilde{\mathcal{H}}_{\mathrm{s}}(\boldsymbol{z}, \tilde{\boldsymbol{z}})}\,, \tag{4.46}$$

with

$$\begin{aligned}\tilde{\mathcal{H}}^{\mathrm{s}}(\boldsymbol{z}, \tilde{\boldsymbol{z}}) &= \mathcal{H}^{\mathrm{s}}(\boldsymbol{z}, \tilde{\boldsymbol{z}}) - \boldsymbol{\varphi}_{\mathrm{s}}^{\dagger}\begin{pmatrix} 0 & \kappa\bar{r}\boldsymbol{I} \\ -\kappa r\boldsymbol{I} & -\kappa s\boldsymbol{I}\end{pmatrix}\boldsymbol{\varphi}_{\mathrm{s}}\,, \\ &= \boldsymbol{z}_{\mathrm{s}}^{\dagger}(\boldsymbol{A}_{\mathrm{s}} - \mathrm{i}\omega\boldsymbol{I} - \kappa r\boldsymbol{I})^{\dagger}\tilde{\boldsymbol{z}}_{\mathrm{s}} - \tilde{\boldsymbol{z}}_{\mathrm{s}}^{\dagger}(\boldsymbol{A}_{\mathrm{s}} - \mathrm{i}\omega\boldsymbol{I} - \kappa r\boldsymbol{I})\boldsymbol{z}_{\mathrm{s}} + \tilde{\boldsymbol{z}}_{\mathrm{s}}^{\dagger}(\boldsymbol{B}_{\mathrm{s}} + \kappa s\boldsymbol{I})\tilde{\boldsymbol{z}}_{\mathrm{s}}\,.\end{aligned} \tag{4.47}$$

Following the definition in section 4.1.1, the power spectral density for the coupled subsystem is obtained by integrating over the auxiliary field $\tilde{\boldsymbol{z}}_{\mathrm{s}}$:

$$\begin{aligned}\mathcal{P}_{\mathrm{s}} = \langle \boldsymbol{z}_{\mathrm{s}}\boldsymbol{z}_{\mathrm{s}}^{\dagger}\rangle &= \int_{\mathcal{C}} \boldsymbol{z}_{\mathrm{s}}\boldsymbol{z}_{\mathrm{s}}^{\dagger}\int_{\mathcal{C}} f_{\mathrm{s}}(\boldsymbol{\varphi}_{\mathrm{s}})\mathrm{d}\boldsymbol{\varphi}_{\mathrm{s}}\,, \\ &= \int_{\mathcal{C}} \boldsymbol{z}_{\mathrm{s}}\boldsymbol{z}_{\mathrm{s}}^{\dagger} e^{-\boldsymbol{z}_{\mathrm{s}}^{\dagger}(\boldsymbol{A}_{\mathrm{s}} - \mathrm{i}\omega - \kappa r)^{\dagger}(\boldsymbol{B}_{\mathrm{s}} + \kappa s)^{-1}(\boldsymbol{A}_{\mathrm{s}} - \mathrm{i}\omega - \kappa r)\boldsymbol{z}_{\mathrm{s}}}\mathrm{d}\boldsymbol{z}_{\mathrm{s}}\,, \\ &= (\boldsymbol{A}_{\mathrm{s}} - \mathrm{i}\omega\boldsymbol{I} - \kappa r\boldsymbol{I})^{-1}(\boldsymbol{B}_{\mathrm{s}} + \kappa s\boldsymbol{I})(\boldsymbol{A}_{\mathrm{s}} - \mathrm{i}\omega\boldsymbol{I} - \kappa r\boldsymbol{I})^{-\dagger}\,.\end{aligned} \tag{4.48}$$

Here in the second line we apply the transform (4.7) and in the third line (4.6). Finally we yield

$$\mathcal{P}_{\mathrm{s}} = (\boldsymbol{A}_{\mathrm{s}} - \mathrm{i}\omega\boldsymbol{I} - \kappa r\boldsymbol{I})^{-1}(\boldsymbol{B}_{\mathrm{s}} + \kappa s\boldsymbol{I})(\boldsymbol{A}_{\mathrm{s}} - \mathrm{i}\omega\boldsymbol{I} - \kappa r\boldsymbol{I})^{-\dagger}, \tag{4.49}$$

where $\boldsymbol{A}_{\mathrm{s}}$ and $\boldsymbol{B}_{\mathrm{s}}$ are respectively the Jacobian and noise covariance matrices corresponding to the subsystem, and s and r are respectively the power spectrum and cross-spectrum of the bulk, determined from the entries of $\boldsymbol{U}$. Comparing equation (4.49) to the unmodified power spectral density $\mathcal{P}(\omega) = (\boldsymbol{A} - \mathrm{i}\omega\boldsymbol{I})^{-1}\boldsymbol{B}(\boldsymbol{A} - \mathrm{i}\omega\boldsymbol{I})^{-\dagger}$, one can clearly see the effect of the coupling in modifying the frequency and amplitude of oscillations. According to our assumption on κ, we know κ is a nonnegative number. Besides, s and r are both given by equation (4.28). We can observe that the amplitude is enhanced because $\kappa s \geq 0$. The effects on the frequency will be discussed in the next section. Roughly speaking, the environment will accelerate the frequency of the oscillation in the subsystem.

4.2.3 Effects from the Complicated Environment

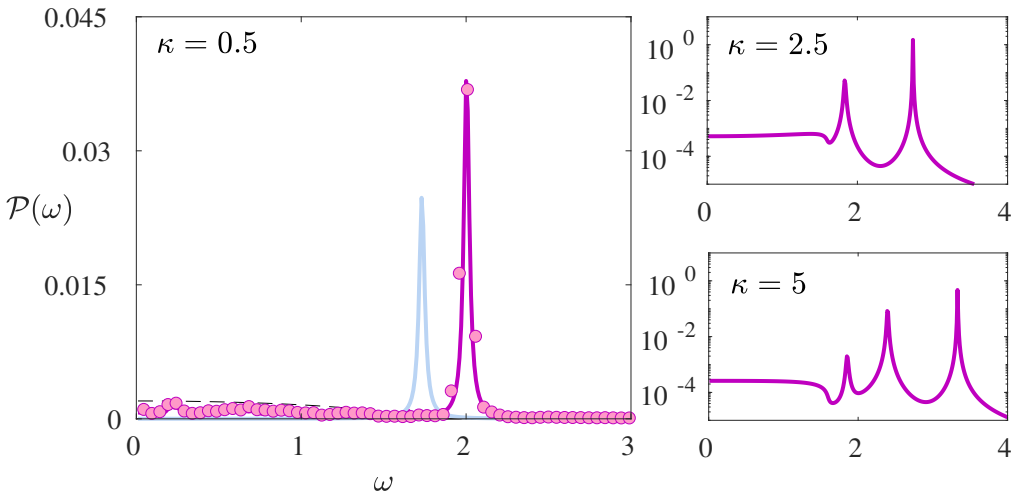

Figure(图) 4-5: Faster and stronger oscillations induced in the three-cycle when coupled to a random network. The left panel shows the peak in the power spectrum of the coupled system (dark solid line for theory, circles for the empirical spectrum of a time series from a microscopic stochastic simulation), relative to the peak observed for the isolated system (pale solid line). The right panels show the appearance of further spectral peaks as the coupling strength κ is increased. In all cases the bulk has log-normally distributed rates, with parameters the same as those in the Fig. 4-2.

Fig. 4-5 shows the results of simulations of the three component cycle, coupled to a large external bulk interaction network, compared with the results obtained when the system is modelled in isolation. The inset subfigures show that, despite the fact that the subsystem possesses only a single dominant frequency, the coupled system can exhibit pronounced stochastic oscillations of up to three distinct frequencies. To understand the origins of this effect, we explore the small D asymptotics of the modified power spectrum described by Eq. (4.49).

Examining the asymptotic expressions for the spectrum (4.29) and cross-spectrum (4.27) of the bulk, we find that $r(\omega)$ is (to leading order in small D) purely imaginary when ω is outside of the spectral bulk (i.e. $\omega > 2\sqrt{c\mu_2}$):

$$r(\omega) = \frac{\mathrm{i}(\sqrt{\omega^2 - 4c\mu_2} - \omega)}{2c\mu_2} + \mathcal{O}(D)\,. \tag{4.50}$$

In this case, the terms in (4.49) involving the inverse of $\boldsymbol{A}_{\mathrm{s}} - [\mathrm{i}\omega + \kappa r(\omega)]$ imply an order $1/D^2$ spike in the modified spectrum whenever $\mathrm{i}\omega + \kappa r(\omega)$ is close to an eigenvalue of the subsystem Jacobinan $\boldsymbol{A}_{\mathrm{s}}$. Specifically, if $\omega_i = \operatorname{Im}\lambda_i$ is the imaginary part of an eigenvalue of $\boldsymbol{A}_{\mathrm{s}}$, we can solve for ω in $\omega_i = \omega - \mathrm{i}\kappa r(\omega)$ to obtain an estimate for the

frequency ω_i^* of induced peak in the modified spectrum:

$$\omega_i^* = \omega_i + \frac{\kappa\sqrt{4(\kappa - c\mu_2) + \omega_i^2} - \kappa\omega_i}{2(\kappa - c\mu_2)} + \mathcal{O}(D)\,. \tag{4.51}$$

This calculation is predicated on the assumption that the excited frequency, ω_i^*, lies outside the spectrum of the bulk network. Following this reasoning, we expect to see a peak in the power spectrum of the coupled system corresponding to each eigenvalue λ_i, for which the corresponding frequency ω_i^* satisfies $\omega_i^* > 2\sqrt{c\mu_2}$.

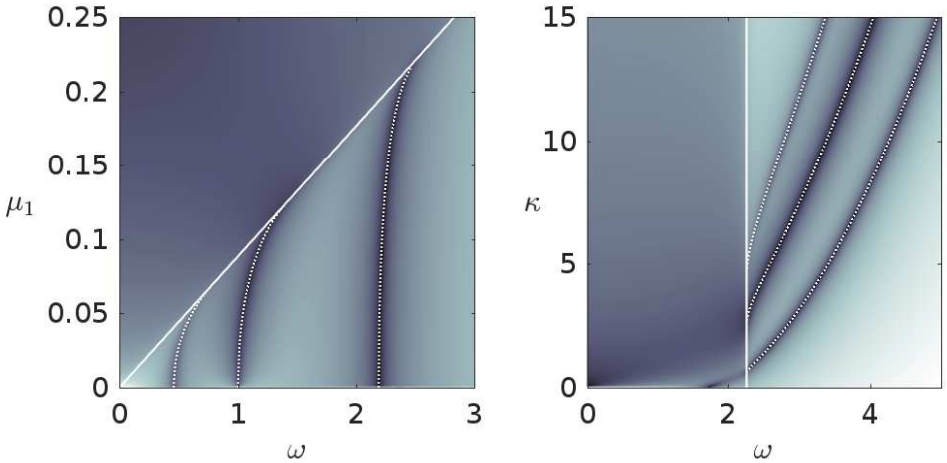

Figure(图) 4-6: Colourmaps showing the effect of varying reaction rate and coupling strength, for networks with $\mu_2 = \mu_1^2$. The colours of each horizontal slice corresponds to a power spectrum, with darker colours indicating larger values of $\mathcal{P}(\omega)$. Solid white lines denote the band edge of the spectral bulk $2\mu_1\sqrt{c}$, dashed white lines show the predicted locations of spectral peaks according to Eq. (4.51).

The colourmaps in Fig. 4-6 illustrate the effects of changing the reaction rates and the coupling strength on the observed number and location of spectral peaks. In the left panel, as the mean reaction rate μ_1 of the bulk is increased, we see that the subsystem peaks initially bend away from the bulk spectrum, before being eventually subsumed by it. The right panel shows the opposite curvature as κ is increased: from Eq. (4.51) we see that the "push" received by the subsystem peaks scales as a square-root for large κ.

As well as determining the position of the spectral peaks, the same method suffices to estimate their amplitude. By evaluating the modified power spectrum (4.49) at an excited frequency ω_i^* and expanding in small D we obtain

$$\mathcal{P}_{\mathrm{s}}(\omega_i^*) = \frac{c^2\mu_1^2(3 + \kappa s(\omega_i^*))}{3D^2(\kappa s(\omega_i^*) - c\mu_1)^2} + \mathcal{O}(1)\,, \tag{4.52}$$

In contrast to the positions of the spectral peaks, we find that their height scales linearly at both small and large coupling strength.

To conclude, we have shown here how the frequency, amplitude and multiplicity of stochastic oscillations can all be increased through interference between a subsystem of interest and a wider random reaction network to which it is coupled. Our results are of particular relevance to the study of ecosystem dynamics, where there is a long tradition of modeling ecological systems as random matrices and studying the resultant properties [46].

Chapter 5

Discussion and Conclusion 总结与探讨

5.1 3-species Competition

We have presented a detailed analysis of the simple Rock–Paper–Scissors game, played in a well-mixed population, where the effects of cyclic competition and mutation lead to oscillatory dynamics in chapter 2. With a win-lose symmetric payoff matrix, the power spectral density is computed to obtain the main frequency of the oscillation around the inner equilibrium, and then with asymmetric payoff, the global attraction point disappears but a limit cycle appears instead.

In the mean-field ODE model where the strategy mix in the population is described by replicator equations, there is a stable limit cycle, produced in a Hopf bifurcation, when the mutation rate μ is small enough compared to the win-lose asymmetry β in the pay-off matrix. For large finite population sizes N, the dynamics of the finite population, as given by stochastic 'chemical reactions' between the species, closely follow the ODE dynamics. Here we investigated a specific chemical reaction scheme that was chosen to be straightforward to implement in the parameter regime we are interested in. It should be noted that this choice is not unique and may well not be optimal; for example, it does not allow for the possibility of $\beta < 0$.

Stochastic simulations in the regime of very small mutation rates shows qualitatively, and quantitatively, different dynamics for the oscillations, with the system remaining at corners for most of the time. Mutations are rare, but an essential part of the dynamics. We presented a detailed description of the dynamics in this regime using a Markov chain model for the dynamics on the boundary of phase space, and then arguing that in this regime the assumption that the dynamics took place on the

boundary was valid, and led to a self-consistent picture.

Our third approach to the problem was to construct a stochastic differential equation, which, according to a theorem of Kurtz [37] approximates the individual-based dynamics for large but finite populations. This was successful in capturing the cross-over between the mean-field and fully stochastic regimes as the mutation rate μ decreased for a fixed population size. In general the effects of noise on nonlinear oscillators are a complex topic of significant current research interest, see [58]. Our work here has concentrated on understanding the cross-over between regions I and III. The cross-over occurs when $\mu N \ln N \approx 1$, and the period of the oscillations changes from the mean-field approximation $T_{\mathrm{ODE}} \sim 3\ln(1/\mu)$ to the stochastic approximation $T_{\mathrm{SSA}} \sim 3/(N\mu)$. Figure 2-17 summarises these three regions of the behaviour, plotting the period of the oscillations as a function of $\mu N \ln N$, comparing the expected period of stochastic simulations with $N = 2^{17}$ with the theoretical results presented above.

Our main conclusion is that as demographic fluctuations become more important (i.e. at small mutation rates and for small population sizes) the period of the cyclic oscillations increases significantly above that which would be predicted on the basis of the mean-field ODE model.

One interesting future question arises in the technique of finding chemical reactions which correspond to the deterministic equations. We have provided the method of deriving replicator equations from chemical reactions. Different chemical reaction schemes may have same mean–field equation to illustrate the dynamics. For example, in the simplest RPS model, the chemical reaction set

$$\begin{aligned} A + B &\xrightarrow{1+\gamma} B + B, \quad A + B \xrightarrow{\gamma} A + A, \\ B + C &\xrightarrow{1+\gamma} C + C, \quad B + C \xrightarrow{\gamma} B + B, \\ C + A &\xrightarrow{1+\gamma} A + A, \quad C + A \xrightarrow{\gamma} C + C, \end{aligned} \tag{5.1}$$

has the same mean–field dynamics as chemical reaction set

$$\begin{aligned} A + B &\xrightarrow{1} B + B, \\ B + C &\xrightarrow{1} C + C, \\ C + A &\xrightarrow{1} A + A. \end{aligned} \tag{5.2}$$

However, considering possible stochastic diffusion, we find that different chemical reaction sets give us different diffusion terms in the Fokker-Planck Equation and the SDE. In this thesis, we have assumed that the inverse reaction does not exist (i.e. $R_{ij}R_{ji} = 0$ where $\boldsymbol{R}$ is the reaction rate matrix) to avoid the possible complicated cases. But in

fact, it may exist in some chemical/ecological applications. So next we hope to anaylse in detail how different chemical reaction schemes may affect the stochastic dynamics in the RPS model.

5.2 Four-species Competition

We have presented a extension of the RPS model in chapter 3: four-species cyclic competitions. Similarly to the situation in chapter 2, we also considered a win-loss asymmetric payoff matrix with parameter β at the beginning. We then added a new parameter ε, which allows for greater variety in the dynamics.

Following the same study pattern, we establish a deterministic equation at first at the population level, and then find a corresponding chemical reaction scheme at the individual level. Assuming mutation rate $\mu = 0$, we can obtain the equilibria easily and analyse their existence and stability. Then we use the parameter plane (β, ε) to illustrate the dynamics in different regions. Most of our attention is focussed on the third quadrant of (β, ε) plane, in which there exist two heteroclinic cycles. They are named after their locations, as 'face cycle' and 'edge cycle'. We then concentrate on the 'face cycle', fixing $\beta = -1.5$. Through stability analysis of the 'face cycle', we find the conditions for the existence of the cycle is $\varepsilon \in (-1, 0)$ and the critical value of stable cycle is $\varepsilon = -1/6$. Again we choose the period of the 'face cycle' to show the variation of the deterministic dynamics. Considering a combination of local and global maps, we can estimate the period with an iterating equation with parameters K and h, which are independent of ε and μ. At large population size N, simulation results coincide with our estimations well.

In the future there are many points which can be worked on. We have presented an approximation of the period of 'face cycle' at population level with estimation of parameters $K = 0.12$ and $h = 0.9$, so next in the stochastic case we plan to find out the relationship between K, h and the population size of simulation N. Further more, we can carry out the simulation with smaller N to find more differences between stochastic dynamics and deterministic dynamics

5.3 Many species Competition

We have presented a detailed analysis of how the frequency, amplitude and multiplicity of stochastic oscillations of a subsystem (RPS model) are increased when interfering with a wider random reaction network. By assuming the large 'bulk' network is a high-dimensional autocatalytic network and weight of the edges in the network obeys an independent distribution, we use the cavity method to obtain its spectrum.

The spectrum illustrates the average oscillatory behavior of species in the networks. Specifically it predicts the frequency, amplitude distribution of each species — here given by a universal quarter circle. After that, we place a RPS model with diffusion in the 'bulk' network. The RPS model with diffusion can be embedded in a large autocatalytic network. The competitions among three species form strong edges in their small network. If the small network has weak communication with the large 'bulk' network, the stochastic oscillations which exist previously will be enhanced. The cavity method is applied again to predict how much the frequency and amplitude are increased and, appearance of new peaks in the spectrum of the coupled network when interference is large.

One interesting future question is how additional structure in the bulk network (see e.g. [3, 23]) might affect subsystem dynamics. In chapter 4 we have assumed that the bulk network is an almost fully connected network with very weak links between each pair of vertices, so the TAP approach gives a good approximation to the real case. If the network has some special properties, e.g. it is not fully connected but has many long loops, because it is a tree-like graph, the cavity method might also offer a good approximation. However, if the 'bulk' network has many short loops, the correlations between vertices might not be ignored in the case of $N \to \infty$. Then the cavity method is probably not suitable and we may consider other approaches to analyse the model.

More generally we hope that our findings will stimulate further work on the important question of how interactions with random environments can complicate our understanding of biological dynamics.

Appendices

Appendices 附录 A

Itô's formula

A stochastic differential equation is an ordinary differential equation with a random forcing, usually given by a white noise $\eta(t)$:

$$\frac{\mathrm{d}x}{\mathrm{d}t} = a(x,t) + b(x,t)\eta(t), \qquad x(0) = x_0, \tag{A.1}$$

where $a(x,t)$ and $b(x,t)$ are parameters, $\eta(t) = \frac{\mathrm{d}W(t)}{\mathrm{d}t}$ for a Wiener process $W(t)$. It is also written in short as:

$$\mathrm{d}x = a(x,t)\mathrm{d}t + b(x,t)\mathrm{d}W(t), \qquad x(0) = x_0. \tag{A.2}$$

Similarly, a multivariable SDE system is written as:

$$\mathrm{d}\boldsymbol{x} = \boldsymbol{u}(\boldsymbol{x},t)\mathrm{d}t + \boldsymbol{M}(\boldsymbol{x},t)\mathrm{d}\boldsymbol{W}(t), \qquad \boldsymbol{x}(0) = \boldsymbol{x}_0. \tag{A.3}$$

where $\boldsymbol{u}$ and $\boldsymbol{M}$ are parameters.

All time series $x(t)$ or $\boldsymbol{x}(t)$ which is used in the following content is defined by SDE of (A.2) or (A.3).

Definition A.1 (Wiener process)**.** *We say $\{W(t) : t \in \mathbb{R}^+\}$ is a 1-variable Wiener process if it is a real-valued Gaussian process with continous sample paths, mean function $\mu(t) = 0$, and covariance function cov(s,t)=min{s,t}. Here Gaussian process means that $\{W(t_1), W(t_2), ..., W(t_N)\}$ follows a multivariate Gaussian distribution for any $t_1, ..., t_N \in \mathbb{R}^+$ and $N \in \mathbb{N}$. A n-variable Wiener process is defined by $\boldsymbol{W}(t) = [W_1(t), ..., W_n(t)]^T$.*

Lemma A.1 (Properties of Wiener process)**.** *A wiener process $W(t)$ is defined by definition A.1, then it has following properties:*

1. *$W(0) = 0$;*

2. $W(t+\tau) - W(t) \sim \mathcal{N}(0,t)$;

3. $\langle W(t), W(t)\rangle = t$;

4. $(\mathrm{d}W(t))^2 = \mathrm{d}t$.

For the n-variable Wiener process $\boldsymbol{W}(t) = [W_1(t), \cdots, W_n(t)]^T$, *the relative properties are:*

1. $\mathrm{d}W_i(t)\mathrm{d}W_j(t) = \delta_{ij}\mathrm{d}t$;

2. $[\mathrm{d}W_i(t)]^{N+2} = 0\,(N > 0)$;

3. $\mathrm{d}W_i(t)\mathrm{d}t = 0$;

4. $\mathrm{d}t^{1+N} = 0$.

Lemma A.2 (one-dimensional Itô's formula)**.** *Given a function of* $x(t)$*:* $f[x(t)]$ *which has continuous derivatives* f' *and* f''*, we can show that*

$$\mathrm{d}f[x(t)] = \{a(x,t)f'[x(t)] + \frac{1}{2}b^2(x,t)f''[x(t)]\}\mathrm{d}t + b(x,t)f'[x(t)]\mathrm{d}W(t). \tag{A.4}$$

Proof(证明). By expanding $\mathrm{d}f[x(t)]$ to second order in $\mathrm{d}W(t)$, we have

$$\begin{aligned}\mathrm{d}f[x(t)] &= f[x(t)+\mathrm{d}x(t)] - f[x(t)] \\ &= f'[x(t)]\mathrm{d}x(t) + \frac{1}{2}f''[x(t)][\mathrm{d}x(t)]^2 + \cdots \\ &= f'[x(t)][a(x,t)\mathrm{d}t + b(x,t)\mathrm{d}W(t)] \\ &+ \frac{1}{2}b^2(x,t)f''[x(t)][\mathrm{d}W(t)]^2 + \cdots\end{aligned} \tag{A.5}$$

where all other terms are discarded because the higher order of $[\mathrm{d}W(t)]^{N+2} = 0$, $\mathrm{d}W(t)\mathrm{d}t = 0$ and $\mathrm{d}t^{1+N} = 0$ for $N > 0$. We use the property of the Wiener process, $[\mathrm{d}W(t)]^2 = \mathrm{d}t$, to obtain equation (A.4) □

Lemma A.3 (general Itô's formula)**.** *Given a function of* $\boldsymbol{x}(t)$*:* $f[\boldsymbol{x}(t)]$ *which has continuous derivatives* $\partial_i f(\boldsymbol{x})$ *and* $\partial_i\partial_j f(\boldsymbol{x})$*, we can show that*

$$\begin{aligned}\mathrm{d}f(\boldsymbol{x}) = &\left\{\sum_i \boldsymbol{u}(\boldsymbol{x},t)\partial_i f(\boldsymbol{x}) + \frac{1}{2}\sum_{i,j}[\boldsymbol{M}(\boldsymbol{x},t)\boldsymbol{M}^T(\boldsymbol{x},t)]_{ij}\partial_i\partial_j f(\boldsymbol{x})\right\}\mathrm{d}t \\ &+ \sum_{i,j}\boldsymbol{M}_{ij}(\boldsymbol{x},t)\partial_i f(\boldsymbol{x})\mathrm{d}\boldsymbol{W}_j(t).\end{aligned} \tag{A.6}$$

Proof(证明). For an n dimensional Wiener process $\boldsymbol{W}(t) = [W_1(t), ..., W_n(t)]^T$, we have shown that

$$\begin{aligned} &\mathrm{d}W_i(t)\mathrm{d}W_j(t) = \delta_{ij}\mathrm{d}t\,, \\ &[\mathrm{d}W_i(t)]^{N+2} = 0\,(N > 0)\,, \\ &\mathrm{d}W_i(t)\mathrm{d}t = 0\,, \\ &\mathrm{d}t^{1+N} = 0, \end{aligned} \tag{A.7}$$

with the independence of $\mathrm{d}W_i(t)$ and $\mathrm{d}W_j(t)$. Then simply follow the procedure in the last proof, we can obtain the general Itô's formula (A.6). □

Theorem A.2 (Connection between F-P equation and SDE)**.** *The F-P equation for the conditional probability density $p(\boldsymbol{x}, t|\boldsymbol{x}_0, t_0) \equiv p$ is*

$$\partial_t p = -\sum_i \partial_i[\boldsymbol{u}_i(\boldsymbol{x})p] + \frac{1}{2}\sum_{i,j}\partial_i\partial_j\{[\boldsymbol{M}(\boldsymbol{x})\boldsymbol{M}^T(\boldsymbol{x})]_{ij}p\}. \tag{A.8}$$

It is equivalent to a multi-variable SDE:

$$\mathrm{d}\boldsymbol{x} = \boldsymbol{u}(\boldsymbol{x})\mathrm{d}t + \boldsymbol{M}(\boldsymbol{x})\mathrm{d}\boldsymbol{W}(t). \tag{A.9}$$

Proof(证明). We now consider a function about $\boldsymbol{x}(t)$ which satisfies the conditions in Itô formula, and then using Itô formula

$$\begin{aligned} \frac{\langle \mathrm{d}f[\boldsymbol{x}(t)]\rangle}{\mathrm{d}t} &= \frac{\mathrm{d}}{\mathrm{d}t}\langle f[\boldsymbol{x}(t)]\rangle\,, \\ &= \left\langle \sum_i \boldsymbol{u}(\boldsymbol{x})\partial_i f(\boldsymbol{x}) + \frac{1}{2}\sum_{i,j}[\boldsymbol{M}(\boldsymbol{x})\boldsymbol{M}^T(\boldsymbol{x})]_{ij}\partial_i\partial_j f(\boldsymbol{x}) \right\rangle \end{aligned} \tag{A.10}$$

$\boldsymbol{x}(t)$ is a random process defined by SDE (A.9), it has a conditional probability density $p(\boldsymbol{x}, t|\boldsymbol{x}_0, t_0)$ and

$$\begin{aligned} \frac{\mathrm{d}}{\mathrm{d}t}\langle f[\boldsymbol{x}(t)]\rangle &= \int f(\boldsymbol{x})\partial_t p\mathrm{d}\boldsymbol{x}\,, \\ &= \int \left\{ \sum_i \boldsymbol{u}(\boldsymbol{x})\partial_i f(\boldsymbol{x}) + \frac{1}{2}\sum_{i,j}[\boldsymbol{M}(\boldsymbol{x})\boldsymbol{M}^T(\boldsymbol{x})]_{ij}\partial_i\partial_j f(\boldsymbol{x}) \right\} p\mathrm{d}\boldsymbol{x}, \end{aligned} \tag{A.11}$$

where the integration $\int \mathrm{d}\boldsymbol{x}$ represents $\int \cdots \int \mathrm{d}x_1 \cdots \mathrm{d}x_n$, and n is the number of di-

mension of $\boldsymbol{x}$. Then we integrate it by parts and discard the surface terms to obtain:

$$\int f(\boldsymbol{x})\partial_t p \mathrm{d}\boldsymbol{x} = \int f(\boldsymbol{x}) \left\{ \sum_i -\partial_i [\boldsymbol{u}(\boldsymbol{x})p] + \frac{1}{2} \sum_{i,j} \partial_i \partial_j \left\{ [\boldsymbol{M}(\boldsymbol{x})\boldsymbol{M}^T(\boldsymbol{x})]_{ij} p \right\} \right\} \mathrm{d}\boldsymbol{x}, \tag{A.12}$$

and hence, since f is arbitrary we obtain (A.8).

□

Appendices 附录 B

Power Spectral Density

Definition B.1 (Power Spectral Density)**.** *The Power Spectral Density of the stochastic scalar process $x(t)$ is defined in two stages. First, define*

$$y(\omega) = \int_0^T \mathrm{e}^{-\mathrm{i}\omega t} x(t) \mathrm{d}t, \tag{B.1}$$

then the spectrum is defined by

$$\mathcal{P}(\omega) = \lim_{T\to\infty} \frac{1}{2\pi T} \left| y(\omega) \right|^2 . \tag{B.2}$$

Definition B.2 (Autocorrelation function)**.** *Given a measurable quantity, a stochastic process $x(t)$ which fluctuates with time, its autocorrelation function is defined to be:*

$$G(\tau) = \lim_{T\to\infty} \frac{1}{T} \int_0^T x(t)x(t+\tau) \mathrm{d}t. \tag{B.3}$$

Theorem B.3 (Wiener-Khinchin theorem)**.** *The Power Spectral Density of the stochastic process $x(t)$ is the Fourier Transform of its autocorrelation function*

$$\mathcal{P}(\omega) = \frac{1}{2\pi} \int_{-\infty}^{\infty} \mathrm{e}^{-\mathrm{i}\omega\tau} G(\tau) \mathrm{d}\tau \tag{B.4}$$

where the autocorrelation function $G(\tau)$ of $x(t)$ is defined above.

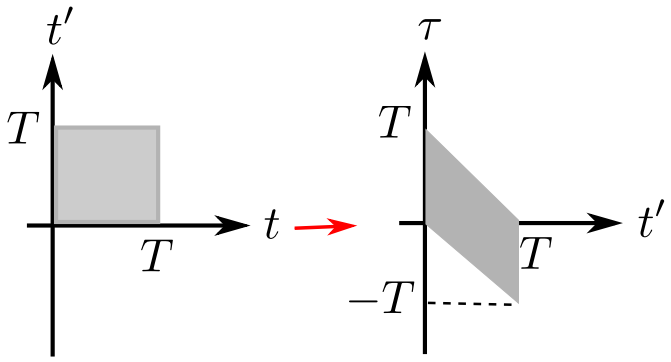

Figure(图) B-1: Transformation of integration domain from (t, t') to (t', τ).

Proof(证明). Firstly we show $G(\tau)$ is an even function:

$$\begin{aligned} G(-\tau) =& \lim_{T\to\infty} \frac{1}{T} \int_0^T x(t)x(t-\tau)\mathrm{d}t \\ =& \lim_{T\to\infty} \frac{1}{T} \int_{-\tau}^{T-\tau} x(t'+\tau)x(t')\mathrm{d}t' \\ =& \lim_{T\to\infty} \frac{1}{T} \int_{-\tau}^{0} x(t'+\tau)x(t')\mathrm{d}t' \\ &+ \lim_{T\to\infty} \frac{1}{T} \int_0^T x(t'+\tau)x(t')\mathrm{d}t' \\ &- \lim_{T\to\infty} \frac{1}{T} \int_{T-\tau}^{T} x(t'+\tau)x(t')\mathrm{d}t' \\ =& G(\tau). \end{aligned} \tag{B.5}$$

The last equality holds in the limit $T \to \infty$.

By definition (B.2), the PSD is written as:

$$\mathcal{P}(\omega) = \lim_{T\to\infty} \frac{1}{2\pi T} \left[\int_0^T \mathrm{e}^{-\mathrm{i}\omega t} x(t)\mathrm{d}t \int_0^T \mathrm{e}^{\mathrm{i}\omega t'} x^*(t')\mathrm{d}t' \right]. \tag{B.6}$$

where $x(t)$ is a real-valued process which means $x^*(t) = x(t)$. Changing the integration

domain from (t, t') to (t', τ) with $\tau = t - t'$, we have

$$\begin{aligned}
\mathcal{P}(\omega) &= \lim_{T\to\infty} \frac{1}{2\pi T} \int_0^T \mathrm{e}^{-\mathrm{i}\omega\tau} \int_0^{T-\tau} x(t')x(t'+\tau)\mathrm{d}t'\mathrm{d}\tau \\
&\quad + \lim_{T\to\infty} \frac{1}{2\pi T} \int_{-T}^0 \mathrm{e}^{-\mathrm{i}\omega\tau} \int_{-\tau}^T x(t')x(t'+\tau)\mathrm{d}t'\mathrm{d}\tau \\
&= \lim_{T\to\infty} \frac{1}{2\pi T} \int_0^T \mathrm{e}^{-\mathrm{i}\omega\tau} \int_0^{T-\tau} x(t')x(t'+\tau)\mathrm{d}t'\mathrm{d}\tau \\
&\quad + \lim_{T\to\infty} \frac{1}{2\pi T} \int_0^T \mathrm{e}^{\mathrm{i}\omega\tau'} \int_0^{T-\tau'} x(t'+\tau')x(t')\mathrm{d}t'\mathrm{d}\tau' \quad (\tau' = -\tau) \\
&= \lim_{T\to\infty} \frac{1}{2\pi T} \int_0^T \left(\mathrm{e}^{-\mathrm{i}\omega\tau} + \mathrm{e}^{\mathrm{i}\omega\tau}\right) \int_0^{T-\tau} x(t')x(t'+\tau)\mathrm{d}t'\mathrm{d}\tau \\
&= \lim_{T\to\infty} \left[\frac{1}{\pi} \int_0^T \cos(\omega\tau) \frac{1}{T} \int_0^{T-\tau} x(t)x(t+\tau)\mathrm{d}t\mathrm{d}\tau\right]
\end{aligned} \tag{B.7}$$

and taking the limit $T \to \infty$, (B.7) is

$$\mathcal{P}(\omega) = \frac{1}{\pi} \int_0^\infty \cos(\omega\tau) G(\tau)\mathrm{d}\tau. \tag{B.8}$$

This is a fundamental result which relates the Fourier transform of the autocorrelation function to the spectrum. Because the autocorrelation function is an even function which has been shown in equation (B.5), we can obtain that

$$\int_{-\infty}^\infty \sin(\omega\tau) G(\tau)\mathrm{d}\tau = 0. \tag{B.9}$$

and

$$\int_{-\infty}^0 \cos(\omega\tau) G(\tau)\mathrm{d}\tau = \int_0^\infty \cos(\omega\tau) G(\tau)\mathrm{d}\tau. \tag{B.10}$$

So from equations (B.8), (B.9) and (B.10) finally we obtain

$$\mathcal{P}(\omega) = \frac{1}{2\pi} \int_{-\infty}^\infty \mathrm{e}^{-\mathrm{i}\omega\tau} G(\tau)\mathrm{d}\tau. \tag{B.11}$$

□

Theorem B.4. *In general, the definitions and theorem is also valid in many-variable systems. If $\boldsymbol{x}(t)$ is given by a linear stochastic differential equation in the form of:*

$$\mathrm{d}\boldsymbol{x} = \boldsymbol{A}\boldsymbol{x}\mathrm{d}t + \boldsymbol{M}\mathrm{d}\boldsymbol{W}(t), \tag{B.12}$$

where $\boldsymbol{A}$ and $\boldsymbol{M}$ are constant matrices with $\boldsymbol{M}\boldsymbol{M}^T = \boldsymbol{B}$ and $\boldsymbol{B}$ is also a constant matrix and $\boldsymbol{W}(t)$ is a multivariate Wiener process. Then the Power Spectral Density

of the stochastic process $\boldsymbol{x}(t)$ *is*

$$\boldsymbol{\mathcal{P}}(\omega) = \frac{1}{2\pi}(\boldsymbol{A} - \mathrm{i}\omega\boldsymbol{I})^{-1}\boldsymbol{B}(\boldsymbol{A} - \mathrm{i}\omega\boldsymbol{I})^{-\dagger}. \tag{B.13}$$

The stochastic process which is define by the SDE (B.12) *is called multivariate Ornstein–Uhlenbeck process.*

Proof(证明). Generally speaking, a stochastic process is stationary if the correlation function of the process $x(t)$ which is defined by

$$\langle x(s), x(t)\rangle = \langle x(s)x(t)\rangle - \langle x(s)\rangle\langle x(t)\rangle \tag{B.14}$$

depends only on time difference $|t-s|$. Here $\langle x(t)\rangle$ represents mean and $\langle x(s), x(t)\rangle$ represents correlation function. The *Ornstein–Uhlenbeck process* is an example which has a stationary solution [19].

Because $\boldsymbol{A}$ and $\boldsymbol{M}$ are constant matrices, the solution to the SDE (B.12) can be easily obtained in the form:

$$\boldsymbol{x}(t) = \exp(t\boldsymbol{A})\boldsymbol{x}(0) + \int_0^t \exp[(t-t')\boldsymbol{A}]\boldsymbol{M}\mathrm{d}\boldsymbol{W}_{t'}. \tag{B.15}$$

The mean is

$$\langle \boldsymbol{x}(t)\rangle = \exp(t\boldsymbol{A})\langle \boldsymbol{x}(0)\rangle. \tag{B.16}$$

The correlation function follows definition (B.14) similarly

$$\boldsymbol{G}(t-s) = \langle \boldsymbol{x}(t), \boldsymbol{x}^T(s)\rangle = \int_0^{\min(t,s)} \exp[(t-t')\boldsymbol{A}]\boldsymbol{M}\boldsymbol{M}^T \exp[(s-t')\boldsymbol{A}]\mathrm{d}t'. \tag{B.17}$$

If matrix $\boldsymbol{A}$ has only eigenvalues with negative real part, the correlation function becomes stationary. In fact, if we set the initial time at $-\infty$ rather than 0, the solution (B.15) becomes

$$\boldsymbol{x}_{\mathrm{s}}(t) = \int_{-\infty}^t \exp[(t-t')\boldsymbol{A}]\boldsymbol{M}\mathrm{d}\boldsymbol{W}_{t'}, \tag{B.18}$$

with $\langle \boldsymbol{x}_{\mathrm{s}}(t)\rangle = 0$ and $\langle \boldsymbol{x}_{\mathrm{s}}(t), \boldsymbol{x}^T\mathrm{s}(s)\rangle$ is

$$\langle \boldsymbol{x}_{\mathrm{s}}(t), \boldsymbol{x}_{\mathrm{s}}^T(s)\rangle = \int_{-\infty}^t \exp[(t-t')\boldsymbol{A}]\boldsymbol{M}\boldsymbol{M}^T\exp[(s-t')\boldsymbol{A}^T]\mathrm{d}t'. \tag{B.19}$$

Let us define the stationary covariance matrix $\boldsymbol{\sigma}$ by

$$\boldsymbol{\sigma} = \langle \boldsymbol{x}_{\mathrm{s}}(t), \boldsymbol{x}_{\mathrm{s}}^T(t)\rangle. \tag{B.20}$$

Following [19](section 4.5.6), we can use $\boldsymbol{\sigma}$ to calculate that

$$\begin{aligned}\boldsymbol{A\sigma}+\boldsymbol{\sigma A}^T &= \int_{-\infty}^{t} \boldsymbol{A}\exp[(t-t')\boldsymbol{A}]\boldsymbol{B}\exp[(t-t')\boldsymbol{A}^T]\mathrm{d}t' \\ &\quad + \int_{-\infty}^{t} \exp[(t-t')\boldsymbol{A}]\mathbf{B}\exp[(t-t')\boldsymbol{A}^T]\boldsymbol{A}^T\mathrm{d}t' \\ &= \int_{-\infty}^{t} \frac{\mathrm{d}}{\mathrm{d}t'}\{\exp[(t-t')\boldsymbol{A}]\mathbf{B}\exp[(t-t')\boldsymbol{A}^T]\}\mathrm{d}t'.\end{aligned} \tag{B.21}$$

Carrying out the integral in (B.21), by assuming the eigenvalues of $\boldsymbol{A}$ have negative real part we find that the lower limit vanishes and only the upper limit remains. Then the final result is

$$\boldsymbol{A\sigma}+\boldsymbol{\sigma A}^T = \boldsymbol{B}, \tag{B.22}$$

which is useful later in the calculations.

The autocorrelation function $G(\tau)$ which is defined in (B.3) and (B.14) is same as follows:

$$\boldsymbol{G}(t-s) = \langle \boldsymbol{x}_{\mathrm{s}}(t), \boldsymbol{x}_{\mathrm{s}}^T(s)\rangle. \tag{B.23}$$

If $t > s$,

$$\begin{aligned}\langle \boldsymbol{x}_{\mathrm{s}}(t), \boldsymbol{x}_{\mathrm{s}}^T(s)\rangle =& \exp[(t-s)\boldsymbol{A}] \int_{-\infty}^{s} \exp[(s-t')\boldsymbol{A}]\boldsymbol{B}\exp[(s-t')\boldsymbol{A}^T]\mathrm{d}t' \\ =& \exp[\boldsymbol{A}(t-s)]\boldsymbol{\sigma}\end{aligned} \tag{B.24}$$

and similarly if $t < s$, we get

$$\langle \boldsymbol{x}_{\mathrm{s}}(t), \boldsymbol{x}_{\mathrm{s}}^T(s)\rangle = \boldsymbol{\sigma}\exp[(s-t)\boldsymbol{A}^T]. \tag{B.25}$$

So we conclude that the autocorrelation function $\boldsymbol{G}(\tau)$ is

$$\boldsymbol{G}(\tau) = \begin{cases} \exp(\tau\boldsymbol{A})\boldsymbol{\sigma} & \text{if} \quad \tau \geq 0 \\ \boldsymbol{\sigma}\exp(-\tau\boldsymbol{A}^T) & \text{if} \quad \tau < 0. \end{cases} \tag{B.26}$$

Now that we have obtained the autocorrelation function, $\boldsymbol{G}(\tau)$, it is straightforward

to calculate the Power Spectral Density:

$$\begin{aligned}\boldsymbol{\mathcal{P}}(\omega) =& \frac{1}{2\pi}\int_{-\infty}^{\infty} \mathrm{e}^{-\mathrm{i}\omega\tau}\boldsymbol{G}(\tau)\mathrm{d}\tau \\ =& \frac{1}{2\pi}\left\{\int_{0}^{\infty} \exp\left[\tau(\boldsymbol{A}-\mathrm{i}\omega\boldsymbol{I})\right]\boldsymbol{\sigma}\mathrm{d}\tau + \int_{-\infty}^{0} \boldsymbol{\sigma}\exp\left[-\tau(\boldsymbol{A}^T+\mathrm{i}\omega\boldsymbol{I})\right]\mathrm{d}\tau\right\} \\ =& \frac{1}{2\pi}\left[(\boldsymbol{A}-\mathrm{i}\omega\boldsymbol{I})^{-1}\boldsymbol{\sigma} + \boldsymbol{\sigma}(\boldsymbol{A}^T+\mathrm{i}\omega\boldsymbol{I})^{-1}\right].\end{aligned} \tag{B.27}$$

Hence, $(\boldsymbol{A}-\mathrm{i}\omega\boldsymbol{I})\boldsymbol{\mathcal{P}}(\omega)(\boldsymbol{A}-\mathrm{i}\omega\boldsymbol{I})^{\dagger} = \frac{1}{2\pi}(\sigma\boldsymbol{A}^T+\boldsymbol{A}\sigma)$ and using (B.22), we get (also see the result in [19] on page 111):

$$\boldsymbol{\mathcal{P}}(\omega) = \frac{1}{2\pi}(\boldsymbol{A}-\mathrm{i}\omega\boldsymbol{I})^{-1}\boldsymbol{B}(\boldsymbol{A}-\mathrm{i}\omega\boldsymbol{I})^{-\dagger}. \tag{B.28}$$

□

Bibliography 参考文献

[1] Visitor mauled to death by tiger in Ningbo zoo in China, Jan. 2017.

[2] P. A. Abrams and H. Matsuda. Prey adaptation as a cause of predator-prey cycles. *Evolution*, 51(6):1742–1750, Dec. 1997. WOS:000071652200004.

[3] S. Allesina and S. Tang. Stability criteria for complex ecosystems. *Nature*, 483(7388):205–208, Mar. 2012.

[4] R. M. Anderson and R. M. May. *Infectious Diseases of Humans: Dynamics and Control*. OUP Oxford, Aug. 1992.

[5] P. H. Baxendale and P. E. Greenwood. Sustained oscillations for density dependent Markov processes. *Journal of Mathematical Biology*, 63(3):433–457, Nov. 2010.

[6] M. Berr, T. Reichenbach, M. Schottenloher, and E. Frey. Zero-One Survival Behavior of Cyclically Competing Species. *Physical Review Letters*, 102(4):048102, Jan. 2009.

[7] P. Chossat and R. Lauterbach. *Methods in Equivariant Bifurcations and Dynamical Systems*. World Scientific, Feb. 2000. Google-Books-ID: ByHgMQ6xv_wC.

[8] G. W. A. Constable, T. Rogers, A. J. McKane, and C. E. Tarnita. Demographic noise can reverse the direction of deterministic selection. *Proceedings of the National Academy of Sciences*, 113(32):E4745–E4754, Sept. 2016.

[9] T. L. Czárán, R. F. Hoekstra, and L. Pagie. Chemical warfare between microbes promotes biodiversity. *Proceedings of the National Academy of Sciences*, 99(2):786–790, Jan. 2002.

[10] T. Dauxois, F. Di Patti, D. Fanelli, and A. J. McKane. Enhanced stochastic oscillations in autocatalytic reactions. *Physical Review E*, 79(3):036112, Mar. 2009.

[11] J. H. P. Dawes and M. O. Souza. A derivation of Holling's type I, II and III functional responses in predator-prey systems. *Journal of Theoretical Biology*, 327:11–22, June 2013.

[12] A. Dembo and A. Montanari. Ising models on locally tree-like graphs. *The Annals of Applied Probability*, 20(2):565–592, Apr. 2010.

[13] U. Dobramysl, M. Mobilia, M. Pleimling, and U. C. Täuber. Stochastic population dynamics in spatially extended predator – prey systems. *Journal of Physics A: Mathematical and Theoretical*, 51(6):063001, 2018.

[14] A. Dobrinevski and E. Frey. Extinction in neutrally stable stochastic Lotka-Volterra models. *Physical Review E*, 85(5):051903, May 2012.

[15] L. A. Dugatkin and H. K. Reeve. *Game Theory and Animal Behavior*. Oxford University Press, Mar. 2000. Google-Books-ID: ldmRTvHAFFQC.

[16] C. H. Durney, S. O. Case, M. Pleimling, and R. K. P. Zia. Saddles, arrows, and spirals: Deterministic trajectories in cyclic competition of four species. *Physical Review E*, 83(5):051108, May 2011.

[17] S. F. Edwards and R. C. Jones. The eigenvalue spectrum of a large symmetric random matrix. *Journal of Physics A: Mathematical and General*, 9(10):1595, May 1976.

[18] E. Fehr and U. Fischbacher. The nature of human altruism. *Nature*, 425(6960):785–791, Oct. 2003. WOS:000186118500034.

[19] C. W. Gardiner. *Stochastic methods: a handbook for the natural and social sciences*. Springer, Berlin, Jan. 2009.

[20] T. Gibbs, J. Grilli, T. Rogers, and S. Allesina. The effect of population abundances on the stability of large random ecosystems. *arXiv:1708.08837 [cond-mat, physics:physics, q-bio]*, Aug. 2017. arXiv: 1708.08837.

[21] D. T. Gillespie. Exact stochastic simulation of coupled chemical reactions. *The Journal of Physical Chemistry*, 81(25):2340–2361, Dec. 1977.

[22] S. A. Gredeskul and L. A. Pastur. Works of I. M. Lifshitz on disordered systems. *Journal of Statistical Physics*, 38(1-2):25–36, Jan. 1985.

[23] J. Grilli, T. Rogers, and S. Allesina. Modularity and stability in ecological communities. *Nature Communications*, 7:ncomms12031, June 2016.

[24] J. Guckenheimer and P. Holmes. *Nonlinear Oscillations, Dynamical Systems, and Bifurcations of Vector Fields*. Springer, New York, sixth edition edition, Feb. 2002.

[25] J. Henrich, R. Boyd, S. Bowles, C. Camerer, E. Fehr, H. Gintis, and R. McElreath. In search of Homo economicus: Behavioral experiments in 15 small-scale societies. *American Economic Review*, 91(2):73–78, May 2001. WOS:000169114600015.

[26] J. Hofbauer and K. Sigmund. *Evolutionary Games and Population Dynamics*. Cambridge University Press, May 1998.

[27] W. Hordijk and M. Steel. Chasing the tail: The emergence of autocatalytic networks. *Biosystems*, 152(Supplement C):1–10, Feb. 2017.

[28] J. Hubbard. Calculation of Partition Functions. *Physical Review Letters*, 3(2):77–78, July 1959.

[29] Y. Iwasa and A. Pomiankowski. Continual Change in Mate Preferences. *Nature*, 377(6548):420–422, Oct. 1995. WOS:A1995RY19000046.

[30] N. G. V. Kampen. *Stochastic Processes in Physics and Chemistry*. Elsevier, Nov. 1992. Google-Books-ID: 3e7XbMoJzmoC.

[31] B. Kerr, M. A. Riley, M. W. Feldman, and B. J. M. Bohannan. Local dispersal promotes biodiversity in a real-life game of rock – paper – scissors. *Nature*, 418(6894):171–174, July 2002.

[32] A. Khintchine. Korrelationstheorie der stationären stochastischen Prozesse. *Mathematische Annalen*, 109(1):604–615, Dec. 1934.

[33] J. Knebel, T. Krüger, M. F. Weber, and E. Frey. Coexistence and Survival in Conservative Lotka-Volterra Networks. *Physical Review Letters*, 110(16):168106, Apr. 2013.

[34] D. C. Krakauer and A. Mira. Reproductive biology - Mitochondria and the death of oocytes - Reply. *Nature*, 403(6769):501–501, Feb. 2000. WOS:000085227300036.

[35] M. Krupa. Robust heteroclinic cycles. *Journal of Nonlinear Science*, 7(2):129–176, Apr. 1997.

[36] M. Krupa and I. Melbourne. Asymptotic stability of heteroclinic cycles in systems with symmetry. *Ergodic Theory and Dynamical Systems*, 15(1):121–147, Feb. 1995.

[37] T. G. Kurtz. Strong approximation theorems for density dependent Markov chains. *Stochastic Processes and their Applications*, 6(3):223–240, Feb. 1978.

[38] R. Kühn. Spectra of sparse random matrices. *Journal of Physics A: Mathematical and Theoretical*, 41(29):295002, June 2008.

[39] D. H. Lee, K. Severin, and M. R. Ghadiri. Autocatalytic networks: the transition from molecular self-replication to molecular ecosystems. *Current Opinion in Chemical Biology*, 1(4):491–496, Dec. 1997.

[40] E. Lieberman, C. Hauert, and M. A. Nowak. Evolutionary dynamics on graphs. *Nature*, 433(7023):312–316, Jan. 2005.

[41] G. J. Lord, C. E. Powell, and T. Shardlow. *An Introduction to Computational Stochastic PDEs*. Cambridge University Press, Aug. 2014. Google-Books-ID: GX_RAwAAQBAJ.

[42] A. J. Lotka. Analytical Note on Certain Rhythmic Relations in Organic Systems. *Proceedings of the National Academy of Sciences of the United States of America*, 6(7):410–415, July 1920.

[43] A. J. Lotka. Elements of physical biology. Feb. 1925.

[44] Y. Martel. *Life of Pi*. Mariner Books, Boston, May 2003.

[45] R. May and W. Leonard. Nonlinear Aspects of Competition Between Three Species. *SIAM Journal on Applied Mathematics*, 29(2):243–253, Sept. 1975.

[46] R. M. May. Will a Large Complex System be Stable? *Nature*, 238(5364):413–414, Aug. 1972.

[47] R. M. May. *Stability and Complexity in Model Ecosystems*. Princeton University Press, Princeton, reprint edition edition, Apr. 2001.

[48] A. J. McKane and T. J. Newman. Predator-prey cycles from resonant amplification of demographic stochasticity. *Physical Review Letters*, 94(21):218102, June 2005. WOS:000229543900050.

[49] M. Mezard, G. Parisi, and M. Virasoro. *Spin Glass Theory and Beyond: An Introduction to the Replica Method and Its Applications*. World Scientific Publishing Company, Nov. 1987. Google-Books-ID: DwY8DQAAQBAJ.

[50] A. D. Mirlin and Y. V. Fyodorov. Universality of level correlation function of sparse random matrices. *Journal of Physics A: Mathematical and General*, 24(10):2273, Jan. 1991.

[51] M. Mobilia. Oscillatory dynamics in rock-paper-scissors games with mutations. *Journal of Theoretical Biology*, 264(1):1–10, May 2010.

[52] D. W. Mock and G. A. Parker. *The Evolution of Sibling Rivalry*. Oxford Series in Ecology and Evolution. Oxford University Press, Oxford, New York, Nov. 1997.

[53] P. A. P. Moran. Random processes in genetics. *Mathematical Proceedings of the Cambridge Philosophical Society*, 54(1):60–71, Jan. 1958.

[54] M. Mézard and G. Parisi. The Cavity Method at Zero Temperature. *Journal of Statistical Physics*, 111(1-2):1–34, Apr. 2003.

[55] M. Mézard, G. Parisi, and M. A. Virasoro. SK Model: The Replica Solution without Replicas. *EPL (Europhysics Letters)*, 1(2):77, Jan. 1986.

[56] M. Mézard, G. Parisi, and R. Zecchina. Analytic and Algorithmic Solution of Random Satisfiability Problems. *Science*, 297(5582):812–815, Aug. 2002.

[57] J. F. Nash. Equilibrium points in n-person games. *Proceedings of the National Academy of Sciences*, 36(1):48–49, Jan. 1950.

[58] J. M. Newby and M. A. Schwemmer. Effects of moderate noise on a limit cycle oscillator: Counter rotation and bistability. *Physical Review Letters*, 112(11), Mar. 2014. arXiv: 1310.2227.

[59] R. M. Nisbet and W. S. C. Gurney. A simple mechanism for population cycles. *Nature*, 263(5575):319–320, Sept. 1976.

[60] J. R. Norris. *Markov Chains*. Cambridge University Press, July 1998.

[61] M. Nowak and R. May. Superinfection and the Evolution of Parasite Virulence. *Proceedings of the Royal Society B-Biological Sciences*, 255(1342):81–89, Jan. 1994. WOS:A1994MT55500012.

[62] M. A. Nowak, K. M. Page, and K. Sigmund. Fairness Versus Reason in the Ultimatum Game. *Science*, 289(5485):1773–1775, Sept. 2000.

[63] M. A. Nowak and K. Sigmund. Evolutionary Dynamics of Biological Games. *Science*, 303(5659):793–799, Feb. 2004.

[64] T. L. Parsons and C. Quince. Fixation in haploid populations exhibiting density dependence II: The quasi-neutral case. *Theoretical Population Biology*, 72(4):468–479, Dec. 2007.

[65] T. L. Parsons and T. Rogers. Dimension reduction for stochastic dynamical systems forced onto a manifold by large drift: a constructive approach with examples from theoretical biology. *arXiv:1510.07031 [math-ph, q-bio]*, Oct. 2015. arXiv: 1510.07031.

[66] M. Perc and A. Szolnoki. Noise-guided evolution within cyclical interactions. *New Journal of Physics*, 9(8):267, Aug. 2007.

[67] T. Pfeiffer, S. Schuster, and S. Bonhoeffer. Cooperation and competition in the evolution of ATP-producing pathways. *Science*, 292(5516):504–507, Apr. 2001. WOS:000168187300047.

[68] M. Rabinovich, A. Volkovskii, P. Lecanda, R. Huerta, H. D. I. Abarbanel, and G. Laurent. Dynamical Encoding by Networks of Competing Neuron Groups: Winnerless Competition. *Physical Review Letters*, 87(6):068102, July 2001.

[69] T. Reichenbach, M. Mobilia, and E. Frey. Coexistence versus extinction in the stochastic cyclic Lotka-Volterra model. *Physical Review E*, 74(5), Nov. 2006.

[70] T. Reichenbach, M. Mobilia, and E. Frey. Mobility promotes and jeopardizes biodiversity in rock – paper – scissors games. *Nature*, 448(7157):1046–1049, Aug. 2007.

[71] G. J. Rodgers and A. J. Bray. Density of states of a sparse random matrix. *Physical Review B*, 37(7):3557–3562, Mar. 1988.

[72] T. Rogers and I. P. Castillo. Cavity approach to the spectral density of non-Hermitian sparse matrices. *Physical Review E*, 79(1):012101, Jan. 2009.

[73] T. Rogers, I. P. Castillo, R. Kühn, and K. Takeda. Cavity approach to the spectral density of sparse symmetric random matrices. *Physical Review E*, 78(3):031116, Sept. 2008.

[74] G. Semerjian and L. F. Cugliandolo. Sparse random matrices: the eigenvalue spectrum revisited. *Journal of Physics A: Mathematical and General*, 35(23):4837, May 2002.

[75] B. Sinervo and C. M. Lively. The rock-paper-scissors game and the evolution of alternative male strategies. *Nature*, 380(6571):240–243, Mar. 1996.

[76] J. M. Smith and G. R. Price. The Logic of Animal Conflict. *Nature*, 246(5427):15–18, Nov. 1973.

[77] G. Szabó and A. Szolnoki. Phase transitions induced by variation of invasion rates in spatial cyclic predator-prey models with four or six species. *Physical Review. E, Statistical, Nonlinear, and Soft Matter Physics*, 77(1 Pt 1):011906, Jan. 2008.

[78] A. Szolnoki, M. Mobilia, L.-L. Jiang, B. Szczesny, A. M. Rucklidge, and M. Perc. Cyclic dominance in evolutionary games: a review. *Journal of The Royal Society Interface*, 11(100):20140735, Nov. 2014.

[79] D. J. Thouless, P. W. Anderson, and R. G. Palmer. Solution of 'Solvable model of a spin glass'. *Philosophical Magazine*, 35(3):593–601, Mar. 1977.

[80] D. F. P. Toupo and S. H. Strogatz. Nonlinear dynamics of the rock-paper-scissors game with mutations. *Physical Review E*, 91(5):052907, May 2015.

[81] R. Trivers. The Evolution of Sex. *The Quarterly Review of Biology*, 58(1):62–67, Mar. 1983.

[82] T.-L. Tsai and J. H. P. Dawes. Dynamics near a periodically-perturbed robust heteroclinic cycle. *Physica D: Nonlinear Phenomena*, 262(Supplement C):14–34, Nov. 2013.

[83] G. J. Velicer and Y. T. N. Yu. Evolution of novel cooperative swarming in the bacterium Myxococcus xanthus. *Nature*, 425(6953):75–78, Sept. 2003. WOS:000185089200040.

[84] V. Volterra. Fluctuations in the Abundance of a Species considered Mathematically. *Nature*, 118(2972):558–560, Oct. 1926.

[85] C. Wedekind and M. Milinski. Cooperation through image scoring in humans. *Science*, 288(5467):850–852, May 2000. WOS:000086869600035.

[86] N. Wiener. Generalized harmonic analysis. *Acta Mathematica*, 55(1):117–258, Dec. 1930.

[87] Q. Yang, T. Rogers, and J. H. P. Dawes. Demographic noise slows down cycles of dominance. *Journal of Theoretical Biology*, 432(Supplement C):157–168, Nov. 2017.

[88] J. S. Yedidia, W. T. Freeman, and Y. Weiss. Exploring Artificial Intelligence in the New Millennium. pages 239–269. Morgan Kaufmann Publishers Inc., San Francisco, CA, USA, Aug. 2002.